ABSTRACT

Title of Dissertation:	ANALYSIS OF RECENT TRENDS IN GLOBAL MEAN SURFACE TEMPERATURE: IMPLICATIONS FOR ACHIEVING THE PARIS AGREEMENT AND QUANTIFICATION OF THE ROLE OF MARITIME EMISSIONS ON GLOBAL WARMING
	Endre Z. Farago, Doctor of Philosophy, 2025
Dissertation directed by:	Professor Ross J. Salawitch, Department of Atmospheric and Oceanic Science, Department of Chemistry and Biochemistry, Earth System Science Interdisciplinary Center

Understanding how human influence affects various components of Earth's climate is a crucial economic and social question of our time. In this dissertation, a set of questions relevant to climate policy and regulations are examined using a reduced complexity climate model, the Empirical Model of Global Climate (EM−GC). First, model simulations are performed to quantify the global mean surface temperature (GMST) in this century, using the projections for the Effective Radiative Forcing (ERF) of greenhouse gases (GHGs) and tropospheric aerosols that were introduced by the AR6 Report of the Intergovernmental Panel on Climate Change (IPCC) in 2021. These updated estimates for ERF are found to result in highly elevated projections of the

GMST, relative to estimates from simulations based on pre-AR6 ERF datasets, for all four Shared Socioeconomic Pathway (SSP) scenarios investigated. The SSP2−4.5 scenario, which is considered to be the most consistent with recent trends in anthropogenic emissions of GHGs, offers only 8% chance of limiting the GMST anomaly to the upper limit of 2.0 ºC prescribed by the Paris Agreement (PA), relative to pre-industrial conditions. Model simulations are presented to quantify the contributing factors to the record high temperature anomalies observed in 2023 and 2024. The temperature anomalies observed in 2023 and 2024 can be reconstructed using existing trends in the rise of GMST, alongside a combination of short-term natural and anthropogenic factors. The reduced emissions of sulfur from maritime traffic, starting in 2020, is found to have contributed at least 0.028 ºC to the GMST, relative to 2019. This estimate was obtained from simulations performed with a new version of the EM−GC model that has been outfitted with an updated ocean module, which is also described in this work. The shift from La Niña to El Niño conditions, combined with a strong Indian Ocean Dipole (IOD) event account for over 50% of the sudden rise in GMST between 2022 and 2023. Short-term variability in the sea surface temperatures (SSTs) of the North Atlantic region were found to have contributed substantially to the GMST anomalies observed in 2023 and 2024, but whether this short-term variability is a direct result of reduced sulfur emissions remains unclear.

ANALYSIS OF RECENT TRENDS IN GLOBAL MEAN SURFACE TEMPERATURE: IMPLICATIONS FOR ACHIEVING THE PARIS AGREEMENT AND QUANTIFICATION OF THE ROLE OF MARITIME EMISSIONS ON GLOBAL WARMING

by

Endre Zoltan Farago

Dissertation submitted to the Faculty of the Graduate School of the
University of Maryland, College Park, in partial fulfillment
of the requirements for the degree of
Doctor of Philosophy
2025

Advisory Committee:
Professor Ross J. Salawitch, Chair
Professor Neil Blough
Associate Professor Timothy P. Canty
Professor Russell R. Dickerson
Professor Sujay Kaushal
Professor Alice Mignerey

© Copyright by
Endre Zoltan Farago
2025

Dedication

To my family and friends, who helped and supported me throughout this journey

Acknowledgements

I would like to thank everyone who supported me during my time at UMD. First, I would like to thank my advisor, Ross, for his patience and understanding, and for the abundance of valuable advice he provided over the years. Second, I would like to thank Laura McBride, who has been an invaluable resource of feedback and advice regarding my research, in particular when it comes to the technical details of the EM−GC model. Third, I would like to thank Austin Hope, Brian Bennett and Tim Canty for their extensive and valuable comments on my paper manuscripts. A special thanks goes to Brian Bennett for his assistance in compiling certain observational datasets, and for his *very* extensive comments on my work. Fourth, I would like to thank Dr. Elizabeth Griffith, with whom I worked alongside as a TA for five semesters. Dr. Griffith's openness to feedback on improving the efficiency of her classes helped extensively in optimizing the amount of time spent on teaching. Fifth, I would like to thank the AOSC MetoGrads for their welcoming and friendly attitude. The MetoGrads treated me as one of their own, even though I was never formally part of the AOSC programme, and for that I will forever be thankful. Finally, I would like to thank all members of the atmospheric chemistry research group, or as we called it, the *chem-group*. The *chem-group* provided me with way more than just research group to be part of; I found a great community and several friends, all of whom helped me greatly in tackling the challenges of graduate school.

Table of Contents

Dedication ii
Acknowledgements iii
Table of Contents iv
List of Tables vi
List of Figures vii
List of Abbreviations viii
Chapter 1: Introduction 1
1.1 Purpose of this Dissertation 2
1.2 Human Influence on Earth's Climate 5
1.2.1 Radiative Forcing 5
1.2.2 Climate Feedback 10
1.3 Modeling of Earth's Climate 12
1.3.1 Coupled Climate Models 13
1.3.2 Reduced Complexity Climate Models 15
1.3.3 Modelling Global Energy Balance 16
1.3.3.1 Climate Sensitivity 17
1.3.3.2 Ocean Heat Export 21
1.4 Policy-relevant Climate Scenarios 24
1.5 Technical updates to the EM−GC modelling framework 26
Chapter 2: AR6 Updates to the RF of GHGs and Aerosols Lowers the probability of Accomplishing the Paris Agreement Compared to AR5 Formulations 28
2.1 Introduction 28
2.2 Data and Methods 30
2.2.1 Shared Socioeconomic Pathway Scenarios 30
2.2.2 Modeling Framework 31
2.2.3 Effective Radiative Forcing 32
2.2.3.1 Effective Radiative Forcing 32
2.2.3.2 Tropospheric Aerosols and Overall Anthropogenic ERF 37
2.2.4 Empirical Model of Global Climate 41
2.2.5 Model Inputs 46
2.2.5.1 Temperature data 46
2.2.5.2 Shared Socioeconomic Pathways 46
2.2.5.3 Baseline Framework 47
2.2.5.4 AR6 Framework 49
2.2.5.5 Natural factors 50
2.2.5.6 Ocean Heat Content 52
2.2.6 Attributable Anthropogenic Warming Rate and Effective Climate Sensitivity 52
2.2.7 Observational Constraining and Ensemble Weighting 54
2.3 Results 55
2.3.1 Ensemble-based Assessment of AAWR and Climate Sensitivity 55
2.3.2 Probabilistic Forecast on Future Warming 64
2.4 Conclusions 73
Appendix A 76

Chapter 3: Implementation of a New Two-layer Energy Balance Module to the EM−GC Model 84
3.1 Introduction 84
3.2 Implementation of EBM−1 in EM−GC 84
3.3 Quantification of the ocean heat transfer parameter γ 88
3.4 Calibration of heat capacities 90
Appendix B 93
Chapter 4: Quantification of the Natural and Anthropogenic Contributors to the GMST Anomalies in 2023 and 2024 96
4.1 Introduction 96
4.2 Data and Methods 98
4.2.1 Empirical Model of Global Climate 98
4.2.1.1 Two−layer Energy Balance Model 101
4.2.1.2 Ensemble Method and Probabilistic Forecasts 101
4.2.2 Data and Model Input 103
4.2.2.1 Temperature Records 103
4.2.2.2 Effective Radiative Forcing 103
4.2.2.3 El-Niño Southern Oscillation, Indian Ocean Dipole and Pacific Decadal Oscillation 104
4.2.2.4 Total Solar Irradiance and Volcanic Activity 106
4.2.2.5 Atlantic Multidecadal Variability 107
4.2.2.6 Ocean Heat Content 108
4.3 Results 109
4.3.1 Long-term warming trends 109
4.3.2 Natural and anthropogenic contributions to temperature anomalies in 2023 and 2024 111
4.3.3 North Atlantic warming 116
4.4 Conclusions 120
Appendix C 122
Chapter 5: Conclusions and Future Opportunities 125
5.1 Summary and Conclusions 125
5.2 Future Directions 128
Bibliography 134

List of Tables

Table 2.1 – ΔT_{2100} for the Four SSP Scenarios Studied..... 66
Table 2.2 – Years of Crossing the 1.5 ºC and 2.0 ºC GMST Anomaly Thresholds 69
Table 2.3 – Probability of Achieving the Paris Agreement Target and Upper Limit..... 72
Table 2.A1 – Formulations of SARF and ERF..... 79
Table 2.A1 – Coefficients and pre-industrial Concentrations 80
Table 2.A3 – Parameters of Gaussians used for Weighting the EM−GC Ensemble..... 81
Table 4.1 – Estimates of ΔERF_{IMO} and ΔT_{IMO} 114

List of Figures

Figure 1.1 – Schematic Representation of the Global Energy Budget 6
Figure 1.2 – Radiative Forcing of the Climate 8
Figure 1.3 – Combined Assessment for the Strength of Climate Feedbacks..... 11
Figure 1.4 – Effective and Equilibrium Climate Sensitivity..... 18
Figure 1.5 – Surface Temperature under abrupt4xCO_2 Conditions..... 22
Figure 1.6 – Process of Climate Scenario Development 24
Figure 2.1 – Concentrations of GHGs and ERF due to GHGs and Aerosols 35
Figure 2.2 – Contributions of Natural and Anthropogenic Factors to GMST 44
Figure 2.3 – Aerosol Weighting Method, AAWR and EffCS 56
Figure 2.4 – Probability Distribution Functions (PDFs) for AAWR and EffCS 58
Figure 2.5 – Equilibrium Climate Sensitivity 62
Figure 2.6 – GMST Anomaly at the end of the Century 65
Figure 2.7 – Probabilistic Forecasts of the GMST Anomaly..... 67
Figure 2.8 – Probability Distribution Functions (PDFs) of ΔT_{2100} 70
Figure 2A.1 – ERF_{AER} Ensemble..... 82
Figure 2A.2 – GMST Anomaly at the end of the Century for the Baseline Framework..... 82
Figure 2A.3 – Probabilistic Forecasts of the GMST for the Baseline Framework..... 83
Figure 3.1 – Values of AAWR for Combinations of C_u and C_d 92
Figure 3.2 – Comparison of EM−GC to CMIP6 Models Under abrupt4xCO_2 Conditions .. 92
Figure 3.B.1 – Values of EffCS for Combinations of C_u and C_d..... 94
Figure 3.B.2 – Values of γ for Combinations of C_u and C_d 95
Figure 4.1 – Contributions of Natural and Anthropogenic Factors to GMST 99
Figure 4.2 – Aerosol Weighting Method and AAWR 110
Figure 4.3 – Contributing Factors to GMST Between 2019 and 2024 112
Figure 4.4 – Contributing Factors to GMST Between 2019 and 2024, AMV Filtered 119
Figure 4C.1 – Ocean Heat Content Time Series..... 123
Figure 4C.2 − Aerosol Weighting Method and EffCS 124
Figure 5.1 – Effective Radiative Forcing due to Black Carbon..... 131

List of Abbreviations

AAWR:	Attributable Anthropogenic Warming Rate
AMO:	Atlantic Multidecadal Oscillation
AMOC:	Atlantic Meridional Overturning Circulation
AMV:	Atlantic Multidecadal Variability
CCN:	Cloud Condensation Nuclei
CMIP:	Coupled Model Intercomparison Project
DMI:	Dipole Mode Index
EBM:	Energy Balance Model
EEI:	Earth's Energy Imbalance
EffCS:	Effective Climate Sensitivity
EM−GC:	Empirical Model of Global Climate
ENSO:	El Niño Southern Oscillation
ERF:	Effective Radiative Forcing
ESM:	Earth System Model
GCM:	General Circulation Model or Global Climate Model
GHG:	Greenhouse Gas
GloSSAC:	Global Space-based Stratospheric Aerosol Climatology
GMST:	Global Mean Surface Temperature
GSAT:	Global Surface Air Temperature
IAM:	Integrated Assessment Model
IMO:	International Maritime Organization
IPCC:	Intergovernmental Panel on Climate Change

IRF:	Instantaneous Radiative Forcing
IOD:	Indian Ocean Dipole
LUC:	Land-use Change
MAGICC:	Model for the Assessment of Greenhouse Gas Induced Climate Change
MLO:	Mauna Loa Observatory
MLR:	Multiple Linear Regression
ODS:	Ozone Depleting Substance
OHE:	Ocean Heat Export
OHC:	Ocean Heat Content
PA:	Paris Agreement
PDO:	Pacific Decadal Oscillation
RCM:	Reduced Complexity Climate Model
RCP:	Representative Concentration Pathway
RF:	Radiative Forcing
SAOD:	Stratospheric Aerosol Optical Depth
SARF:	Stratospheric Adjusted Radiative Forcing
SCM:	Simplified Climate Model
SSP:	Shared Socioeconomic Pathway
SST:	Sea Surface Temperature
TOA:	Top of the atmosphere
TSI:	Total Solar Irradiance
WMO:	World Meteorological Organization

Chapter 1: Introduction

Understanding Earth's climate, and the various processes that drive it, is a critical social, political and economic issue of our era. The Industrial Revolution of the 18th century kickstarted a period of almost three centuries, during which the benefits of fossil fuels were harnessed to improve industrial output and the economy across the world. However, these benefits have come at a cost: in this period known as the Anthropocene, several components of the climate system were altered by human activity. Emissions of greenhouse gases (GHGs) have resulted in increased surface temperatures, while tropospheric aerosols of anthropogenic origin have adversely affected the air quality in several parts of the world. A vast amount of research is focused on studying the impacts of anthropogenic activity on various parts of the climate system. Due to the complexity of the underlying processes however, several components of Earth's climate, and the influence of anthropogenic activity on them, are not yet fully understood. Changes to Earth's climate system carry with them the danger of negatively affecting economies and human welfare across the world, such as by increasing the frequency and risk of extreme weather events or by affecting crop yields and the food supply chain. Consequently, climate model simulations are key tools for informing policymakers about potential changes in Earth's climate system in response to anthropogenic activity. This dissertation aims to contribute to this field by analyzing several policy-relevant problems, including the long-term influence of anthropogenic activity on global climate in the coming decades, as well as the short-term impacts of recently introduced climate policies.

1.1 Purpose of this Dissertation

The warming of Earth's climate is strongly correlated with the anthropogenic emissions of GHGs. GHGs alter the energy balance of the planet by trapping outgoing radiation, which is referred to as the greenhouse effect. Conversely, tropospheric aerosols scatter incoming solar radiation, and alter several properties of clouds, thereby cooling the planet and offsetting a portion of GHG-induced warming. The influence of GHGs and tropospheric aerosols on Earth's radiative balance is quantified by their radiative forcing (RF). However, the connection between the emissions of GHGs and aerosols, and the corresponding RF is not yet fully understood. Here, a few key uncertainties relevant to this dissertation are listed, though this list is by no means exhaustive. The RF of GHGs depend on their atmospheric concentration; how the atmospheric concentrations of GHGs evolve in response to anthropogenic emissions, surface temperature, and the effectiveness of chemical and biological sinks remains uncertain. Similarly, the influence of tropospheric aerosols on radiative balance, in particular, through their interactions with clouds, is not well quantified. Consequently, climate model simulations that are used to inform policymakers about the climate outcomes of various emissions policies must account for the uncertainties associated with the connection between the emissions of various GHGs and aerosols, and their influence on Earth's radiative balance.

Chapter 1 of this dissertation provides a brief overview of the key considerations when modeling the influence of GHGs and tropospheric aerosols on Earth's radiative balance and, consequently, surface temperatures. In Chapters 2−4, a reduced complexity climate model, the Empirical Model of Global Climate (EM−GC), developed and maintained at the University of Maryland is used to provide short and long-term forecasts of global mean surface temperatures (GMST).

Chapter 2 of this dissertation focuses on the updates to the formulations of RF of GHGs and tropospheric aerosols introduced by the Sixth Assessment Report (AR6) of the Intergovernmental Panel on Climate Change (IPCC). Since the rise in GMST is proportional to the magnitude of RF, updated projections of RF affect the forecasted GMST. Therefore, the primary research question of Chapter 2 is how the updates to the formulations of RF introduced by AR6 influence the projected GMST by the end of the century. Chapter 2 also provides updated quantifications on the likelihood of accomplishing the goals of the Paris Agreement (PA), which aims to limit the rise in GMST to 1.5 ºC (PA Target) or 2.0 ºC (PA Upper Limit) by the end of the century, relative to pre-industrial conditions. Chapter 2 therefore serves as an extension of McBride et al., (2021), who provided forecasts of the GMST with the EM−GC model using datasets that predated the AR6 report.

While Chapter 2 focuses on the long-term impact of anthropogenic activity on GMST, Chapter 4 examines the short-term consequences of anthropogenic activity. Specifically, the GMST anomalies observed in the years 2023 and 2024 were much higher than the years directly prior, as well as the values projected by climate models for these two years (Schmidt, 2024). The unexpectedly high GMSTs observed in 2023 and 2024 therefore raised questions about whether the sudden rise in the GMST is driven by natural variability, a short-term anthropogenic influence, or some combination of these factors. One key research question is how the regulations on the sulfur content of fuels used in international shipping, introduced by the International Maritime Organization (IMO) starting in January 2020, affected the GMST anomalies. As sulfate aerosols cool the surface, it is a critical question whether the unexpectedly high GMST anomalies observed in 2023 and 2024 can be attributed to the reduced emissions of sulfur from international shipping. Chapter 4 thus focuses on a highly policy-relevant question, which has seen an extensive level of

interest from the climate modelling community recently (Gettelman et al., 2024; Jordan and Henry, 2024; Quaglia and Visioni, 2024; Watson-Parris et al., 2024; Yoshioka et al., 2024; Yuan et al., 2024). As efforts to improve air quality by reducing aerosol loading continue, the conclusions of this chapter contribute to the understanding of the short-term impacts of such efforts on the global climate.

The version of the EM−GC model that is used in Chapter 2 includes an ocean module that was originally developed and described in Hope et al., (2020) and later used in McBride et al., (2021) as well. This module, however, uses a simplified two-layer energy balance component, which overestimates the short-term change in GMST in response to sudden changes in RF. This problem is negligible when performing simulations on multi-decadal timescales as done in Chapter 2, but becomes significant when modelling the short-term impacts of changes in RF on the GMST in Chapter 4. Consequently, to accurately quantify the influence of the IMO regulations on the GMST, the model needed to be updated with an energy balance component that provides a more accurate short-term temperature response to sudden changes in RF. In Chapter 3, a new ocean module to the EM−GC is presented, which is based on the two-layer energy balance model (EBM) proposed in Held et al., (2010). Chapter 3 also presents the observation-driven calibration of the two-layer EBM, as well as the results of a series of benchmark simulations. The observation-driven calibration of the two-layer EBM component of EM−GC described in Chapter 3 is a new and novel method for calibrating the two-layer EBM, and is distinctly unique from the calibration methods of other climate models that use a similar two-layer EBM approximation. The two-layer EBM component presented in Chapter 3 therefore provides a substantial improvement in the short-term temperature response of the model, while retaining the observation-driven nature of the EM−GC.

The updated version of the EM−GC model presented in Chapter 3 is then used in Chapter 4 to quantify the contributing factors to the observed GMST anomalies in 2023 and 2024. Finally, Chapter 5 provides concluding remarks, as well as a series of additional recommendations for future model updates and policy-relevant questions for further study.

1.2 Human Influence on Earth's Climate

1.2.1 Radiative Forcing

Several factors influence the amount of solar radiation that reaches Earth's surface, and the amount of energy radiated back to space. Figure 1.1 provides a schematic representation of Earth's energy budget. Incoming shortwave radiation (340 W m^{-2} in Fig. 1.1) from the sun is partially reflected by the atmosphere. The majority of the incoming radiation that reaches the surface (185 W m^{-2}) is absorbed by the surface (161 W m^{-2}), with a small portion being reflected (24 W m^{-2}). The energy absorbed by the surface is reemitted in the form of longwave (infrared) radiation (398 W m^{-2}). A small portion of this longwave radiation escapes directly to space through the so-called atmospheric windows, while the majority of this radiation is absorbed by the atmosphere, and then re-emitted in all directions. The longwave radiation emitted by the atmosphere towards the surface (342 W m^{-2}) is known as back-radiation. The ability of atmospheric constituents to absorb incoming longwave radiation and re-emit this radiation towards the surface is referred to as the greenhouse effect.

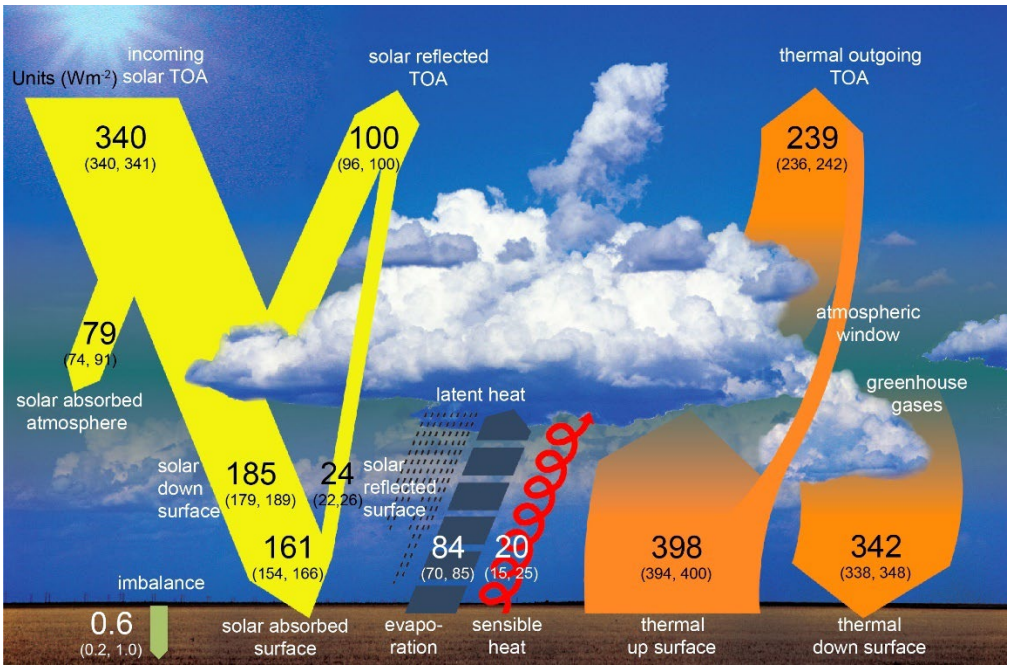

Figure 1.1 Schematic representation of the global energy budget. Yellow and orange arrows correspond to fluxes of shortwave and longwave radiation, respectively. All values are in W m^{-2}. Reproduction of Fig. 2.11 of Hartmann et al., (2013)

GHGs, such as carbon dioxide (CO_2), methane (CH_4), nitrous oxide (N_2O), water vapor (H_2O) and tropospheric ozone (O_3), absorb certain wavelengths of infrared radiation, governed by their respective infrared absorption spectra. Radiation with wavelengths corresponding to low atmospheric absorption, such as 10−12 μm, is allowed to escape to space without being absorbed by the atmosphere; such ranges of wavelengths are commonly referred to as atmospheric windows. Increasing concentrations of GHGs result in a greater absorption of longwave radiation and subsequent back-radiation, thereby leading to a larger amount of energy retained by the planet. The influence of GHGs on the atmospheric radiative transfer is quantified by the RF associated with each GHG. The unique absorption spectrum of each GHG, along with the overlaps between the absorption spectra of different GHGs, means that the mathematical relationship between the atmospheric abundance and the RF due to GHGs is different for each gas.

Small particulate matter suspended in air in the lower atmosphere is commonly referred to as tropospheric aerosols. Tropospheric aerosols are either emitted directly into the atmosphere, or form from precursor gases in the atmosphere. These two categories are commonly referred to as primary and secondary aerosols. Most of the anthropogenic emissions of tropospheric aerosols and their precursors are related to the combustion of fossil fuels. The influence of tropospheric aerosols on atmospheric radiative transfer depends heavily on their type. For example, black carbon aerosols, which originate from incomplete combustion of fossil fuels, absorb solar radiation and contribute to the warming of the climate (Bond et al., 2013; Forster et al., 2021a). Meanwhile, emissions of SO_2 from the combustion of sulfur-containing fossil fuels, such as coal, lead to the formation of sulfate aerosols that exert a cooling effect, as described below (Bellouin et al., 2020).

While GHGs increase Earth's energy imbalance by trapping a portion of the outgoing longwave radiation, tropospheric aerosols of anthropogenic origin exert a net cooling effect through processes categorized as direct and indirect effects. Aerosol direct effects are related to the scattering and absorption of a portion of the incoming shortwave radiation, as well as the trapping of longwave radiation. The combination of these processes yields an overall cooling effect (Forster et al., 2021a), primarily due to the scattering of incoming shortwave radiation by sulfate aerosols (Szopa et al., 2021), which reduces the amount of energy reaching Earth's surface. Meanwhile, tropospheric aerosols also increase the number of cloud condensation nuclei (CCN), thereby increasing the reflectivity (albedo) and extending the lifetime of clouds (Twomey, 1974; Albrecht, 1989). Aerosol-cloud interactions contribute strongly to the overall cooling effect of tropospheric aerosols (Forster et al., 2021a). Tropospheric aerosols, particularly those with diameters smaller than 2.5 μm, commonly referred to as PM2.5, have several adverse health effects (Cissé et al., 2022). Consequently, efforts to improve air quality have led to policies which aim to

reduce the anthropogenic emissions of aerosols and aerosol precursors. As tropospheric aerosols help offset a portion of the GHG-induced warming, reduced aerosol loading due to air-quality considerations leads to an increase in surface temperatures.

Figure 1.2 shows the RF due to various GHGs and tropospheric aerosols in the year 2011, relative to pre-industrial conditions. As shown in Fig. 1.2, the largest contributor to the total RF due to GHGs is CO_2. However, several other GHGs, most notably CH_4, N_2O, tropospheric O_3, and a combination of halogenated species, such as halocarbons, SF_6 and NF_3 contribute to the RF of the climate. Several halogenated species also contribute to the destruction of the stratospheric ozone layer; these species are collectively termed ozone depleting substances (ODSs). Critically, as shown in Fig. 1.2, there is significant uncertainty in the magnitude of the RF due to both the aerosol direct and indirect effects, which is the primary cause of the large uncertainty in total anthropogenic RF. Therefore, climate model simulations must account for this uncertainty in the RF of tropospheric aerosols.

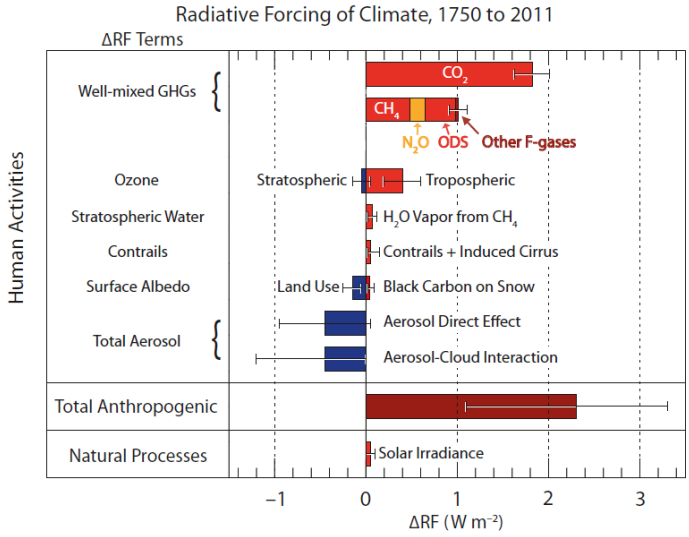

Fig. 1.2: Radiative forcing of the climate in 2011 relative to pre-industrial conditions. Error bars correspond to 5−95% uncertainty ranges. The categories "ODS" and "Other F−gases" correspond to a combination of various halogenated species as described in Salawitch et al., (2017). Reproduction of Figure 1.4 of Salawitch et al., (2017).

So far, the collective term "RF" has been used to provide a qualitative description of how GHGs and aerosols affect atmospheric radiative transfer. There are, however, three different definitions of radiative forcing, termed instantaneous RF (IRF), stratospheric adjusted RF (SARF) and effective RF (ERF) (Forster et al., 2021a). The IRF is defined as the change in the net top-of-atmosphere (TOA) radiative flux without any additional adjustments following a perturbation, such as an increase in GHG or aerosol abundances. SARF represents the change in net TOA radiative flux in response to a perturbation, after the temperature of the stratosphere was allowed to adjust to this perturbation. Finally, ERF corresponds to the change in the net TOA flux in response to a perturbation after allowing for the adjustment of both the stratospheric and tropospheric temperatures, as well as certain surface properties that are uncoupled to the change in Global Surface Air Temperature (GSAT) (Forster et al., 2021a). The adjustments to RF described above are commonly referred to as *rapid adjustments* (Smith et al., 2018b). Rapid adjustments are considered to be a part of the RF, and are defined such that they are independent of the surface temperature change (Smith et al., 2018b; Forster et al., 2021a).

The Fifth Assessment Report of IPCC (AR5) (Boucher and Randall, 2013), "recommended ERF as a more useful measure of the climate effects of a physical driver than [SARF]" (Forster et al., 2021a). However, AR5 considered SARF to be equal to ERF for many GHGs. The AR6 report introduced updated assessments on rapid adjustments (Fig. 7.4 of Forster et al., (2021a)), and within AR6, ERF is no longer considered equal to SARF. Further, new mathematical formulas used to convert the atmospheric concentration of GHGs to radiative forcing were also introduced by the AR6 report (Smith et al., 2021a), relative to the formulations of Myhre et al., (1998), which were adapted by previous IPCC Assessment Reports (IPCC, 2001, 2007, 2013b). These changes raised the question of how the projections of future warming are affected by the updates to the

calculation of ERF introduced by the AR6 report. The EM−GC simulations presented in Chapter 2 examine this problem by contrasting the future warming projected using the AR6 ERF datasets as model inputs, with simulations that are based on ERF data that predate the AR6 report.

1.2.2 Climate Feedback

As shown in Fig. 1.1, a portion of the incoming shortwave radiation is reflected by the surface. The warming of the atmosphere due to anthropogenic activity leads to reduced snow and ice cover, lowering the reflectivity of the surface. This phenomenon, known as the albedo feedback, is one of many climate feedbacks influencing Earth's climate. Climate feedbacks are processes that either amplify (positive feedbacks) or dampen (negative feedbacks) the magnitude of warming in response to increasing RF. Albedo feedback is a positive feedback, as the increase in surface temperatures due to anthropogenic activity is amplified by the reduced reflection of incoming shortwave radiation.

Climate feedbacks vary greatly in their magnitude and the timescale of their response. Climate feedbacks that exert their influence on timescales of years or faster are often termed *fast feedbacks* (Charney et al., 1979). Meanwhile, climate feedbacks that are relevant only over multi-century or multi-millennial timescales are referred to as *slow feedbacks* (Forster et al., 2021a). The IPCC AR6 report provided an assessment of the magnitude of climate feedback for several fast feedback processes, which are shown in Fig. 1.3. This figure also shows the multi-model mean and range of climate feedback that were estimated from the simulations performed with the coupled climate models of Phase 5 and Phase 6 of the Coupled Model Intercomparison Project (CMIP5 and CMIP6, respectively). The use of coupled climate models, and the CMIP protocol is described in greater detail in Sect. 1.3.1.

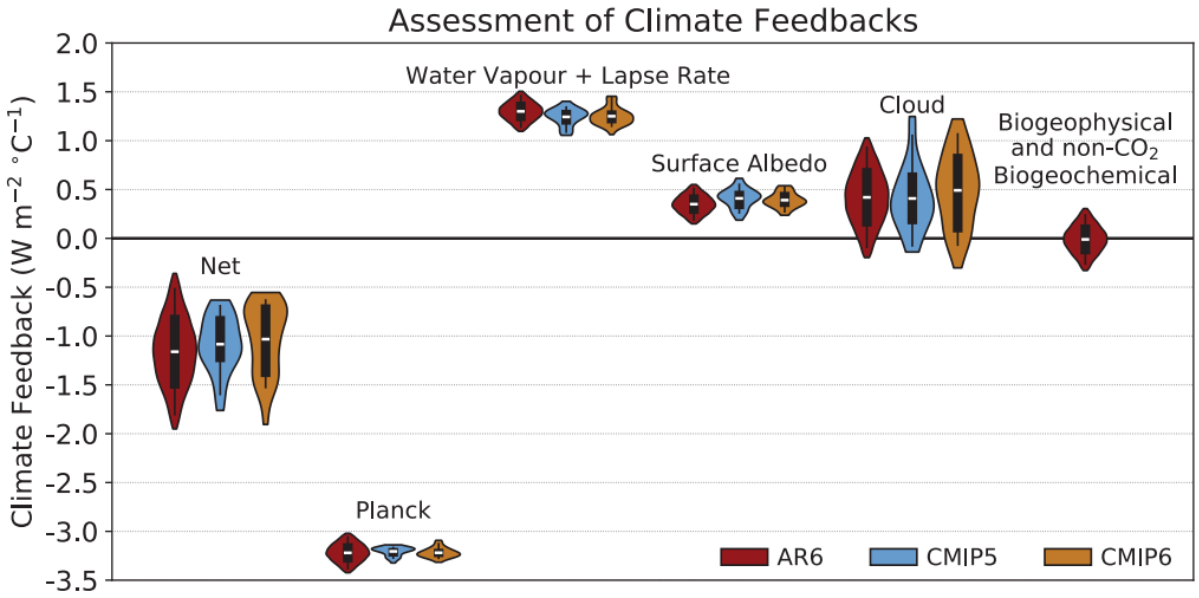

Fig. 1.3: Combined assessment and model-based estimates for the strength of various feedback processes. The white line, black box and black vertical line correspond to the mean, 66% and 90% uncertainty ranges, respectively. The colored shading corresponds to the probability distribution for the estimates from the CMIP5 and CMIP6 ensembles (blue and orange, respectively) and represents the 95% confidence range for the AR6 combined assessment (red). Reproduction of Figure 7.10 of IPCC AR6 (Forster et al., 2021a).

The warming of the atmosphere leads to increased evaporation of water, thereby increasing the water vapor content of the atmosphere. Water vapor is a highly potent GHG, and therefore, increasing surface temperatures are amplified by the rising atmospheric water vapor content. This positive feedback is referred to as water vapor feedback (Forster et al., 2021a). Lapse-rate feedback is related to the nonuniform change in the vertical temperature profile of the tropopause. Over the tropics, the upper troposphere warms more than the lower troposphere does, leading to an increased emission of longwave radiation at the TOA. Consequently, over the tropics, lapse-rate feedback acts as a negative feedback. In the extratropics, however, the lower troposphere warms quicker than the upper troposphere, leading to a positive lapse-rate feedback. On a global level, the effects of the tropics dominate, and the net global lapse-rate feedback is negative (Forster et al., 2021a). The term "cloud feedbacks" corresponds to a wide array of physical processes through

which surface warming affects cloud microphysics (Sect. 7.4.2.4 of Forster et al., (2021a)). The overall cloud feedback is believed to be positive with less than 10% of a probability that cloud feedbacks are negative. There is a considerable level of uncertainty in the magnitude of cloud feedbacks, however, which is the primary driver of the large uncertainty in net climate feedback. Consequently, climate model simulations must also consider the uncertainty in the magnitude of the net climate feedback, alongside the uncertainty in anthropogenic RF. The Planck feedback, which relates to the fact that a warmer planet emits more longwave radiation thereby cooling the planet, is considered with a negative sign in Fig. 1.3. As described in Sect. 1.3.3, there is no universally accepted notation or sign for the net climate feedback, and climate models may differ in the exact mathematical implementation of the various climate feedback terms.

Finally, the magnitude of climate feedbacks is believed to be both time- and temperature-dependent (Forster et al., 2021a), which is addressed further in Sect. 1.3.3.1. However, many simplified climate models use the approximation that, over the timeframe of their simulations, the value of the net climate feedback can be treated as constant. This assumption was found to be a good approximation within the EM−GC model by McBride et al., (2021). Further, the two-layer energy balance representation, upon which the updates to the EM−GC ocean module presented in Chapter 3 are based, also uses the assumption that climate feedback is constant. This representation was found to provide a temperature response highly similar to those of more complex climate models for simulations shorter than about three centuries (Geoffroy et al., 2013a).

1.3 Modeling of Earth's Climate

To provide forecasts of the changes in the climate system, a wide variety of computer models were developed in the recent decades. These models vary in complexity from comprehensive coupled models (Sect. 1.3.1) to reduced complexity climate models (RCMs, Sect.

1.3.2), which simplify certain components of the climate system to reduce the computational cost of simulations. The key considerations for the reduced complexity modelling of global energy balance are described in Sect. 1.3.3, which also provides the basis for the updates to the EBM module of EM−GC that are described in Chapter 3. Finally, climate model simulations are generally performed for a set of standardized climate scenarios that each correspond to various projections for the emissions of GHGs and aerosols, which are briefly reviewed in Sect. 1.4.

1.3.1 Coupled Climate Models

Climate models of various complexities are instrumental for studying the effects of anthropogenic activity on Earth's climate. General Circulation Models (GCMs), which are sometimes referred to as Global Climate Models, and Earth System Models (ESMs) are the most comprehensive tools currently available for such purposes. GCMs solve sets of equations that represent the physical processes of the components of the climate system, such as the atmosphere, oceans, and the land surface, and the interactions between them. GCMs and ESMs divide Earth into a three-dimensional grid, where two dimensions represent the surface of the planet, with the third (vertical) dimension corresponding to altitude in the atmosphere and depth in oceans. The more refined the grid is, the higher the computational demand of the model. Since Earth's climate is a complex system with numerous components that all interact with each other, GCM and ESM simulations require substantial computational resources.

Early GCMs were only able to provide simplified simulations of the physics of the atmosphere, land surface, and the oceans. As the computational power of supercomputers improved, newer GCMs became able to provide more detailed simulations of these components, while incorporating additional elements of the climate system and simulating the interactions

between them. GCMs and ESMs are commonly referred to as coupled climate models, due to their ability to simulate the interactions between the various components of the climate system.

ESMs are among the most advanced coupled climate models currently available and differ from GCMs in that ESMs can also simulate the chemical and biological processes on Earth, such as the carbon cycle or the nitrogen cycle. Importantly, since ESMs possess the ability to simulate chemical and biological processes involved in the loss of GHGs, ESMs are able to compute the concentrations of GHGs from emissions (Meinshausen et al., 2020). This ability has not yet been leveraged to a large extent due to the high computational demand of such simulations. Consequently, ESM simulations are often conducted in a so-called concentration-driven mode, where pre-calculated concentrations of GHGs are used as inputs, rather than emissions.

The projected surface temperatures in response to rising GHG concentrations differ substantially between individual coupled climate models, due to differences in parametrizations and the levels of detail at which the components of Earth's climate are simulated. Intercomparison projects, such as the Coupled Model Intercomparison Project (CMIP) initiative, are collaborations aimed at comparing the output of different climate models under a set of standardized climate scenarios (Taylor et al., 2012; Eyring et al., 2016). The IPCC assessment reports rely heavily on the output of CMIP model simulations, with the IPCC AR5 and AR6 reports having been based on the output of model runs from the fifth and sixth phase of the CMIP exercise, termed CMIP5 and CMIP6, respectively.

While CMIP6 ensemble members are among the most comprehensive coupled models available, questions regarding the magnitude of warming projected by certain CMIP6 models arose in recent years. Several studies indicated that certain CMIP6 models overestimate the magnitude of future warming in response to increasing RF (Tokarska et al., 2020b; McBride et al., 2021;

Hausfather et al., 2022; Voosen, 2022; Rugenstein et al., 2023). This phenomenon has recently been termed the "hot-model problem" (Hausfather et al., 2022). The hot-model problem, along with the high computational demand of GCMs, increases the significance of the development and use of alternative modelling tools, such as reduced complexity climate models.

1.3.2 Reduced Complexity Climate Models

While coupled climate models provide the most comprehensive simulations of Earth's climate, reduced complexity climate models (RCMs), which are sometimes referred to as Simplified Climate Models (SCMs), offer lower computational costs, thereby allowing for a larger number of climate scenarios to be studied in a given amount of time than what is feasible with coupled models. RCMs vary greatly in design, as individual models differ in the specific simplifications of the climate system used during simulations. Most RCMs possess a much smaller spatial resolution, if any, than coupled climate models (see Table 1 of Nicholls et al., (2020)). Instead, RCMs typically provide their output as global means, with the primary output being the GMST in the future under a variety of emissions scenarios. Most RCMs simulate the GMST based on the conservation of energy on a global scale. The key considerations when modelling this global energy balance are reviewed in Sect. 1.3.3.

The EM−GC model, which is used to perform the simulations presented in Chapters 2−4, also uses this global energy balance approach to simulate the rise in GMST in response to anthropogenic activity (ΔT_{ANTH}). In addition to the energy balance component, EM−GC also employs a multiple linear regression (MLR) component to quantify the contribution of internal variability, that is, processes independent of anthropogenic activity, to the GMST. The EM−GC considers the uncertainty in the magnitude of climate feedback and anthropogenic ERF using an ensemble method (Hope et al., 2020; McBride et al., 2021). The model is observationally

constrained, which means that ensemble members where the simulated GMST or Ocean Heat Content (OHC) is inconsistent with observations over the so-called training period are eliminated. The training period used in this dissertation spans between 1850 and 2019. The projections of future GMST within EM−GC in response to rising ERF are therefore informed by the observationally constrained analysis of the evolution of the GMST in response to anthropogenic activity in the historical past.

1.3.3 Modelling Global Energy Balance

While Earth's radiative balance is influenced by several factors (Fig. 1.1), the overall energy balance of our planet can be simplified into the general expression shown in Eq. (1.1) (Gregory et al., 2004).

$$N = F - \alpha T \tag{1.1}$$

In Eq. (1.1), N represents the time-dependent change in the TOA net energy flux (in units of W m^{-2}). This quantity is also referred to as Earth's energy imbalance (EEI). The quantities F and T correspond to the time-dependent change in radiative forcing (in units of W m^{-2}) and global-mean surface temperature (in units of K), respectively. N, F and T are generally treated as anomalies relative to a pre-industrial climate, where the values of N, F and T are defined to be equal to 0. α represents the magnitude of total climate feedback, and is referred to as the climate feedback parameter (in units of W m^{-2} K^{-1}).

There exists a large level of inconsistency between the notations used for climate feedback, with no uniformly accepted convention (Forster et al., 2021a). Many studies denote climate feedback with λ instead, and the sign of the feedback parameter, and hence the sign of the "αT" term in Eq. (1.1), also differs between studies. Consequently, care must be taken when using the above formulation to avoid confusion between the different notations for climate feedback. In this

dissertation, the following conventions are adopted: first, the numerical value of α is defined to be greater than zero (Gregory et al., 2015). Second, within EM−GC, the Planck feedback is mathematically separated from the sum of all other feedbacks; these two quantities correspond to the parameters λ_p and λ_Σ, respectively. These notations have been retained in this dissertation to maintain consistency with earlier versions of EM−GC. The value of α relates to these two quantities such that $\alpha = \lambda_p - \lambda_\Sigma$ (Hope et al., 2020).

The expression shown in Eq. (1.1) provides a connection between the radiative forcing and the surface temperature anomaly, and serves as the basis for the simulation of surface temperature in several RCMs. Importantly however, this equation only offers a general framework for climate models, and the modelled change in global surface temperatures in response to changes in RF depends heavily on the mathematical implementation of the EEI and climate feedback terms. These differences are best illustrated by performing a set of benchmark simulations, which are described below.

1.3.3.1 Climate Sensitivity

To test the temperature response of coupled models and RCMs to various idealized changes in RF, a set of benchmark scenarios was developed. This section focuses on the *abrupt2xCO₂* simulation, in which the atmospheric concentration of CO_2 is instantaneously doubled relative to the pre-industrial levels at the beginning of the simulation and then held constant for the remainder of the simulation. Consequently, *abrupt2xCO₂* simulations represent how a climate model responds to sudden changes in RF.

The primary output of *abrupt2xCO₂* simulations is the Equilibrium Climate Sensitivity (ECS), which is defined as the GMST after Earth's climate has fully equilibrated following an abrupt doubling of CO_2 concentrations. Such an equilibrium, however, takes multiple millennia to

reach, and running coupled climate models to cover such long time periods has not been feasible until very recently. Consequently, several methods have been developed to approximate the value of ECS, and conflicting definitions of ECS exist between different phases of model development.

Figure 1.4 shows the schematic illustration of the TOA net flux (N) plotted against the global mean surface temperature (T) in response to an abrupt doubling of CO_2 concentrations. The grey circles represent annual GMST for the first 150 years of the simulation, while crosses correspond to decadal means after the first 150 years. The trendlines correspond to various linear approximations of the N−T relationship following Eq. (1.1) as described below. Over the first approximately 150 years of the simulation, the N−T relationship is near linear, and therefore the feedback parameter α in Eq. (1.1) can be treated as constant (Gregory et al., 2004). However, this linearity does not hold true over the millennial timescales required for full equilibration.

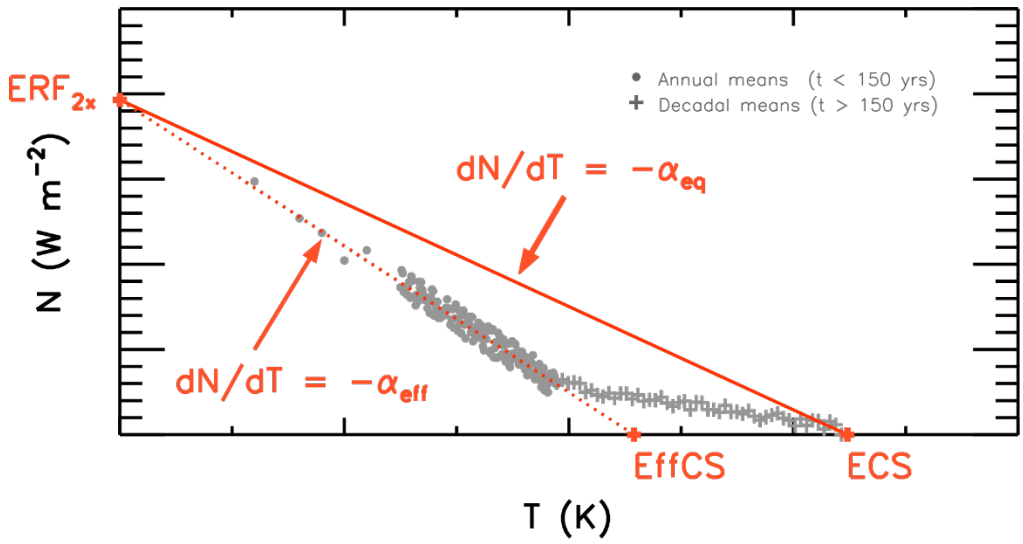

Fig. 1.4: Schematic illustration of the relationship between the TOA net radiative flux (N) and global mean surface temperature (T) during an abrupt2xCO_2 simulation. Circles represent annual means for the first 150 years of the simulation, while crosses correspond to decadal means thereafter. ERF_{2x} corresponds to the ERF due to the abrupt doubling of CO_2 concentrations.

The most common method to quantify the climate sensitivity of a climate model without running the model to full equilibration uses a linear fit to the N−T relationship over the first 150

years of an *abrupt2xCO₂* simulation (dotted line in Fig. 1.4). In equilibrium, N = 0 W m^{-2}, and therefore, this linear fit is extrapolated to find the x-intercept, which is used as an estimate for climate sensitivity (Gregory et al., 2004). This method, generally referred to as the Gregory-regression, has been used extensively to quantify the climate sensitivity of CMIP models, and the climate sensitivity obtained with this method is often termed ECS. Recently, simulations with a small set of CMIP models were performed over multi-millennial timescales under the aegis of the LongRunMIP protocol (Rugenstein et al., 2019). By equilibrating CMIP models, ECS was found to be, on average, 17% higher than the values inferred using the Gregory-regression (Rugenstein et al., 2020).

The difference between the values of ECS obtained from fully equilibrated climate models, and those quantified using the Gregory-regression has led to the proposal of a revised nomenclature for climate sensitivity, which is also adopted for this dissertation. In this convention, ECS is defined as the surface temperature in equilibrium, whereas the climate sensitivity inferred from a regression to a finite, non-equilibrium period is referred to as Effective Climate Sensitivity (EffCS). Consequently, the climate sensitivity estimated using the Gregory-method is better referred to as EffCS. This convention, however, has not yet been uniformly adopted.

Finally, EffCS is often quantified using *abrupt4xCO₂* model runs instead of *abrupt2xCO₂*, with the x-intercept from the Gregory-regression divided by a factor of two (e.g. Eyring et al., (2016), Zelinka et al., (2020), Tokarska et al., (2020b), McBride et al., (2021)). This approximation, however, tends to yield higher estimates of climate sensitivity, as the surface warms by more than twice the amount under *abrupt4xCO₂* conditions compared to *abrupt2xCO₂* (Poletti et al., 2024). Based on the above, careful consideration of definitions is essential when comparing the climate sensitivity of various models.

So far, climate sensitivity has been examined from a model development perspective. There is, however, substantial value in quantifying real-world climate sensitivity − in other words, how susceptible is our planet to warming in response to rising GHG concentrations? There is ongoing debate about whether ECS is an appropriate metric for this purpose (e.g. Knutti et al., (2017)), as the *abrupt2xCO_2* scenario associated with ECS is highly idealized. Consequently, efforts are underway to quantify climate sensitivity using other lines of evidence, such as observationally constrained climate model simulations over the historical period (Otto et al., 2013; Skeie et al., 2018; Tokarska et al., 2020a). Since these estimates are inferred from a non-equilibrated climate, they are generally referred to as EffCS. The EM−GC model has previously been used by McBride et al., (2021) to quantify climate sensitivity based on the historical GMST record, and to compare these estimates to the climate sensitivity of CMIP6 climate models obtained with the Gregory-method. While McBride et al., (2021) used the term ECS in their analysis, these estimates are better referred to as EffCS.

Recently, an intriguing new method was proposed to connect the EffCS inferred from the historical GMST record to ECS (Forster et al., 2021a), as described below. Based on Eq. (1.1) and Fig 1.4, any value of EffCS can be interpreted in the context of a linear N−T relationship. The slope of this linear relationship is the inverse of the time-invariant *effective feedback parameter*, α_{eff} (Rugenstein and Armour, 2021). As shown in Fig. 1.4, there exists a second trendline, and a corresponding feedback parameter, termed the *equilibrium feedback parameter* α_{eq}, for which Eq. (1.1) yields the same ECS that would otherwise be obtained by running the model until full equilibration (Rugenstein and Armour, 2021). These two trendlines differ only in their slopes, which is a result of the difference between α_{eq} and α_{eff}. Consequently, the true ECS can be approximated from observationally constrained estimates of EffCS by applying a correction factor

to the slope, termed α', which accounts for the difference between α_{eff} and α_{eq}. Chapter 2 of this dissertation leverages this approach to quantify the magnitude of ECS using observationally constrained EM−GC simulations and estimates for the value of α' provided by the IPCC AR6 report (Forster et al., 2021a). This work contributes to the effort to connect ECS with EffCS inferred from the historical climate record, which has seen widespread interest in recent years (Armour, 2017; Proistosescu and Huybers, 2017; Andrews et al., 2018; Dong et al., 2020; Winton et al., 2020).

1.3.3.2 Ocean Heat Export

The previous section established the connection between the surface temperature response of coupled models and the global energy balance concept. Since RCMs aim to simulate the surface temperature response in a similar but simplified manner compared to coupled models, *abrupt4xCO₂* simulations are useful for assessing how well an RCM captures the rise in surface temperatures in response to an abrupt increase in RF.

Over 90% of EEI is absorbed by Earth's oceans (Forster et al., 2021a). Consequently, in RCMs, the term N is commonly considered equal to the amount of energy absorbed by Earth's oceans (Ocean Heat Export, OHE) (Gregory et al., 2004). In RCMs that use Eq. (1.1) to simulate the surface temperature response to changes in RF, the quantity N serves as the mathematical representation for OHE. This mathematical representation differs between individual models, however. Fig. 1.5 shows the surface temperature response of an atmosphere-ocean GCM (AOGCM) during an *abrupt4xCO₂* simulation, while the other lines correspond to various simplified representations of OHE, as described below. The surface temperature response of a GCM shown in Fig. 1.5 can be separated into two main components: a short-term component

associated with rapid warming, and a long-term component where the surface temperatures rise at a slow, but steady rate (Held et al., 2010).

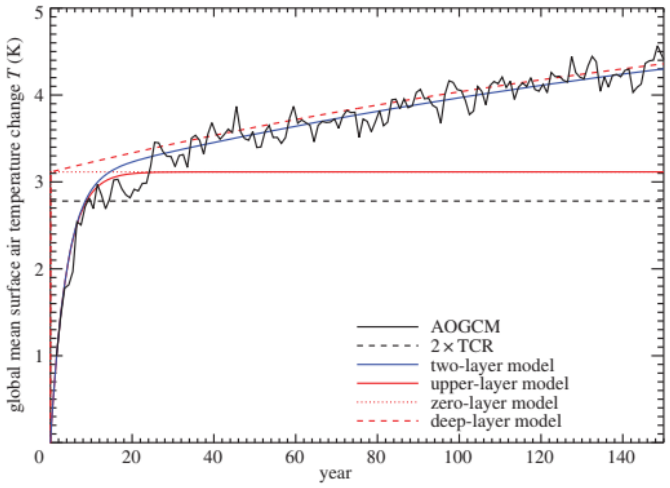

Fig. 1.5: Simulated surface temperature response of various representations of OHE under abrupt4xCO_2 conditions. Reproduction of Fig. 2 of Gregory et al., (2015).

The simplest way to model OHE is often referred to as the zero-layer model (dotted red line in Fig. 1.5). The zero-layer model provides a highly simplified representation of OHE with a low computational cost, by assuming that the ocean consists of a single layer of infinite heat capacity (Gregory et al., 2015). The temperature response of this model under *abrupt4xCO_2* conditions is highly inconsistent with that of GCMs both on the short and long timescales. Importantly, however, the RF of the climate rarely changes in such an abrupt manner, and the continuous rise in RF can be approximated as a series of small, abrupt changes between the timesteps of the model (Good et al., 2011). Under such circumstances, the zero-layer model can serve as a useful but highly simplified representation of OHE. The initial version of the EM−GC model (Canty et al., 2013) employed an OHE representation highly similar to the zero-layer model.

The infinite heat capacity of oceans in the zero-layer model corresponds to the fact that the oceans do not warm in response to radiative forcing, thereby acting as infinite heat sinks.

Consequently, the change in surface temperature over longer timescales is underestimated due to the excessive heat loss to the oceans. This issue was addressed in Hope et al., (2020), who introduced a series of updates to the ocean module of EM−GC. The representation of OHE introduced into EM−GC by Hope et al., (2020) assumes that the oceans are comprised of two layers of finite heat capacity, and that the amount of heat stored in the upper layer of the oceans is about ~14% of the total ocean heat content. This updated ocean module provides a surface temperature response to abrupt changes in RF similar to the "deep-layer model" representation (Gregory et al., 2015) shown in Fig. 1.5 (dashed red line), albeit through a different mathematical formulation from the equations presented in Gregory et al., (2015). The finite heat capacity allows oceans to warm in response to RF, enabling the model to capture the long-term warming of the climate system under *abrupt4xCO_2* conditions. Since a continuous increase in RF can be treated as a series of small, abrupt changes to RF, this version of EM−GC can also capture the long-term warming in response to a continuous rise in RF. This ability was leveraged in Hope et al., (2020), McBride et al., (2021) and Chapter 2 of this dissertation to provide projections of the warming at the end of the century under a variety of emissions scenarios.

The main weakness of the ocean module implemented by Hope et al., (2020) is the immediate temperature response to an abrupt change in RF, which corresponds to an overestimation of warming relative to GCMs during the first few years after the shock in RF. The sudden reduction of sulfur emissions from international shipping in 2020 corresponds to a sudden increase in RF (Gettelman et al., 2024), and therefore, the ocean representation of Hope et al., (2020) is not suitable for studying the short-term effects of the IMO regulations on the GMST. Chapter 3 of this dissertation introduces an updated ocean module to the EM−GC model, which follows the same core equations as the "two-layer model" representation shown in Fig. 1.5,

allowing EM−GC to better capture the changes in GMST in response to an RF shock compared to earlier versions of the model.

1.4 Policy-relevant Climate Scenarios

Climate modelling efforts rely heavily on a set of standardized scenarios to simulate how the emissions of GHGs and tropospheric aerosols influence the global climate. The design of these emissions scenarios is closely tied to IPCC Assessment reports, and involves a multi-step process depicted in Fig. 1.6. The bottom part of Fig. 1.6 shows the steps of scenario development and subsequent simulations of how anthropogenic activity affects Earth's climate, various ecosystems, and human welfare. The top part of Fig. 1.6 shows the types of models that are used to perform simulations in each step by the various Working Groups (WGs) of IPCC. This dissertation focuses on steps 2−4, that is, the relationship between emissions of GHGs and aerosols, and climate model projections.

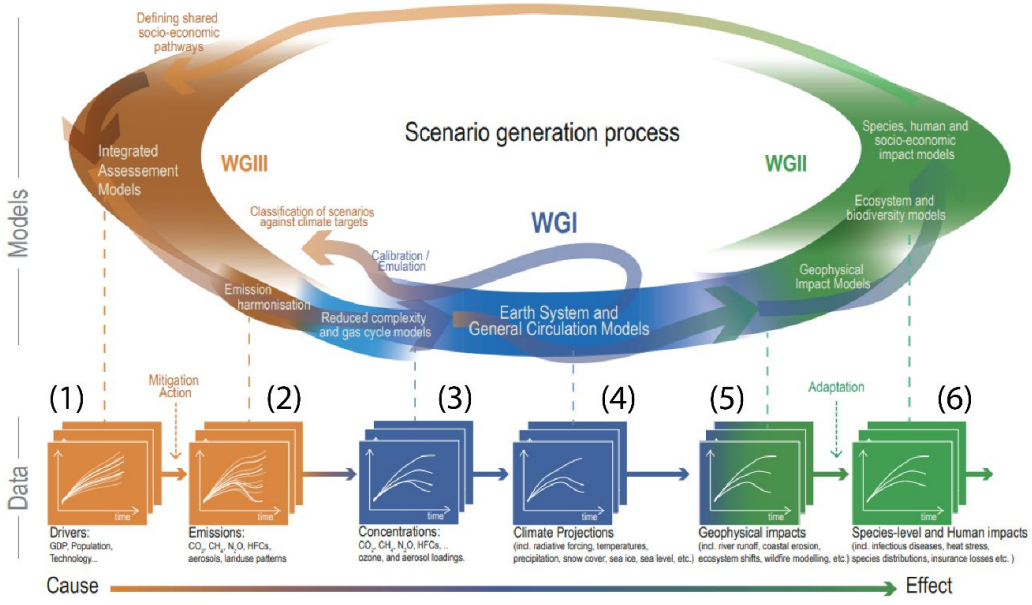

Fig. 1.6: Schematic representation of the process of climate scenario development. Reproduction of Figure 1.27 of IPCC AR6 (Chen et al., 2021).

The first step in the development of climate scenarios is performed by the socioeconomic modelling community using Integrated Assessment Models (IAMs). IAMs simulate a variety of socioeconomic factors, such as changes in population and per capita GDP in different parts of the world. These quantities are directly related to the emissions of GHGs and aerosols, which are among the primary outputs of IAM simulations. The emissions of GHGs can be used directly as inputs to Earth System Models (ESMs), which are able to compute the concentration and radiative forcing due to GHGs and aerosols, as well as the resulting changes in regional and global climate. Such simulations require a large amount of computational power and, therefore, are not yet common. Instead, simplified climate models are often used to compute the "best estimate" time series of GHG concentrations from emissions (Meinshausen et al., 2020). These time series are then used either as direct inputs for models that compute RF from atmospheric concentrations internally, or are converted to RF using so-called conversion formulas, such as the ones described in Myhre et al., (1998) and Meinshausen et al., (2020).

The IPCC AR6 report introduced several updates to the process described above. These changes include an updated computation of the "best estimate" concentrations, as well as revised conversion formulas between RF and atmospheric concentrations. Such adjustments to the process raise the question of how the output of climate model simulations, such as the simulated rise in GMST, are affected by the updates introduced in IPCC AR6. Chapter 2 of this dissertation focuses on these questions by providing forecasts of the GMST under the most recent set of climate scenarios, termed Shared Socioeconomic Pathways (SSPs). Such forecasts were previously provided by McBride et al., (2021) for several SSP scenarios, but those simulations were based on datasets that predated the AR6 report. Consequently, the simulations described in Chapter 2 are valuable for assessing how forecasts of future warming and the projected likelihood of achieving

the goals of the Paris Agreement were affected by the AR6 updates to the formulation of radiative forcing.

1.5 Technical updates to the EM−GC modelling framework

This dissertation focuses on using the Empirical Model of Global Climate (EM−GC) to study a variety of policy-relevant questions described in Sect. 1.1. To perform these model simulations, a series of updates to the input datasets and to the code of the model have been introduced, which are summarized in this section. Updates to the EM−GC modelling framework presented in this dissertation include:

- Inclusion of updated ERF datasets obtained from Annex III of AR6, relative to earlier versions of the model, which used datasets based on AR5 and the SSP database
- Update to the aerosol-weighting method introduced by McBride et al., (2021), to allow the model to use the AR6 estimates of ERF_{AER} for weighting the EM−GC probabilistic ensemble
- Additional updates to the aerosol-weighting method, providing the user with greater control over the range of uncertainty in ERF_{AER} used for weighting the EM−GC ensemble
- Adoption of a new method to estimate ECS through the use of a correction factor applied to the climate feedback parameter
- Replacement of the EM−GC ocean module with a new, two-layer energy balance component based on the formulations of Held et al., (2010) and Geoffroy et al., (2013b)
- Conceptualization and development of the observation-driven calibration of the two-layer EBM component of the model, and conducting a series of benchmark simulations with the updated ocean module

- Inclusion of new, updated observational datasets for internal variability
- Development and redesign of several supporting codes to provide greater flexibility in processing model inputs and outputs

The technical updates listed above provide considerable improvements to several modules of the model, while also increasing the flexibility of the modelling workflow.

Chapter 5 of this dissertation provides proposals for additional improvements to further extend the flexibility and applicability of the EM−GC model. First, Chapter 5 proposes additional updates to the treatment of the global energy balance and ocean heat export within EM−GC, as well as to the consideration of the uncertainty in the temporal evolution of both ERF_{AER} and the strength of climate feedback. Second, Chapter 5 provides recommendations for other policy-relevant model simulations, focusing both on updated emissions scenarios, as well as short-term mitigation opportunities through the reduction of black carbon emissions.

Chapter 2: AR6 Updates to the RF of GHGs and Aerosols Lowers the probability of Accomplishing the Paris Agreement Compared to AR5 Formulations

2.1 Introduction

The Paris Agreement (PA), negotiated in 2015, established the goal of limiting global warming to 1.5 ºC (PA target) relative to the pre−industrial baseline, with an upper limit of 2.0 ºC (PA upper limit). Forecasting the rise in global mean surface temperature, for various estimates of the future atmospheric abundances of greenhouse gases and aerosols, is important for assessing the feasibility of accomplishing the goal of the PA.

Numerous modeling efforts focus on assessing the feasibility of various climate policies, and the implications of these policies on various elements of Earth's climate. Earth System Models (ESMs) are the most comprehensive climate models available and are the primary tool of global warming research. Although ESMs are able to compute the atmospheric concentration of CO_2 from emissions, most often these models use prescribed time series of atmospheric CO_2 (Jones et al., 2016; Lawrence et al., 2016; Meinshausen et al., 2020). For non-CO_2 GHGs, ESMs of Phase 6 of the Coupled Model Intercomparison Project (CMIP6), also use prescribed atmospheric concentration trajectories (Meinshausen et al., 2020). While there is an effort to make ESMs emissions-based for more greenhouse gases (GHGs) (Meinshausen et al., 2024), many ESMs will need to continue to rely on concentration input for many non-CO_2 GHGs.

Reduced Complexity Climate Models (RCMs) are used to compute "best estimate" GHG concentration trajectories from emissions for various scenarios, which can serve as an input to ESMs (Smith et al., 2018a; Meinshausen et al., 2020; Meinshausen et al., 2024). RCMs require substantially lower computational resources than ESMs and allow the exploration of a wide variety of possible emissions scenarios. Outputs from RCMs serve as the basis for projections of

atmospheric abundances of CO_2, CH_4, N_2O and other GHGs that constitute the Shared Socioeconomic Pathways (SSPs) (Meinshausen et al., 2020).

Chapters 10 (Bindoff et al., 2013) and 11 (Kirtman et al., 2013) of the 2013 IPCC Report (IPCC, 2013b) raised the possibility that "some CMIP5 models have a higher transient response to GHGs and a larger response to other anthropogenic forcings (dominated by the effects of aerosols) than the real world". The tendency of ESMs to warm more quickly than the observed rise in global mean surface temperature (GMST) over the past three to four decades has also been noted for CMIP6 model output (Tokarska et al., 2020b; Zelinka et al., 2020; McBride et al., 2021). Hausfather et al. (2022) recently termed this tendency the "hot-model problem". Nicholls et al. (2021) examined future projections of GMST from a suite of RCMs and concluded that "the most extreme CMIP6 model projections [of GMST] are outside the range of most RCMs' 5−95th percentiles [of GMST]".

The Physical Science Basis document published in 2021 (IPCC, 2021b), commonly known as the Sixth Assessment Report (AR6), provided important updates to the projections of future abundances of GHGs and aerosols compared to previously published values in the SSP database (Riahi et al., 2017; van Vuuren et al., 2017; Fricko et al., 2017; Fujimori et al., 2017; Calvin et al., 2017; Kriegler et al., 2017; Rogelj et al., 2018). Furthermore, AR6 also updated values of the effective radiative forcing (ERF) due to the major GHGs and aerosols relative to the Fifth Assessment Report (AR5) (IPCC, 2013b).

In this paper, we review the changes to the projections of GHGs and aerosols, as well as the ERF formulations adapted by AR6, and compare to prior SSP-based projections of the radiative forcing due to GHGs and aerosols (Sect. 2.2.3). Then, we use our multiple linear regression energy balance RCM, the Empirical Model of Global Climate (EM−GC, Sect. 2.2.4), (Canty et al., 2013;

Mascioli et al., 2012; Hope et al., 2017; McBride et al., 2021), to assess the implications of the AR6 updates on Effective Climate Sensitivity (EffCS, Sect. 2.3.1), the rate of warming due to human activity (Attributable Anthropogenic Warming Rate, AAWR; Sect. 2.3.1), and projected future warming (Sect. 2.3.2) for a large ensemble of aerosol trajectories. A major strength of our EM−GC is the ability to provide probabilistic forecasts of the future rise in GMST for each SSP scenario, based upon the uncertainty in climate feedback and the radiative forcing due to tropospheric aerosols (Canty et al., 2013; Mascioli et al., 2012; Hope et al., 2017; McBride et al., 2021). Therefore, we conclude the paper by comparing the likelihood of achieving the target (1.5 ºC warming in 2100) and upper limit (2.0 ºC) of the Paris Agreement within the two frameworks, for various SSP scenarios (Sect. 2.3.2).

Previous projections of the GMST anomaly found using our EM-GC (McBride et al., 2021) show good agreement with results from other RCMs that participated in the reduced complexity model intercomparison project (RCMIP) exercise (Nicholls et al., 2020; Nicholls et al., 2021). In particular, projections of GMST from our model showed good agreement with results from the Model for the Assessment of Greenhouse Gas Induced Climate Change (MAGICC7) RCM (Meinshausen et al., 2011a; Meinshausen et al., 2011b; Meinshausen et al., 2020), that was used for the computation of GHG trajectories adapted by AR6. Consequently, the EM−GC simulations presented here should serve as a good reference point for the impact of the new AR6 ERF time series on projections of the GMST anomaly found using other RCMs.

2.2 Data and Methods

2.2.1 Shared Socioeconomic Pathway Scenarios

Shared Socioeconomic Pathway (SSP) scenarios are used to represent various future outcomes in the emissions of GHGs and tropospheric aerosols, as well as aerosol precursors. SSP

scenarios are denoted with the nomenclature SSPx−y, where x represents the identifier of the baseline SSP pathway (1−5) related to mitigation and adaptation, and y is the target radiative forcing (in W m^{-2}) at the end of the century (commonly referred to as headline or nameplate RF) (O'Neill et al., 2014). As an example, SSP1−2.6 aims to keep anthropogenic ERF close to 2.6 W m^{-2} in the year 2100 under a sustainable socioeconomic pathway. Different baseline SSP pathways associated with the same nameplate RF represent the notion that various socioeconomic trajectories can lead to a similar end-of-century RF (O'Neill et al., 2016). AR6 provides a detailed description of nine Tier 1 and Tier 2 (O'Neill et al., 2016) SSP scenarios (Chen et al., 2021). Of these nine scenarios, we extensively analyze the following four: SSP1−1.9, SSP1−2.6, SSP4−3.4, SSP2−4.5.

2.2.2 Modeling Framework

We assess the impact on global warming projections of changes to the ERF datasets to GHGs and aerosols introduced by AR6. We define two frameworks, a Baseline Framework that represents the state of knowledge prior to AR6, and an AR6 Framework based on ERF data from Chapter 7 and Annex III of AR6 (Forster et al., 2021a; IPCC, 2021a; Smith et al., 2021b; Smith et al., 2021a).

For the Baseline Framework, ERF for GHGs is primarily based on GHG concentrations from the SSP database (Riahi et al., 2017; van Vuuren et al., 2017; Fricko et al., 2017; Fujimori et al., 2017; Calvin et al., 2017; Kriegler et al., 2017; Rogelj et al., 2018) converted to ERF using the formulae from AR5, as described in Sect. 2.5.3. The ERF due to tropospheric aerosols in the Baseline Framework considers six aerosol types: sulfate, mineral dust, ammonium-nitrate, fossil fuel organic carbon, fossil fuel black carbon and biomass burning organic and black carbon based on data from the Potsdam Institute for Climate Research (Meinshausen et al., 2011c), (Sect. 2.5.3).

ERF input data for the AR6 Framework is obtained from Annex III and Chapter 7 of the AR6 report (Forster et al., 2021a; IPCC, 2021a; Smith et al., 2021b; Smith et al., 2021a) as described in Sect. 2.2.5.4.

2.2.3 Effective Radiative Forcing

Effective Radiative Forcing (ERF) is described as the top-of-the-atmosphere (TOA) energy flux difference (in W m^{-2}) due to an imposed perturbation (Myhre et al., 2013b; Boucher and Randall, 2013; Sherwood et al., 2015; Forster et al., 2021a). ERF accounts for both tropospheric and stratospheric temperature adjustments (Smith et al., 2018b; Forster et al., 2021a), and as such is more representative of the impacts of various forcing agents on the GMST anomaly than stratospheric-temperature-adjusted RF (SARF) or instantaneous RF (IRF) (Forster et al., 2021a). ERF describes Earth's energy imbalance due to anthropogenic factors such as GHGs and tropospheric aerosols; hence, ERF is connected quantitatively to the anomaly in GMST that is central to projections of global warming.

2.2.3.1 Effective Radiative Forcing

ERF from GHGs can be computed from their atmospheric concentrations (Byrne and Goldblatt, 2014). Formulations of Myhre et al. (1998) based on results from a line-by-line model (Edwards, 1992; Myhre and Stordal, 1997) were the generally accepted method for converting atmospheric concentrations to radiative forcing for GHGs. These parametrizations were adapted by multiple IPCC reports (TAR, AR4, AR5) (IPCC, 2001, 2007, 2013b). Updates to these formulations, based on the Oslo line-by-line model (Myhre et al., 2006) were provided by Etminan et al. (2016) and Meinshausen et al. (2020), with the latter being adapted into Chapter 7 of the AR6 report (Forster et al., 2021a). The formulations by Etminan et al. (2016) and Meinshausen et al. (2020) account for the band overlaps between CO_2 and N_2O, include shortwave forcing from CH_4,

and provide an update to the water vapor continuum. Both of these formulations have their own respective advantages and limitations, as discussed in Section 2.7 of Meinshausen et al. (2020) and Section 7.SM.1.1 of AR6 (Smith et al., 2021a).

The AR5 and AR6 formulations are used to compute time series of SARF for each GHG, based on time series of historical and future concentrations of GHGs. In the AR5 RF formulations, SARF computed with the formulations of Myhre et al. (1998) was considered to be equal to ERF, based on an analysis of the RF due to CO_2 by Vial et al. (2013). Since no similar analyses were available for other GHGs, ERF was considered equal to SARF for all other well-mixed GHGs in AR5 (Forster et al., 2021a). In AR6, tropospheric adjustments for CO_2, CH_4 and N_2O are assessed to be non-zero (see Sections 7.3.2 and 7.3.5.1 of Forster et al. (2021a) for further detail). Consequently, the formulations for ERF given by AR6 allow for tropospheric adjustments, whereas the formulations given by AR5 allow for only stratospheric adjustments.

Annex III of the AR6 report (IPCC, 2021a) adapted not only the ERF formulae described in Meinshausen et al. (2020), but also projections for GHG concentrations for various SSP scenarios published in the same paper. Here and throughout, we consider concentration to be synonymous with volume mixing ratio. The Meinshausen et al. (2020) GHG projections are provided using version 7 of the Model for the Assessment of Greenhouse Gas Induced Climate Change (MAGICC7) RCM (Meinshausen et al., 2011a; Meinshausen et al., 2011b; Meinshausen et al., 2020). Prior to the release of the AR6 report, one of the most up-to-date sources for GHG concentrations for various SSP scenarios was the SSP database (Riahi et al., 2017; van Vuuren et al., 2017; Fricko et al., 2017; Fujimori et al., 2017; Calvin et al., 2017; Kriegler et al., 2017; Rogelj et al., 2018). These concentration projections were computed with version 6.8 of the MAGICC model, based upon emissions data from various Integrated Assessment Models (IAMs) (Riahi et

al., 2017), that were also published in the SSP database. Meinshausen et al. (2020) computed the GHG concentrations using the same GHG emissions database with a newer version of the MAGICC model. MAGICC7 includes several updates and changes to certain gas cycles, as well as the enablement of the permafrost feedback module of the model, which results in additional emissions of CO_2 and CH_4 from the melting of permafrost.

Figure 2.1 shows the time evolution of the concentration (Fig. 2.1a−c) and ERF (Fig. 2.1d−f) for CO_2, CH_4 and N_2O within the Baseline and AR6 Frameworks, as well as ERF from tropospheric aerosols (ERF_{AER}), the total ERF from all GHGs, and ERF from overall anthropogenic activity (Fig. 2.1g−i). There is a considerable difference between the Baseline and AR6 datasets, particularly for SSP4−3.4 and SSP2−4.5. Concentrations of CO_2 are larger within the AR6 Framework by as much as 30 ppm (Fig. 2.1a) in the year 2100 compared to the Baseline. Projected concentrations of CH_4 within the AR6 Framework are much higher for SSP2−4.5 and SSP4−3.4, compared to the Baseline. For the three major GHGs, an increase for the ERF was found in the AR6 Framework for most SSP scenarios, with a particularly high increase for ERF_{CO2} and ERF_{CH4} of SSP2−4.5 and SSP4−3.4 (Fig. 2.1d−f). This increase can be attributed to a combined effect of the increase in projected GHG concentrations (Fig. 2.1a−c) and the updated ERF formulations of Meinshausen et al. (2020), as well as updates to the tropospheric adjustments of RF (Smith et al., 2018b; Hodnebrog et al., 2020; Forster et al., 2021a).

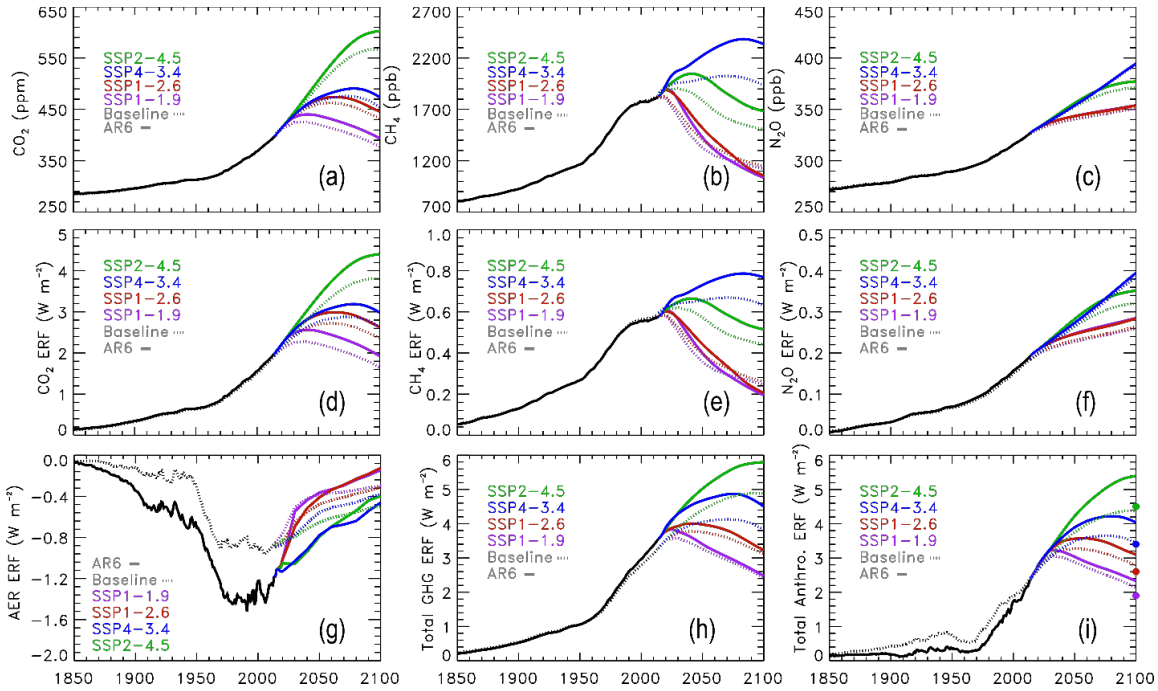

Figure 2.1: Concentrations and ERF due to various forcing agents for the Baseline (dashed) and AR6 (solid) frameworks. Colors represent SSP scenarios, as indicated on the individual panels. (a) Concentration of CO_2. (b) Concentration of CH_4. (c) Concentration of N_2O. (d) ERF from CO_2. (e) ERF from CH_4, including ERF from the enhancement of stratospheric water vapor due to methane. (f) ERF from N_2O. (g) ERF due to tropospheric aerosols. (h) ERF from all GHGs, including halogens and tropospheric O_3, as well as land-use change. (i) Total anthropogenic ERF. Colored circles on the right−hand axis represent the target ERF of each SSP scenario as indicated in the name of the scenario.

AR6 adapted the SARF formulations of Meinshausen et al. (2020) for CO_2, CH_4 and N_2O, replacing the formulae of Myhre et al. (1998) used in previous IPCC Assessment Reports (Table 2A.1). To convert $SARF_{CO2}$ to ERF_{CO2}, an additional +5% tropospheric adjustment was also introduced in AR6 (Forster et al., 2021a). This tropospheric adjustment increases ERF_{CO2} by as much as 0.2 Wm^{-2} in the year 2100 for SSP2−4.5. Concentration projections for CO_2 in Annex III of AR6 (IPCC, 2021a; Smith et al., 2021b) − which are largely based on Meinshausen et al. (2020) – are also higher than the concentration projections within the SSP Database (Riahi et al., 2017; Fricko et al., 2017; Calvin et al., 2017). Thus, the combination of increased projections on the concentration of CO_2 and updates to the conversion of CO_2 concentrations to ERF introduced in

AR6 result in increased projections of ERF_{CO2} within the AR6 Framework relative to the Baseline, for all four SSP scenarios studied (Fig. 2.1d).

The inclusion of permafrost emissions of methane result in as much as 50 ppb increase in the atmospheric concentration of methane in 2100, for the scenarios studied in our work (Fig. 3b of Meinshausen et al. (2020)). However, the inclusion of permafrost emissions does not fully account for the difference in the projected concentration of CH_4 between the Baseline and AR6 Frameworks (Fig. 2.1b).

Updates to the atmospheric lifetime of CH_4 were introduced in MAGICC7 resulting in a shorter average lifetime for low radiative forcing scenarios, and longer lifetimes for high forcing scenarios (Sect. 2.4.1 of Meinshausen et al. (2020)). This update, alongside updates to the parametrization of the CH_4 cycle in MAGICC7 result in the difference between the projected CH_4 concentrations within the Baseline and AR6 frameworks for SSP4−3.4 and SSP2−4.5 depicted in Fig. 2.1b. In 2100, the atmospheric concentration of CH_4 is projected by Meinshausen et. al. (2020) to be higher by 180 ppb and 400 ppb for SSP2−4.5 and SSP4−3.4, respectively, compared to the projections in the SSP database (Riahi et al., 2017; Fricko et al., 2017; Calvin et al., 2017). These findings are consistent with Meinshausen et al. (2020) who concluded "the comparison of mid-century CO_2 and CH_4 concentrations also reveals that the main reason for higher implied warming of SSP4-3.4 in comparison to SSP1-2.6 are elevated CH_4 concentrations".

While the difference in the projected concentration of CH_4 between our two frameworks is considerable for SSP4−3.4 and SSP2−4.5, the increase in ERF_{CH4} is proportionally smaller in magnitude. The comparably smaller increase in ERF_{CH4} is mostly due to the application of a multiplicative factor of 0.86 used to relate the new SARF formulation of CH_4 to ERF. This 14% reduction offsets a significant portion of the would-be increase in ERF due to CH_4 caused by higher

projected concentrations and spectroscopy−based updates to the formulation of SARF (Forster et al., 2021a). Section 7.3.2.2 of AR6 (Forster et al., 2021a) assesses the uncertainty in the multiplicative factor used to relate SARF to ERF to be ±0.15, which introduces a sizeable new uncertainty in the radiative forcing of CH_4 for all of the SSPs. Overall, we find a major increase in the ERF_{CH4} within the AR6 Framework compared to the Baseline for SSP4−3.4 and SSP2−4.5, driven by the elevated concentration projections of CH_4. In contrast, differences in ERF_{CH4} between the Baseline and AR6 Frameworks for SSP1−1.9 and SSP1−2.6 are quite small.

New parametrizations in MAGICC7 were also introduced for N_2O (Meinshausen et al., 2020). These parametrizations result in a minimal increase in the projected concentrations shown on Fig 2.1c. A small increase in ERF_{N2O} is found between the two frameworks for all four SSP scenarios (Fig. 2.1f), mostly attributable to the +7 ± 13% tropospheric adjustment described in Section 7.3.2.3 of AR6 (Forster et al., 2021a).

2.2.3.2 Tropospheric Aerosols and Overall Anthropogenic ERF

Tropospheric aerosols (AER) exhibit an overall cooling effect on the atmosphere, both by directly reflecting and absorbing incoming radiation (aerosol direct effect), and through interactions with clouds (aerosol indirect effect) (Forster et al., 2021a). ERF from these two factors is usually denoted ERF_{ari} and ERF_{aci}, respectively. We use ERF_{AER} to denote the total ERF due to tropospheric aerosols (ERF_{ari} + ERF_{aci}).

In AR5, the best estimate of the ERF_{AER} was assessed to be −0.9 Wm^{-2}, for the time period 1750−2011. In AR6, the best estimate of ERF_{AER} was determined to be −1.1 Wm^{-2}, between 1750−2019 (Forster et al., 2021a). The corresponding 5th and 95th percentile ranges were −0.1 to −1.9 Wm^{-2} in 2011 and −0.4 to −1.7 Wm^{-2} in 2019, for the AR5 and AR6 assessments,

respectively. AR6 also provided the assessment of −1.3 [range −0.6 to −2.0 Wm^{-2}] for the 1750−2014 period. We use the 1750−2019 time period below.

Furthermore, AR5 assessed ERF_{ari} and ERF_{aci} to be nearly equal in magnitude (see Fig. 8.15 of AR5 (Myhre et al., 2013b)). A major difference between these two assessments of ERF_{AER} is that, in AR6, it was stated that the cooling due to the aerosol indirect effect (ERF_{aci}) is much larger than the cooling due to the direct effect (ERF_{ari}). The change of ERF_{AER} by AR6 to a value that exhibits more cooling, for a time period that is 8 years more recent than the 2011 end year used by AR5 implies a major shift in the shape of ERF_{AER} as a function of time, because tropospheric aerosol loading is believed to have declined over the past two decades due to successful air quality regulations implemented throughout the world (Smith and Bond, 2014; Fu et al., 2021).

The methodology to develop the time evolution of RF due to aerosols in AR6 is partially based on the modeling study of Smith et al. (2021c). Similarly to GHGs, there is a direct relationship between ERF_{AER} and the atmospheric abundance of various types of aerosols, which is commonly expressed as a relation between the ERF and the emission of aerosols and aerosol precursors. The parametrization used in AR6 assumes that ERF_{ari} scales linearly with the emissions of various types of aerosol precursors (Smith et al., 2018a; Smith et al., 2021c), while the relation between ERF_{aci} and emissions is logarithmic (Carslaw et al., 2013; Ghan et al., 2013; Stevens, 2015; Smith et al., 2018a; Smith et al., 2021c). Smith et al. (2021c) used aerosol ERF from various CMIP6 models, which were decomposed to the direct and indirect components using the Approximate Partial Radiative Perturbation (APRP) method (Taylor et al., 2007; Zelinka et al., 2014), from which coefficients for the linear and logarithmic relations (for ERF_{ari} and ERF_{aci}, respectively) for each CMIP6 model were determined.

Next, Smith et al. (2021c) created a large ensemble of ERF_{AER} time series of various shapes and magnitudes by a Monte-Carlo sampling around the sets of coefficients obtained from the CMIP6 model-based fits. This aerosol ensemble accounts for the uncertainty in both the historical time evolution and the magnitude of ERF_{AER}. This methodology is adapted by Chapter 7 of AR6 for ERF_{aci}, as described in Sections 7.SM.1.3 and 7.SM.1.4 of AR6 (Smith et al., 2021a). The median of the ensemble is adapted as the best estimate for the historical time series of ERF_{aci}, scaled to match a value of −1.0 Wm^{-2} for 1750 to 2005−2014. For ERF_{ari}, AR6 uses the same assumption of a linear connection between aerosol emissions and forcing (Smith et al., 2018a; Smith et al., 2021c), but unlike Smith et al. (2021c), also considers emissions of NH_3. Additionally, the AR6 report does not use a Monte-Carlo ensemble to derive a best estimate time series for ERF_{ari} (and corresponding coefficients). Instead, AR6 determines coefficients such that the contributions from the individual aerosol precursor species match the values derived from Myhre et al. (2013c), as described in Section 7.SM.1.3.2 of the AR6 report (Smith et al., 2021a). The AR6 methodology provides a single set of "best estimate" coefficients that can be used to convert emissions data to a time series of ERF_{ari} and ERF_{aci}, and consequently, ERF_{AER}.

In our model framework, the radiative forcing of aerosols is treated in a probabilistic manner that expands upon the single best estimate ERF_{AER} time series that is associated with each SSP. Therefore, the comparison of single ERF_{AER} time series shown in Fig. 2.1g highlights only a portion of the difference between the Baseline and AR6 Frameworks.

There are two major takeaways from Fig. 2.1g. First, for SSP2−4.5 and SSP4−3.4, aerosol cooling is much stronger between 2020 and 2060 in the AR6 Framework compared to the Baseline, whereas for SSP1−1.9 and SSP1−2.6, aerosol cooling is similar or weaker within the AR6 Framework than in the Baseline. In general, for all four SSP scenarios, the rate of decline in aerosol

cooling is more rapid within the AR6 Framework relative to the Baseline. Second, if we use the aerosol ensemble member from our probabilistic treatment that corresponds to the best estimate of ERF_{AER} in the Baseline Framework (−0.9 Wm^{-2} in 2011 from AR5) as well as the best estimate in the AR6 Framework (−1.1 Wm^{-2} in 2019) to compute the overall anthropogenic ERF for the respective Frameworks (Fig. 2.1i), the total anthropogenic ERF between 1850 and 2019 is lower in the AR6 framework compared to the Baseline, whereas the rise in total anthropogenic ERF between 1950 and 2019 is more pronounced within the AR6 framework (black dotted and solid lines, Fig. 2.1i). This difference has important implications for our estimates of the rate of warming due to human activity, which we discuss in Sect. 2.2.4.

Finally, we highlight how total anthropogenic ERF at the end of the century considerably exceeds, by as much as 0.7 Wm^{-2} for SSP2−4.5, the nameplate RF target for each of the four SSP scenarios (Fig. 2.1i). At the time the SSP scenarios were constructed, the value of the nameplate RF at the end of the century was designed to be interpreted as SARF (Tebaldi et al., 2021). The original purpose of the nameplate RF metric was to provide a numerical representation of a certain climate outcome (O'Neill et al., 2016). As highlighted by Sect. 7.3.1 of AR6 (Forster et al., 2021a), "AR5 recommended ERF as a more useful measure of the climate effects of a physical driver than [SARF] adopted in earlier assessments". Additionally, as described above, AR5 considered SARF to be equal to ERF, while this is no longer the case for AR6. Thus, in AR5-consistent settings, the nameplate RF of a given SSP scenario could be interpreted as either SARF or ERF. Lastly, RF for tropospheric aerosols is computed as ERF directly from emissions in AR6 (Smith et al., 2021a), which leads to additional differences with the end-of-century design of the original SSPs. As such, we conclude that the end-of-century RF is larger than the nameplate target for all four SSPs.

2.2.4 Empirical Model of Global Climate

To quantify the impacts of the updates to ERF datasets outlined above on AAWR, EffCS, and projected warming, we use the Empirical Model of Global Climate (EM−GC) model (Canty et al., 2013; Mascioli et al., 2012; Hope et al., 2017; McBride et al., 2021). EM−GC uses a multiple linear regression energy balance approach and computes the GMST anomaly (ΔT_{MDL}) based on anthropogenic ERF and natural factors as shown in Eq. (2.1).

$$\Delta T_{MDL,i} = \frac{1+\gamma}{\lambda_p}\left(\Delta ERF_{GHG,i} + s \times \Delta ERF_{AER,i} + \Delta ERF_{LUC,i} - Q_{OCEAN,i}\right) + C_0 + C_1 \times SAOD_{i-6} + C_2 \times TSI_{i-1} + C_3 \times ENSO_{i-2} + C_4 \times AMOC_i + C_5 \times PDO_i + C_6 \times IOD_i \quad (2.1)$$

In Eq. (2.1), $\Delta ERF_{x,i}$ represent the effective radiative forcing from greenhouse gases (GHG), tropospheric aerosols (AER) and land use change (LUC) compared to a 1750 baseline. The model uses a monthly time grid, with *i* being the index of a specific month. The dimensionless scaling parameter, *s*, is used to account for the uncertainty in the ERF due to aerosols as described in Sect. 2.2.4.1.

The natural factors considered when modeling the GMST anomaly are Stratospheric Aerosol Optical Depth (SAOD) from volcanic eruptions, Total Solar Irradiance (TSI), El-Niño Southern Oscillation (ENSO), Atlantic Meridional Overturning Circulation (AMOC), Pacific Decadal Oscillation (PDO) and Indian Ocean Dipole (IOD), as outlined in Sect. 2.2.5.5. Similarly to previous analyses with EM−GC (McBride et al., 2021), SAOD, TSI and ENSO are lagged by 6,1 and 2 months, respectively. Additionally, EM−GC quantitatively accounts for the export of heat to Earth's oceans ($Q_{OCEAN,i}$ in Eq. 2.1), as described below.

The dimensionless parameter γ in Eq. (2.1) is defined as the sensitivity of the global climate to feedbacks due to changes in the anthropogenic ERF due GHGs, AER and LUC. γ is related to the climate feedback parameter of EM−GC (λ_Σ) as shown in Eq. (2.2):

$$1 + \gamma = \frac{1}{1-(\frac{\lambda_\Sigma}{\lambda_p})} \quad (2.2)$$

Here, λ_Σ is the sum of all climate feedbacks from factors such as water vapor, lapse rate, surface albedo and clouds. λ_p in Eqs. (2.1) and (2.2) corresponds to the response of a black body to a perturbation with no climate feedback present, with a value of 3.2 W m^{-2} $^oC^{-1}$ (Bony et al., 2006). The above mathematical representation is used in lieu of incorporating the Planck feedback into λ_Σ. For the EM−GC simulations shown below, we assume λ_Σ to be constant over time, which was found to be a very good approximation within EM−GC, as described by Sect. 3.3.6 of McBride et al. (2021).

Values of the regression coefficients C_0−C_6 in Eq. (2.1) are computed by minimizing the cost function shown in Eq. (2.3).

$$Cost\ function = \sum_{i=1}^{N_{MONTHS}} \frac{1}{\sigma_{OBS,i}^2} (\Delta T_{OBS,i} - \Delta T_{MDL,i})^2 \quad (2.3)$$

Here, $\Delta T_{OBS,i}$ and $\Delta T_{MDL,i}$ represent the observed and EM−GC modeled GMST anomaly for a given month (i), respectively, while σ_{OBS} is the 1σ uncertainty associated with each temperature observation.

EM−GC simulations quantitatively account for heat being absorbed by Earth's oceans (ocean heat export, OHE). Time−dependent OHE is computed as shown by Eq. (2.4), where the constant κ is the ocean heat uptake efficiency (in W m^{-2} $^oC^{-1}$) as expressed by Eq. (2A.1). Further details of our model treatment of OHE is given in the Supplement as well as Sect. 2.1 of McBride et al. (2021).

$$Q_{OCEAN,i} = \kappa\left(\Delta T_{ATM,HUMAN,i} - \Delta T_{OCEAN,HUMAN,i}\right) \quad (2.4)$$

Time series of the natural and anthropogenic factors between 1850 and 2019 are used as inputs to compute the coefficients (C_0−C_6) in Eq. (2.1). We refer to this step as the training of the model.

We define the historical training period as 1850−2019, and the future SSP−based projection period as 2020−2100, to be consistent with the definition of historical and SSP−based timeframes outlined in Section 7.SM.1.3 (Smith et al., 2021a) and Annex III (IPCC, 2021a) of AR6. Each fit to the historical GMST record (a set of coefficients) can be extrapolated to the future using Eq. (2.1), with effects of natural forcings zeroed out, allowing EM−GC to provide a time-dependent GMST forecast for each set of regression coefficients. The model also uses three χ^2 goodness-of-fit constraints, as summarized in Sect. 2.2.7.

Figure 2.2 shows the EM−GC best fit to the Hadley Centre Climatic Research Unit version 5 (HadCRUT5) (Morice et al., 2021) historical GMST anomaly record for the Baseline and AR6 Frameworks, assuming the IPCC best estimate RF trajectories for tropospheric aerosols shown on Fig. 2.1g. The top panels of Fig. 2.2 show the EM−GC modelled best fit (red) to the HadCRUT5 GMST record (black). Other panels represent the contribution to the modelled GMST from anthropogenic activity (Fig. 2.2c,d), as well as the natural factors of SAOD, TSI, ENSO, AMOC, PDO and IOD included in Eq. (2.1) (Fig. 2.2e−l). The bottom panels of both columns of Fig. 2.2 show the modeled (red) and measured (black) Ocean Heat Content (OHC), as well as the corresponding measurement uncertainty (blue). Description of the GMST and OHC datasets used to train the model are provided in Sect. 2.2.5. EM−GC runs simulate the amount of heat exported to Earth's oceans such that the change in modeled OHC matches the change in observed OHC, over the period where observed OHC data are available. For panel (m) of Fig. 2.2, the modeled OHC time series is initialized to zero in 1850, and the observed OHC (black line, which is an anomaly) is adjusted to match the model mean over 1955 to 2019. For panel (n), the observed OHC is identical to that shown in panel (m), and the modeled time series is again adjusted to match

the observed mean over 1955 to 2019. This final adjustment leads to a non-zero value for OHC in 1850 for the AR6 Framework run.

We provide the value of the λ_Σ and κ from Eqs. (2.1) and (2.4) on Fig. 2.2a,b and Fig. 2.2m,n, respectively. The χ^2 goodness-of-fit parameters (Sect. 2.2.7) for the modelled GMST anomaly (χ^2_{ATM}) and OHC χ^2_{OCEAN} are also provided on the same panels. The rate of increase in GMST between 1975 and 2014 due to human activity (AAWR, Sect. 2.2.6) is provided as the slope of a linear fit to the anthropogenic contribution to the GMST anomaly in this period on Fig. 2.2c,d. Similar values of AAWR are found for modest (that is, shifts within a decade) changes in the start and end year used to compute AAWR, due to the linearity of the anthropogenic contribution to GMST (orange lines in Fig. 2.2c–d).

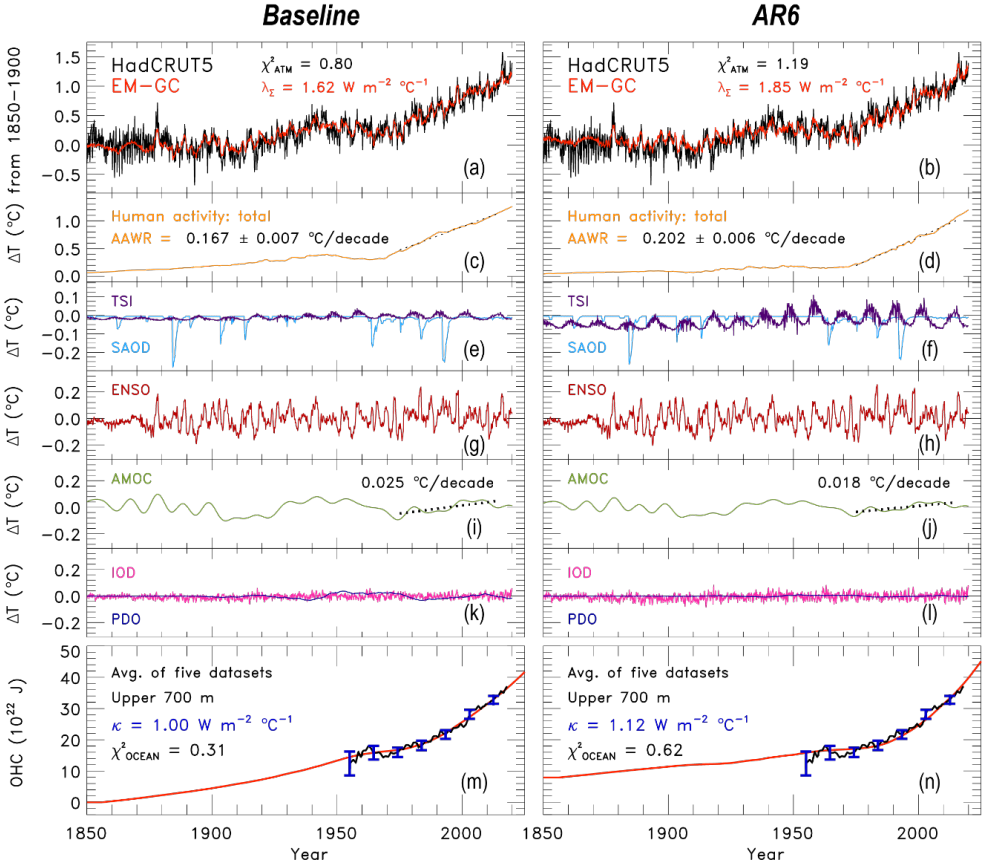

Figure 2.2: EM–GC assessed contribution of natural and anthropogenic factors to warming for the best fits to the HadCRUT5 GMST record within the Baseline (left) and AR6 (right) Frameworks. Fits are shown

for the IPCC best estimate of ERF_{AER} (see text) for each Framework. Both simulations use a training period of 1850 to 2019. (a,b) Observed (black) and modelled (red) GMST anomaly (ΔT) relative to a pre-industrial (1850−1900) baseline. Values of λ_{Σ} and χ^2_{ATM} for the best-fit simulation are shown at the top. (c,d) Contribution of anthropogenic activity to the GMST anomaly (orange). AAWR, computed as the slope of a linear fit (dashed black line) as described in Section 2.2.6 is shown at the top. The 2σ uncertainty for the slope of the linear fit is also provided (see text). (e−h): Influence of TSI, SAOD and ENSO on the GMST anomaly. (i,j) Contribution of AMOC to the GMST anomaly. A linear fit between 1975 and 2014 is provided in a similar manner to the AAWR on panels (c,d). (k,l): Influences of PDO and IOD on the GMST anomaly. (m,n) Observed (black) and modelled (red) ocean heat content (OHC), with blue bars corresponding to the observational uncertainty. Observed OHC shown in this figure is based on the average of five OHC datasets as described in Sect. 2.2.5.6. The χ^2_{OCEAN} goodness-of-fit parameter, as well as the ocean heat uptake efficiency (κ) are displayed at the top.

For the AR6 Framework, an AAWR of 0.202 ± 0.006 ºC/decade is obtained from the best fit to the HadCRUT5 GMST record. A considerably smaller value for AAWR of 0.167 ± 0.006 ºC/decade is found for the Baseline framework. As noted above, the rise in total anthropogenic ERF since about 1950 is more pronounced within the AR6 Framework compared to the Baseline (Fig. 2.1i), due to differences in the best-estimate time series of ERF_{AER} between the two frameworks (Fig. 2.1g). Since AAWR is based on the slope of the linear fit to the anthropogenic contribution to warming, a higher value of AAWR is found for the AR6 framework. Here, both uncertainties for AAWR are based on the goodness of the linear fit for a single model run and are noted only for completeness. A more realistic estimate of the true uncertainty in AAWR is found using the ensemble runs of our EM-GC, as described in Section 3.1.

The value of 0.202 ºC/decade found within the AR6 Framework for AAWR is consistent with the assessment of 0.19 ºC/decade between 1980−2020 described in Table 2.4 of AR6 Chapter 2 (Gulev et al., 2021; Forster et al., 2023). Furthermore, AAWR computed within the AR6 framework shows closer agreement − compared to the Baseline framework − with AAWR derived from a CMIP6 multi-model ensemble, the median of which McBride et al. (2021) found to be 0.221 ºC/decade, with the 5th, 25th, 75th and 95th percentiles being 0.151, 0.192, 0.245 and 0.299 ºC/decade, respectively. However, the median value of AAWR for the CMIP6 ensemble, as well

as AAWR obtained from numerous CMIP6 ensemble members, are higher than our regression-based estimate of AAWR using EM−GC. This finding is consistent with several recent assessments finding that some CMIP6 GCMs overestimate the extent of warming in response to GHG emissions (Tokarska et al., 2020b; McBride et al., 2021; Hausfather et al., 2022).

Below, we provide a description of the probabilistic approach utilized by EM−GC to account for the uncertainty in ERF_{AER}. We quantify AAWR and EffCS for the whole range of uncertainty in ERF_{AER} and climate feedback in Section 3.1.

2.2.5 Model Inputs

2.2.5.1 Temperature data

In this study, we use the Hadley Centre Climatic Research Unit version 5 (HadCRUT5) (Morice et al., 2021) GMST anomaly records for the training of the EM−GC. Temperature anomalies are with respect to an 1850−1900 pre-industrial baseline. Similarly to previous works using EM−GC (McBride et al., 2021), the uncertainty time series given with the HadCRUT4 temperature record are used for the EM−GC simulations in this paper. The input GMST anomaly is shown by the black line in Fig. 2.2a-b.

2.2.5.2 Shared Socioeconomic Pathways

In this work, we provide EM−GC output for four different SSP scenarios, two from Tier 1 (SSP1−2.6, SSP2−4.5) and two from Tier 2 (SSP1−1.9, SSP4−3.4) of the ScenarioMIP experiment (O'Neill et al., 2016). Three of these SSP scenarios (SSP1−1.9, SSP1−2.6 and SSP2−4.5) are highlighted as significant scenarios both in Annex III of AR6 (IPCC, 2021a) and Table 1 of Meinshausen *et al.* (2024). SSP4−3.4 is considered as a scenario which was closest to a 50% probability of limiting warming below the PA upper limit of 2.0 ºC in 2100, based on the previous work of McBride *et al.* (2021) using the EM−GC model. Higher forcing scenarios like SSP3−7.0

and SSP5−8.5 are not considered here, as our intention is to focus on the SSP scenarios that are consistent with current or potential future climate policies. Scenarios like SSP3−7.0 and SSP5−8.5 fall into the "The World We Avoided" category of Meinshausen *et al.* (2024), who considers this category to be of a lower priority (see Table 1 of Meinshausen *et al.* (2024)).

2.2.5.3 Baseline Framework

The Baseline framework is constructed based on datasets available shortly before the AR6 report was published. Historical concentrations of GHGs between 1850 and 2014 are from Meinshausen et al. (2017), while GHG concentrations between 2015 and 2100 – with the exception of ODSs – are from the SSP database (Riahi et al., 2017; van Vuuren et al., 2017; Fricko et al., 2017; Fujimori et al., 2017; Calvin et al., 2017; Kriegler et al., 2017; Rogelj et al., 2018) available at https://tntcat.iiasa.ac.at/SspDb/ (last opened: January 8, 2024). Data in these sources are provided on a yearly and decadal grid, respectively, which are interpolated to obtain a monthly time series of GHG concentrations between 1850 and 2100. Concentrations of CO_2, CH_4 and N_2O are converted to SARF using the formulae of Myhre et al. (1998). SARF attributable to stratospheric water vapor is computed as 15% of $SARF_{CH4}$ based on Myhre et al., (2007). Concentrations of ODSs beyond 2015 are from table 6-4 of the 2018 Ozone Assessment Report (Carpenter et al., 2018), and are converted to RF using radiative efficiencies for these obtained from the WMO (2018). The SSP database does not provide SARF time series for tropospheric O_3, hence our input of $SARF_{O3}$ is developed based on Meinshausen et al. (2011c) with the same methodology used by McBride et al. (2021): $SARF_{O3}$ between 1850 and 2005 are obtained from Meinshausen et al. (2011c) through the Potsdam Institute of Climate Research (PICR) website (https://www.pik-potsdam.de/~mmalte/rcps/, last opened: May 21, 2024), while from 2006 onwards, for each SSP scenario, we use $SARF_{O3}$ from a corresponding RCP pathway in

Meinshausen et al. (2011c). $SARF_{O3}$ from RCP2.6 and RCP4.5 are used for SSP1−2.6 and SSP2−4.5, respectively. We use $SARF_{O3}$ from RCP2.6 for SSP1−1.9, while for SSP4−3.4, a new time series was created, using the linear combination of the RCP2.6 and RCP8.5 time series, weighed by the total GHG SARF in 2100. We note that RCP2.6 is sometimes referred to as RCP3−PD (Meinshausen et al., 2011c), including on the PICR website. Consistent with the pre−AR6 formulations, within the Baseline framework, we consider ERF to be equal to SARF for all GHGs (Myhre et al., 2013b; Forster et al., 2021a). Finally, ERF due to land-use change between 1850 and 2011 is obtained from Table AII.1.2 of Annex II of the AR5 (IPCC, 2013a), which is interpolated onto a monthly time grid. Between 2012 and 2100, we used the 2011 value for ERF_{LUC}.

The initial time series for the RF due to tropospheric aerosols is developed in a manner that is similar to that described by McBride et al. (2021). Between 1850 and 2005, we sum RF from six different aerosol types (sulfate, mineral dust, ammonium-nitrate, fossil fuel black carbon and biomass burning organic and black carbon) to obtain a time series of the total aerosol direct effect. RF data for each of these aerosol types are from the PICR (Meinshausen et al., 2011c) for RCP4.5, except for sulfate, where we use the estimate of Smith *et al.* (2011). The PICR datasets for aerosol direct effects are nearly identical until 2005, so the specific choice of RCP4.5 between 1850 and 2004 carries no significance. Time series for aerosol indirect effects between 1850 and 2005 are developed by scaling the time series of the direct effect using methodology described in Section 3.2.2 of Canty *et al.* (2013), as well as Hope *et al.* (2017). The time series for direct and indirect effects are added to obtain the time series of total RF due to tropospheric aerosols between 1850 and 2005. From 2005 onwards, values of total aerosol RF published in the SSP database are used. In order to obtain a continuous time series, values of total aerosol RF between 1850 and 2005 are

scaled such that the value in 2005 matches the total aerosol RF value in 2005 obtained from the SSP database. The time series of RF due to aerosols described above are treated as ERF for the Baseline Framework. The initial ERF_{AER} time series is then scaled to obtain an ensemble of aerosol forcing scenarios, as described in Sect. 2.4.1.

2.2.5.4 AR6 Framework

EM−GC input data for the AR6 Framework are based on the datasets published in Annex III of AR6 (IPCC, 2021a), and the corresponding data repository (https://doi.org/10.5281/zenodo.5705391, last opening: 9th January, 2024) (Smith et al., 2021b). Yearly concentrations for CO_2, CH_4 and N_2O are obtained from this repository, which are based on the time series by Meinshausen *et al.* (2017) and Meinshausen et al. (2020) for the 1850−2014 and 2019−2100 periods, respectively, with a linear transition between the two datasets between 2015 and 2020, as described by Sections 7.SM1.3 and 7.SM.1.4 of AR6 (Smith et al., 2021a). Similarly to AR6, the atmospheric concentrations are converted to SARF with the formulae of Meinshausen et al. (2020), using pre-industrial concentrations of 278.3 ppm, 270.1 ppb and 729 ppb for CO_2, N_2O and CH_4 respectively. These values are ice-core based best assessments of pre-industrial concentrations for these GHGs as described in Chapter 2 of AR6 (Gulev et al., 2021). Tropospheric adjustments of +5%, +7% and −14% are used (Smith et al., 2018b; Hodnebrog et al., 2020) to convert SARF to ERF for CO_2, N_2O and CH_4, respectively, which are based on Section 7.3.2 and 7.SM.1.3.1 of AR6 (Forster et al., 2021a; Smith et al., 2021a). ERF from stratospheric water vapor is computed as 9.19% of methane ERF; our use of this scaling value was found to have the highest agreement with the values provided in Annex III of AR6. ERF time series for halogenated compounds and tropospheric ozone are directly adapted from the AR6 Annex III datasets. This dataset provides total ERF from both stratospheric and tropospheric O_3, which is

dominated by the contribution from tropospheric O_3 (see note below Table AIII.3 in Annex III of AR6). All of the above input time series are interpolated onto a monthly time grid, and then summed to provide the ΔERF_{GHG} time series in Eq. (2.1) for the AR6 Framework.

The ERF time series for land-use change is adapted directly from the AR6 Annex III dataset and interpolated onto a monthly time grid to obtain ΔERF_{LUC} to be used in Eq. (2.1). Finally, the initial ERF time series for tropospheric aerosols is also created using the AR6 Annex III datasets by summing ERF_{ari} (direct effect) and ERF_{aci} (indirect effect) for the entire timeframe for each SSP scenario. The sum is then scaled to create an ensemble for ERF_{AER}, as described in Section 2.4.1. The resulting time series are then interpolated to obtain monthly time series for ERF_{AER}.

2.2.5.5 Natural factors

EM−GC simulations consider a variety of natural factors alongside the anthropogenic component of warming, as shown in Eq. (2.1). The input time series for TSI anomalies used in Eq. (2.1) is constructed from CMIP6 model data between 1850 and 2014 (Matthes et al., 2017), while values for 2015−2019 are obtained from the Solar Radiation and Climate Experiment (SORCE) (Dudok De Wit et al., 2017). The SAOD input time series from 1850 to 1978 is based on extinction coefficients at 550 nm from 80 ºS to 80 ºN obtained from the Volcanic Forcing Dataset (Arfeuille et al., 2014) that was prepared for CMIP6 GCM runs. For 1979 to 2018, we use a time series of SAOD at 550 nm from the Global Space-based Stratospheric Aerosol Climatology (GloSSAC v2.0) (Thomason et al., 2018). For the earlier time period (1850 to 1978), the extinction coefficients from the Volcanic Forcing Dataset were integrated from the tropopause to 39.5 km, to obtain a globally averaged SAOD, weighted by the cosine of latitude from 80 ºS to 80 ºN. For the latter time period (1979 to 2018), we calculate globally averaged SAOD from the GloSSAC dataset using cosine-latitude weighting over the same range of latitudes. For the year 2019, level

3 gridded SAOD product from the Cloud-Aerosol Lidar and Infrared Pathfinder Satellite Observations (CALIPSO) (Vaughan et al., 2004) is used to obtain a global average SAOD, which is then offset by the average difference between the GloSSAC and CALIPSO datasets for the period of overlap (2006−2018) between the two datasets, as described in Section 2.2.5 of McBride *et al.* (2021). The contribution of TSI and SAOD to the GMST anomaly for the best-fit runs of the Baseline and AR6 frameworks are shown in Fig. 2.2e-f. Values of TSI beyond 2019, which marks the end of the training period, are set to zero, while for SAOD, we use the value from December 2019 for the 2020 to 2100 period.

The ENSO time series used during the training period (1850−2019) is based on Version 2 of the Multivariate ENSO Index (MEI.v2) (Wolter and Timlin, 1993; Zhang et al., 2019a). The MEI.v2 dataset provides data starting in 1979. For 1850 to 1978, a historical extension based on Wolter and Timlin (2011) and the HadSST3 dataset (Kennedy et al., 2011) is used, as detailed in Section 2.2.6 of McBride *et al.* (2021). Input values for ENSO are also set to zero beyond 2019. The contribution of ENSO to the GMST anomaly for the best-fit runs are shown in Fig. 2.2g-h.

PDO input data are obtained from the University of Washington PDO index for 1900−2018, with values of zero used outside this time period. IOD input for 1850−2019 was created from the 1º x 1º Sea Surface Temperatures (SSTs) from the Centennial in situ Observation-Based Estimate (COBE) (Ishii et al., 2005), with values of zero assigned beyond 2019. PDO and IOD were found to have little effect on GMST in EM−GC simulations (McBride et al., 2021), but for completeness, we include these factors. The input AMOC time series is based on SST data from HadSST4 (Kennedy et al., 2019) between the Equator and 60 ºN in the Atlantic Ocean, detrended using the magnitude of anthropogenic radiative forcing, then Fourier-filtered to remove frequencies above 1/9 yr^{-1} following Sect. 3.2.3 and 4.1.2 of Canty *et al.* (2013) and Sect. 2.2.7 of

McBride *et al.* (2021). Further detail regarding model inputs for ENSO, AMOC, IOD, PDO and SAOD is given in Sections 2.2.5−2.2.7 of McBride et al. (2021). The computed contribution of variations in the strength of AMOC to the GMST anomaly for the best-fit runs is shown in Fig. 2.2i-j.

2.2.5.6 Ocean Heat Content

For both Frameworks in this paper, the average of five ocean heat content datasets (Levitus et al., 2012; Balmaseda et al., 2013; Cheng et al., 2017; Ishii et al., 2017; Carton et al., 2018) is used. The uncertainty for the average OHC record in each month is obtained by computing the 1σ standard deviation between the five datasets for a given month, or by using the uncertainty from Cheng *et al.* (2017) for that month, whichever is greater. The uncertainties from Cheng *et al.* (2017) were chosen for this purpose as these are the largest uncertainties of the five datasets. EM−GC simulations normalize modelled OHC (Fig. 2.2m-n, red line) to 0 in 1850, which is shown along the average observed OHC time series (black line) and the uncertainty series described above (blue markers) on Fig. 2.2m-n for the upper 700m of the ocean. EM−GC simulations assume that the upper 700m of the ocean holds 70% of the total OHC (McBride et al., 2021). Section 2.2.8 and Fig. S9 of McBride *et al.* (2021) provide additional detail on the average OHC dataset and the corresponding uncertainty time series.

2.2.6 Attributable Anthropogenic Warming Rate and Effective Climate Sensitivity

We define Attributable Anthropogenic Warming Rate (AAWR) as the rate of change in GMST due to anthropogenic activity between 1975 and 2014. The period 1975−2014, chosen in accordance with previous work using our model, spans a 40-year period in which GMST rose in a near-linear fashion due to human activity (McBride et al., 2021). AAWR is determined as the slope of a linear fit to the anthropogenic component ($\Delta T_{MDL,anth}$) of global warming, defined below in

Eq. (2.5), between 1975 and 2014. The time series of $\Delta T_{MDL,anth}$ for the best fts of the Baseline and AR6 Framework simulations are shown by the orange lines in Fig. 2.2c-d.

$$\Delta T_{MDL,anth,i} = \frac{1+\gamma}{\lambda_p}\left(\Delta RF_{GHG,i} + \Delta RF_{AER,i} + \Delta RF_{LUC,i} - Q_{OCEAN,i}\right) \quad (2.5)$$

Equilibrium Climate Sensitivity (ECS) is defined as the warming after climate equilibrated to a theoretical doubling of the pre-industrial concentration CO_2 (IPCC, 2001, 2021c; Forster et al., 2021a). Since equilibrium can take centuries to reach due to the slow heat transfer to deep oceans (Hansen et al., 2011; Church et al., 2013; Tokarska et al., 2020a), often the more short-term Effective Climate Sensitivity (EffCS) (Gregory et al., 2020; Tokarska et al., 2020a; Spencer and Christy, 2023) is used. EM−GC output is used to provide an estimate of EffCS which is based upon the regression to the historical GMST record. We infer EffCS from the ERF due to the doubling of the pre-industrial CO_2 concentration (ΔERF_{2xCO2}) as shown in Eq. (2.6), which is consistent with the methodology described in Box 7.1 of AR6 (Forster et al., 2021a).

$$EffCS = \frac{1}{\lambda_p - \lambda_\Sigma} \times \Delta \mathrm{ERF}_{2\times CO2} \quad (2.6)$$

This method of computing EffCS depends on the formulation of ERF. Within the Baseline Framework, we use the RF formula of Myhre et al. (1998), which leads to $\Delta \mathrm{ERF}_{2\times CO2} = 5.35 \times \ln(2) = 3.71\ Wm^{-2}$. For the AR6 Framework, we use a ΔERF_{2xCO2} value of 3.93 Wm^{-2} based on Section 7.3.2.1 and 7.SM.1.2 of AR6 (Forster et al., 2021a; Smith et al., 2021a). Thus, EffCS computed using the AR6 ERF_{CO2} formula is 6% larger relative to EffCS calculated with the Myhre et al. (1998) formula for a given value of λ_Σ. Finally, we note that climate sensitivity deduced from historical warming may be different from true ECS, as the historical climate feedback could differ from the climate feedback under an abrupt $4\times CO_2$ forcing scenario that is often used to evaluate ECS in ESMs (Andrews et al., 2018; Andrews et al., 2019; Winton et al., 2020; Forster et al., 2021a).

2.2.7 Observational Constraining and Ensemble Weighting

The 160,000 member λ_Σ−ERF_{AER} grid described in Sect. 2.2.4.1 is constrained by observational data of the GMST anomaly and OHC, using three χ^2 based metrics (McBride et al., 2021) given by Eqns. 2A.2−2A.4. Two of these χ^2 metrics quantify how well the modelled GMST anomaly represents the observed temperature anomaly of the atmosphere for the entire training period (1850 – 2019, χ^2_{ATM}) and the GMST anomaly of the last 80 years (1940 – 2019, χ^2_{RECENT}). The third χ^2 metric (χ^2_{OCEAN}) is a goodness-of-fit value between the observed and modeled ocean heat content. Numerical values of χ^2_{ATM} and χ^2_{OCEAN} for the best fit run of the Baseline and AR6 Frameworks are given in Fig. 2.2a-b and 2.2m-n, respectively. The χ^2_{RECENT} metric is used because without this constraint, some solutions with values of χ^2_{ATM} less than or equal to 2 have a visually poor simulation of the rise in GMST over the past 4 to 5 decades (McBride et al., 2021). Only members of the λ_Σ – $ERF_{AER,t}$ grid that yield a good fit to the historical GMST and OHC data are accepted; that is, grid members for which all three χ^2 metrics yield values less than or equal to 2.

For the results shown in Section 2.3, the accepted grid members that are considered to be good fits to the observational data are then weighted by the assessed likelihood that their specific value of ERF_{AER} in the reference year 2011 (for the Baseline Framework) or 2019 (for the AR6 Framework) is "true". To derive these weightings, we use an asymmetrical Gaussian function that is centered around the IPCC best estimate of the ERF of aerosols in the reference year (−0.9 Wm^{-2} in 2011 within the Baseline Framework, and −1.1 Wm^{-2} in 2019 for the AR6 Framework). These weighting functions are shown in Fig. 2.3a-b. The 2σ boundaries of the Gaussians are based on the boundaries of the likely range of ERF_{AER} in the same year provided by the corresponding IPCC reports (see Table 2A.3). The Gaussians are asymmetrical, as the likely range of ERF_{AER} specified in both the AR5 and AR6 reports is not symmetrical around the respective best estimate. The

weighted grid is then used to provide probabilistic estimates of AAWR and EffCS (Sect. 2.3.1), as well as probabilistic forecasts on the GMST anomaly (Sect. 2.3.2), which serve as the primary output of EM−GC.

2.3 Results

2.3.1 Ensemble-based Assessment of AAWR and Climate Sensitivity

In Sect. 2.2.4, we briefly analyzed the AAWR obtained from EM−GC best fits to the GMST record, assuming the AR5 and AR6 prescribed radiative forcing for aerosols, for the Baseline and AR6 Frameworks, respectively. We found a significant increase in the value of AAWR from 0.167 ºC/decade within the Baseline Framework, to 0.202 ºC/decade for the AR6 Framework. In this section, we evaluate AAWR and EffCS for the entire 160,000 member EM−GC grid, which accounts for the uncertainty in the magnitude of climate feedback and ERF of aerosols (Sect. 2.2.4.1).

Figure 2.3 shows AAWR (Fig. 2.3c−d) and EffCS (Fig. 2.3e−f) for the EM−GC λ_{Σ} – $ERF_{AER,t}$ grid, within the Baseline (left) and AR6 Frameworks (right). Colors denote the values of AAWR and EffCS found for simulations that satisfy all three χ^2 metrics, as described in Sect. 2.2.7. Fig 2.3a−b shows the Gaussians used to convert the λ_{Σ} – $ERF_{AER,t}$ grid output into a probabilistic quantification of AAWR and EffCS, which are presented in the form of Probability Distribution Functions (PDFs) in Fig. 2.4. The height of bars on Fig. 2.4 corresponds to the probability of AAWR (Fig. 2.4a) and EffCS (Fig. 2.4b) − obtained from the Gaussian-weighting of the EM−GC grid − being in the range defined by the width of each column. We use a bin size of 0.005 ºC decade^{-1} and 0.1 ºC in Fig. 2.4 for AAWR and EffCS, respectively. Figure 2.4 also shows the EM−GC median for AAWR and EffCS, which we define as the values of AAWR and EffCS corresponding to 50% probability, alongside the 5th to 95th percentile range for AAWR and EffCS.

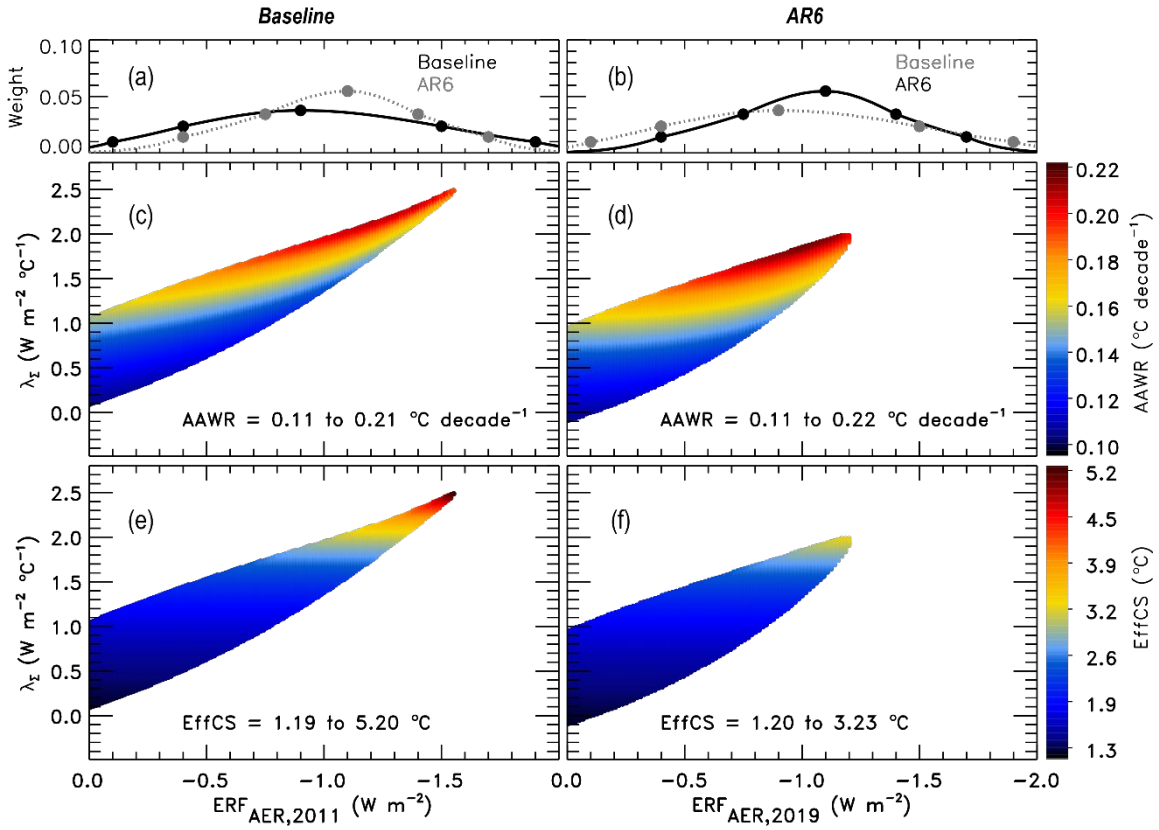

Figure 2.3: Aerosol weighting method and EM−GC computed values of AAWR and EffCS for combinations of ERF_{AER} and λ_{Σ}. (Left): Simulations using the Baseline Framework. (Right): Simulations using the AR6 Framework. (a−b) Asymmetrical Gaussians used to weight aerosol scenarios for probabilistic forecasts, as described in Sect. 2.2.7. Points marked on the Gaussians represent specific ERF values used as the central values, as well as 1σ and 2σ boundaries of each Gaussian (Table 2A.3). The Gaussians are overlaid for visual comparison. The Gaussians shown with the solid black line are used to weight the EM−GC output in each column. (c−d) EM−GC computed values of AAWR for the $\lambda_{\Sigma} - ERF_{AER,t}$ grid. Colors denote the specific values of AAWR as indicated by the color bar on the right, and are only shown for the combinations of ERF_{AER} and λ_{Σ} for which a good fit to the HadCRUT5 historical climate record was found. (e-f) EM−GC computed values of EffCS for the $\lambda_{\Sigma} - ERF_{AER,t}$ grid.

Within the Baseline Framework (Fig. 2.3c), the historical GMST record can be fit with combinations of high λ_{Σ} and strong aerosol cooling. For example, good fits to the historical GMST record were found with aerosol cooling as negative as −1.6 Wm^{-2} in 2011, which corresponds to much stronger aerosol cooling than the AR5 best estimate of −0.9 Wm^{-2} within the same year. Conversely, within the AR6 Framework, the strongest aerosol cooling for which a good fit was found (about −1.2 Wm^{-2} in 2019) is very close to the AR6 best estimate of −1.1 Wm^{-2} in 2019.

Thus, within the AR6 Framework, it is not possible to fit the historical GMST record with aerosol cooling much stronger than the corresponding IPCC best-estimate. Within the AR6 Framework, the $ERF_{AER,2019}$ range for which a good fit to the historical GMST record was found is 0.0 to −1.2 Wm^{-2}, which is broadly consistent with the AR6 likely range for $ERF_{AER,2019}$ of −0.4 to −1.7 Wm^{-2} (Forster et al., 2021a). While good fits to the historical GMST record were found with weak aerosol cooling of 0 to −0.4 Wm^{-2}, these simulations are given very low weights (Fig. 2.3b) because the value of ERF_{AER} lies outside of the AR6−assessed likely range. These weak aerosol cooling simulations are also associated with values of climate feedback (λ_Σ) that fall outside the "likely" range of total feedback derived from Table 7.10 of AR6 (see Appendix A for details). Finally, even though EM−GC simulations can obtain good fits to the HadCRUT5 record with ERF_{AER} being greater than 0 Wm^{-2} and with λ_Σ being negative, these simulations are discarded (and not shown in Fig. 2.3) because Section 7.3.3.4 of AR6 states that it is "virtually certain" that total aerosol ERF is negative. The ERF_{AER} cutoff in Fig. 2.3c−f is thus set at 0 Wm^{-2}.

The range of AAWR found using the entire EM−GC grid is near identical between the Baseline and AR6 Frameworks at 0.11 to 0.21 ºC $decade^{-1}$ and 0.11 to 0.22 ºC $decade^{-1}$, respectively (Fig. 2.3c−d). However, the median AAWR increases from 0.16 to 0.18 ºC $decade^{-1}$ from the Baseline to the AR6 Framework (Fig. 2.4a). Similarly to the range of AAWR derived from the entire λ_Σ – $ERF_{AER,t}$ grid, the 5th to 95th percentile ranges are found to be consistent between the Baseline and AR6 Frameworks, at 0.12 to 0.20 ºC $decade^{-1}$ and 0.13 to 0.21 ºC $decade^{-1}$, respectively. As described above, AAWR found for the best fit to the GMST record using the IPCC prescribed best estimate for the RF of aerosols is 0.167 ºC $decade^{-1}$ and 0.202 ºC $decade^{-1}$ for the Baseline and AR6 Frameworks, respectively (Fig. 2.2c−d). For the Baseline Framework, the best−fit AAWR of 0.167 ºC $decade^{-1}$ found using the IPCC best estimate aerosol

cooling is close to the EM−GC median of 0.16 ºC decade^{-1}. Conversely, for the AR6 Framework, the median AAWR of 0.18 ºC decade^{-1} is about 10% smaller than the AAWR of 0.202 ºC decade^{-1} shown in Fig. 2.2d. This difference is caused by the fact that the IPCC AR6 best estimate of −1.1 W m^{-2} for $ERF_{AER,2019}$ is very close to the upper end of the range of ERF_{AER} for which a good fit was found (Fig. 2.3d), whereas for the Baseline Framework, the AR5 best estimate for aerosol cooling of −0.9 W m^{-2} is approximately in the middle of the range of ERF_{AER} for which good fits to the historical GMST record are found.

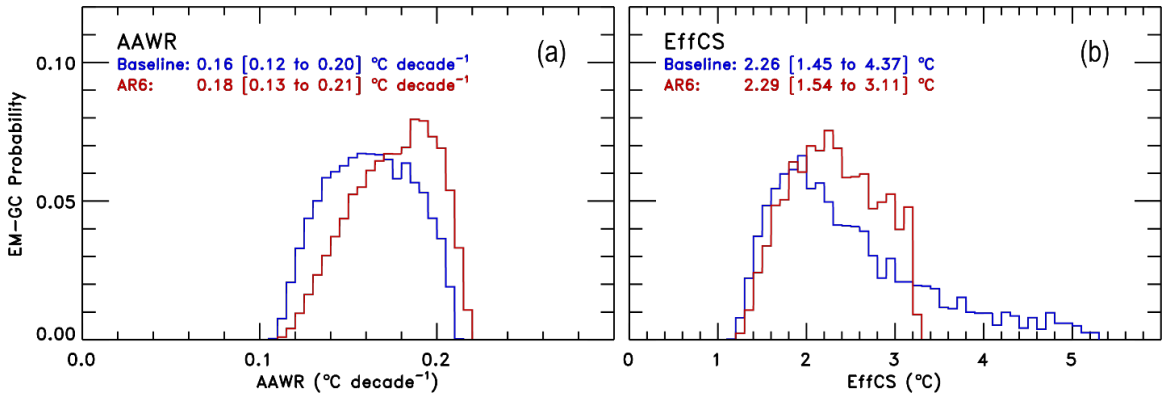

Figure 2.4: (a) Probability Distribution Functions (PDFs) for AAWR obtained from EM−GC simulations trained with the HadCRUT5 temperature dataset. AAWR from the Baseline Framework is shown in blue, while AAWR from the AR6 Framework is shown in red. The EM−GC median (defined as the 50th percentile probability), and 5th to 95th percentile range is displayed at the top. (b) PDFs of EffCS within the Baseline (blue) and AR6 Framework (red), with the corresponding median and range.

The EM−GC computed median and 5−95% range of AAWR are 0.18 [0.13 to 0.21 ºC decade^{-1}] between 1974 and 2014 for the AR6 Framework. This range and median are consistent with several other studies, such as Samset et al. (2023), who found a rate of increase in warming to be 0.19 ± 0.01 ºC decade^{-1} between 1973 and 2022 for the HadCRUT5 GMST record. Samset et al. (2023) also found rates for other temperature records such as GISTEMP v4, NOAA v5.1 and Berkeley Earth to be 0.19, 0.18 and 0.17 ºC decade^{-1}, respectively. Our HadCRUT5−based median of 0.18 ºC decade^{-1} is consistent with the analysis of Samset et al. (2023) who employed a variety of historical temperature records, as well as the assessment of 0.19 ºC decade^{-1} between

1980−2020 described in Table 2.4 of AR6 Chapter 2 (Gulev et al., 2021; Forster et al., 2023). As highlighted by Samset et al. (2023) however, warming has accelerated since 1990 at a rate of 0.008 to 0.025 ºC decade^{-1} per decade depending on the temperature record studied, with Forster et al. (2023) finding a rate of 0.2 ºC decade^{-1} for human−induced warming for the 2013−2022 period, while Ribes et al. (2021) found this rate to be 0.23 ºC decade^{-1} for the 2010−19 period.

Our median and range of AAWR of 0.18 [0.13 to 0.21 ºC decade^{-1}] within the AR6 Framework is considerably lower than the median and 5−95% range of 0.221 [0.151 to 0.299 ºC decade^{-1}] derived from a CMIP6 multi-model ensemble by McBride *et al.* (2021). The CMIP6 median obtained by McBride *et al.* (2021) is greater than the upper limit of the range found in our study. Samset *et al.* (2023) also found that "virtually all CMIP6 simulations have higher 50−year warming rates than the observations", using an ensemble of 119 ESM simulations from CMIP6. In particular, Samset et al. (2023) found that models with ECS being greater than 3.0 ºC tend to quantify the rate of warming to be above 0.2 ºC decade^{-1} up to about 0.43 ºC decade^{-1} for certain models with ECS around 5 ºC (Fig. 2.2d of Samset et al. (2023)). Armour *et al.* (2024) showed that CMIP5/6 models that tended to over-estimate the observed warming trend over the 1981 to 2014 time period tended to have larger values of EffCS, which they attribute to gross differences in the observed versus modeled warming patterns, particularly in the tropical Pacific Ocean. Overall, AAWR found using our AR6 Framework is consistent with other lines of empirical evidence in the recent literature, and tends to be quite a bit lower than the CMIP6 multi-model mean.

EffCS found using the three χ^2 based metrics has a range of 1.20 to 3.23 ºC in the AR6 Framework relative to a range of 1.19 to 5.20 ºC for the Baseline Framework (Fig. 2.3e−f). The lower limit is found to be near identical between the two Frameworks; however, the upper limit of

EffCS is substantially smaller within the AR6 Framework. This difference originates from the fact that the HadCRUT5 GMST record can be fit with combinations of high climate feedback and strong aerosol cooling only for the Baseline Framework, as described above. Fits with very strong aerosol cooling correspond to high λ_Σ and yield high values of EffCS (Eq. (2.6)) in the Baseline framework, resulting in a high upper bound for the range of EffCS.

The median EffCS is also found to be near identical between the Baseline and AR6 Frameworks at 2.26 and 2.29 ºC, respectively, with corresponding 5−95% ranges being [1.45 to 4.37 ºC] and [1.54 to 3.11 ºC] (Fig. 2.4b). The 95th percentile value of EffCS is considerably smaller within the AR6 Framework relative to the Baseline, due to the aforementioned phenomenon of not being able to obtain good fits to the GMST anomaly in the AR6 Framework for aerosol scenarios with $ERF_{AER,2019}$ being more negative than about −1.2 W m^{-2}. Given that in the AR6 Framework the Gaussian used to weight the λ_Σ – $ERF_{AER,t}$ grid is centered around the IPCC best estimate of −1.1 W m^{-2}, the few combinations of λ_Σ – $ERF_{AER,2019}$ that yield good fits for which $ERF_{AER,2019}$ is between −1.1 and −1.2 W m^{-2} are still assigned high weights. Within the Baseline Framework, good fits with strong aerosol cooling scenarios (as negative as −1.6 W m^{-2} in 2011) are far from the AR5 best estimate of −0.9 W m^{-2} cooling and are therefore assigned small weights (Fig. 2.3a). The high cooling scenarios correspond to the low probability tail of the PDF with EffCS greater than about 3.5 ºC shown in Fig. 2.4b for the Baseline Framework. The range of EffCS found for the AR6 Framework is considerably narrower than for the Baseline, which is well represented by the difference in the 95th percentiles for EffCS for the two frameworks of 3.11 ºC and 4.37 ºC, respectively (Fig. 2.4b).

A recent study by Skeie *et al*. (2024b) found the best estimate and 90% uncertainty range for EffCS to be 2.2 [1.6 to 3.0 ºC] using a Bayesian estimation model and ERF datasets from AR6.

Our estimate of 2.29 [1.54 to 3.11 ºC] within the AR6 Framework exhibits close agreement with this study. Furthermore, Skeie *et al.* (2024b) assume climate feedback to be constant over the historical period, similar to our work. However, climate feedbacks may not be constant over time, partly due to their dependence on the spatial pattern of warming, often termed "pattern effect" (Andrews et al., 2015; Armour, 2017; Stevens et al., 2016; Skeie et al., 2024b). Since climate sensitivity is derived from the magnitude of climate feedback (i.e. (Forster et al., 2021a)), the magnitude of the pattern effect governs how much climate sensitivity inferred from historical records (EffCS) differs from ECS. The sensitivity of GMST projections found using our model to time-dependent feedback is quantified in Section 3.3.6 of McBride *et al.* (2021).

Next, we quantify the effect of time-dependent feedback on ECS. Similar to Skeie *et al.* (2024b), we apply the AR6 formulation for the impact of the pattern effect on the ensemble output of the AR6 Framework. The impact of time-dependent feedback on ECS is quantified as in Eq. (2.7), where α' represents the difference between climate feedback inferred from historical warming and the climate feedback corresponding to that found for an abrupt doubling of the concentration of CO_2.

$$ECS = \frac{1}{\lambda_p - \lambda_\Sigma - \alpha'} \times \Delta \mathrm{ERF}_{2\times CO2} \tag{2.7}$$

The formulation shown in Eq. (2.7) is equivalent with the methodology for the computation of ECS with the inclusion of α' described in Section 7.5.2 of AR6 (Forster et al., 2021a). The coefficient α' is assessed by Section 7.4.4.3 of AR6 to have a value of 0.5±0.5 W m^{-2} K^{-1}, at a low confidence level. Figure 2.5 shows ECS for values of α' within the AR6 assessed range of 0 to 1 W m^{-2} K^{-1}, in increments of 0.1 W m^{-2} K^{-1} (black circles, median), where the error bars represent the 5th and 95th probabilistic range of ECS. The dashed horizontal line and shaded area correspond to the central value and very likely range of ECS from Table 7.13 of AR6 (Forster et al., 2021a).

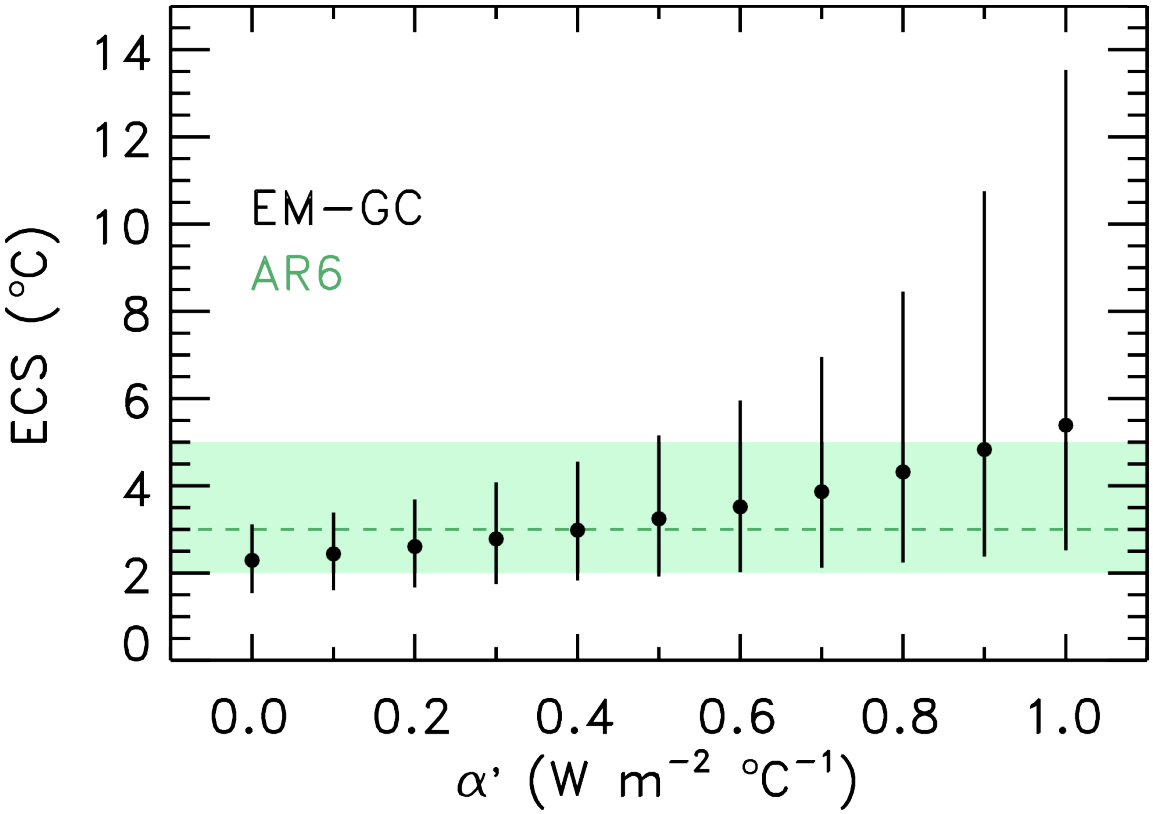

Figure 2.5: Equilibrium Climate Sensitivity (ECS) as the function of the pattern effect (α', see text). Black vertical bars and circles correspond to the EM−GC 5−95% range, and 50% probability, respectively. The green shaded area and horizontal dashed line represent the AR6 very likely range, and central estimate of ECS respectively, from Table 7.13 of Forster et al. (2021a). All results shown in this figure are based on inputs from the AR6 ERF Framework.

For α' = 0 W m^{-2} K^{-1} (corresponding to no pattern effect), EffCS is equal to ECS and we obtain a median and range for ECS of 2.29 [1.54 to 3.11 ºC]. Using the AR6 best estimate of α' = 0.5 W m^{-2} K^{-1}, we find ECS to be 3.24 [1.92 to 5.15 ºC], while the AR6 upper limit of α' = 1.0 W m^{-2} K^{-1} yields a median and 5−95% range of 5.39 [2.52 to 13.54 ºC]. Our estimate of ECS agrees extremely well with the AR6 central estimate and likely range of ECS, for the AR6 best-estimate of α', which equals 0.5 W m^{-2} K^{-1}. This conclusion is consistent with Skeie *et al.* (2024b), who also found their estimate of climate sensitivity to be "almost identical" to the AR6 central value and very likely range of 3.0 [2.0 ºC to 5.0 ºC], upon using the AR6 best estimate of α'. Our range of ECS of [1.92 to 5.15 ºC] at α' = 0.5 W m^{-2} K^{-1} is also consistent with the recent assessment of

Cooper et al. (2024), who found ECS to be between 1.4 ºC to 5.0 ºC based on analysis of data acquired during the Last Glacial Maximum (LGM). Our median estimate of 3.24 ºC for α' = 0.5 W m^{-2} K^{-1} is, however, higher than the LGM−based best estimate of 2.4 ºC. However, when combining the LGM−based assessment with other lines of evidence, Cooper et al. (2024) finds ECS to be 2.9 ºC [2.1 to 4.1 ºC], which agrees well with our estimate.

Additionally, Fig. 2.5 shows that the 5th percentile of ECS varies between about 1.5 to 2.5 ºC, depending on the magnitude of α', consistent with the AR6 assessment of ECS being greater than 1.5 ºC at a virtually certain level of confidence (Forster et al., 2021a). The 50th percentile estimates for ECS also all fall into the range of ECS assessed by AR6. Conversely, our 95th percentile estimates for ECS vary greatly with α', and carry a substantially larger level of uncertainty than the 5th and 50th percentile estimates. These findings are consistent with Chapter 7 of AR6, which stated "warming over the instrumental record provides robust constraints on the lower end of the ECS range (high confidence), but owing to the possibility of future feedback changes it does not, on its own, constrain the upper end of the range, in contrast to what was reported in AR5."

We now discuss how the rate of warming in recent decades relates to EffCS/ECS and the spatial pattern of global warming. Armour *et al.* (2024) found the central estimate and 5−95% range for the rate of warming between 1981 and 2014 to be 0.18 [0.15 to 0.21 ºC $decade^{-1}$], which corresponds to ECS of 2.7 [1.5 to 3.9 ºC] and EffCS of 2.3 [1.9 to 2.7 ºC]. The rate of warming obtained by Armour *et al.* (2024) is in close agreement with our AAWR estimate of 0.18 [0.13 to 0.21 ºC $decade^{-1}$] between 1974 and 2014. Furthermore, our EffCS estimate of 2.29 [1.54 to 3.11 ºC] closely matches that of Armour *et al.* (2024), albeit with a wider 5−95% range. Finally, our ECS estimate was found to be 3.24 [1.92 to 5.15 ºC] for α' = 0.5 W m^{-2} K^{-1}, which is broadly

consistent with Armour *et al.* (2024) value. Samset *et al.* (2023) found that CMIP6 models with ECS greater than about 3.0 ºC tend to provide an overly high estimate of the trend of observed warming in recent decades. Armour *et al.* (2024) suggest the overly high estimates of recent warming trends are related to CMIP5/6 historical simulations failing to reproduce observed SST patterns, particularly a cooling of the eastern tropical Pacific and a warming of the western Pacific. Weaver *et al.* (2024) reached the same conclusion based on analysis of top of the atmosphere albedo of clouds and aerosols from 340 nm radiances observed by NASA and NOAA satellite instruments. Armour et al. (2024) found that CMIP5/6 models with high ECS can nonetheless provide estimates of warming trends consistent with observations, after correcting for the biases in SST trend patterns. Weaver *et al.* (2024) showed that a significant number of CMIP6 models are unable to simulate the observed latitudinal pattern of cloud albedo trends over the Pacific Ocean, again tied to the observed cooling trend in the eastern tropical Pacific.

Our multiple linear regression – energy balance RCM, despite not considering the spatial pattern of warming, is able to reproduce estimates of EffCS and ECS consistent with the Armour *et al.* (2024) study, who explicitly consider the spatial pattern of global warming. We find that the range of observed warming in recent decades is consistent with the AR6 estimate of ECS and that the CMIP5/6 models that estimate a more rapid rate of warming may indeed fall into the "hot model" category (Tokarska et al., 2020b; McBride et al., 2021; Hausfather et al., 2022), potentially due to an overestimation of historical EffCS (Armour et al., 2024).

2.3.2 Probabilistic Forecast on Future Warming

Here we quantify the magnitude of future warming based on projections of ERF for four SSP scenarios. Here, we show projections of GMST for only constant feedback because the GMST anomaly can be fit quite well for a wide-range of time invariant feedback, albeit spanning a large

range of values, particularly for the Baseline Framework (Fig. 2.3c-d). We compare forecasts of GMST using the AR6 Framework with forecasts found using the Baseline Framework for the same SSPs, where "Baseline" refers to the state-of-knowledge prior to the release of AR6. Similarly to our analysis of AAWR and EffCS in Section 2.3.1, forecasts of the GMST anomaly for the λ_{Σ}–$ERF_{AER,t}$ grid, weighted by an asymmetrical Gaussian function (Fig. 2.3a-b) that describes the AR5-based (Baseline) or AR6-based assessments of the likelihood of how much global warming by GHGs has been offset by tropospheric aerosols, is central to these probabilistic forecasts.

Figure 2.6 shows computed values of the GMST anomaly in the year 2100 (ΔT_{2100}) for the AR6 Framework, for four SSPs. The colors correspond to values of ΔT_{2100} for model runs that provide a good fit to the observed GMST anomaly over the 1850–2019 training period, as defined by all three χ^2 metrics described in Section 2.2.7 yielding values less than or equal to 2.

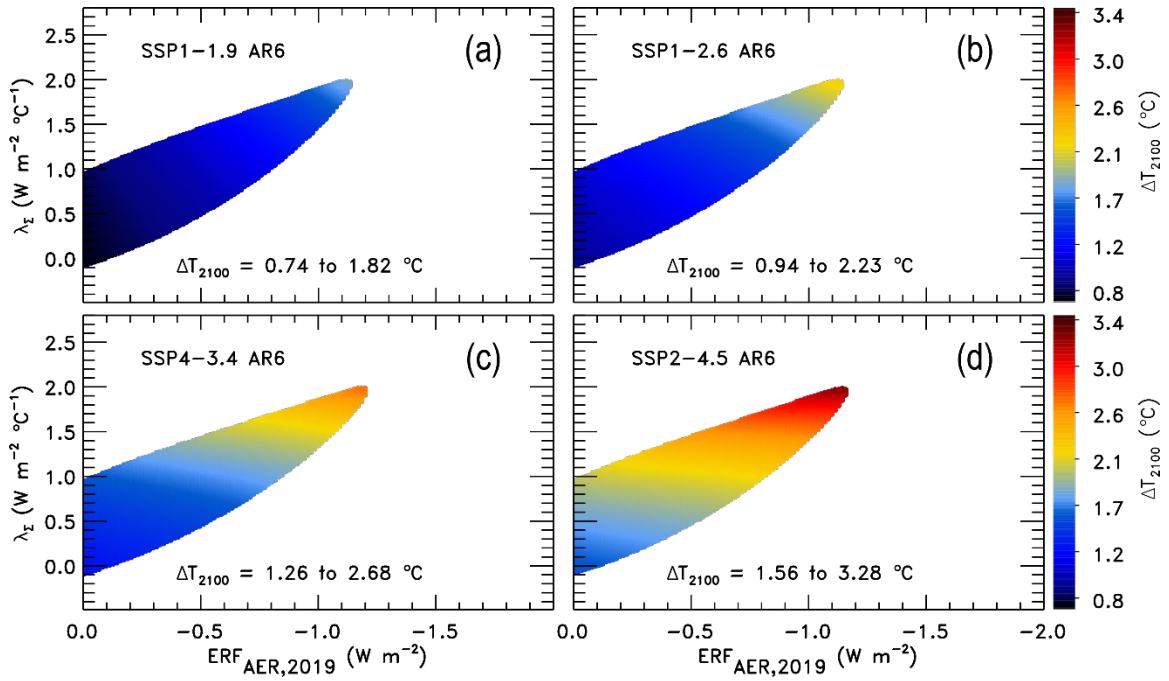

Figure 2.6: GMST anomaly at the end of the century (ΔT_{2100}) relative to a pre–industrial baseline for combinations of λ_{Σ} and $ERF_{AER,2019}$. Colors denote values of ΔT_{2100} as indicated by the color bars on the right. Plots generated from EM-GC simulations trained on the HadCRUT5 GMST record, and use the AR6 ERF Framework. Only those combinations are colored where a good fit on the HadCRUT5 GMST record was found. (a) ΔT_{2100} for SSP1–1.9. (b) ΔT_{2100} for SSP1–2.6. (c) ΔT_{2100} for SSP4–3.4. (d) ΔT_{2100} for

SSP2−4.5. Values of ΔT_{2100} for the $\lambda_\Sigma - ERF_{AER}$ grid within the Baseline Framework are shown in Fig. 2A.2.

Table 2.1 details numerical values for ΔT_{2100} projections for the four SSPs. As described in Sect. 2.3.1, within the Baseline Framework the historical GMST record can be fit with combinations of high λ_Σ and strong aerosol cooling. This difference results in a small shift in the upper boundary of ΔT_{2100}, with values associated with the Baseline Framework being larger than those for the AR6 Framework. Even though the climate record can be fit with much higher values of λ_Σ within the Baseline Framework, ERF projections within the AR6 Framework are much higher than in the Baseline Framework (Fig. 2.1i), which offsets some of the λ_Σ – driven difference. For SSP2−4.5, the upper estimate of ΔT_{2100} being 3.47 ºC corresponds to a value of λ_Σ of about 2.5 W m^{-2} $ºC^{-1}$ (Fig. 2A.2) within the Baseline Framework. The upper boundary of ΔT_{2100} = 3.28 ºC is found at a smaller climate feedback of about λ_Σ = 2.0 W m^{-2} $ºC^{-1}$ for the AR6 Framework.

Table 2.1: ΔT_{2100} for the four SSP scenarios studied. The first four rows correspond to data for the entire $\lambda_\Sigma - ERF_{AER,t}$ grid as shown in Figs. 2.6 and 2A.2. The last four rows are associated with the EM−GC probabilistic assessment, with values derived from PDFs in Fig. 2.8 shown using the format of Median [5−95% range].

	SSP Scenario	**Baseline Framework (ºC)**	**AR6 Framework (ºC)**
Full $\lambda_\Sigma - ERF_{AER,t}$ grid	SSP1−1.9	0.73 to 2.06	0.74 to 1.82
	SSP1−2.6	0.93 to 2.58	0.94 to 2.23
	SSP4−3.4	1.15 to 3.01	1.26 to 2.68
	SSP2−4.5	1.42 to 3.47	1.56 to 3.28
Median [5−95% range]	SSP1−1.9	1.14 [0.81 to 1.87]	1.34 [0.93 to 1.72]
	SSP1−2.6	1.46 [1.05 to 2.28]	1.67 [1.18 to 2.13]
	SSP4−3.4	1.80 [1.31 to 2.77]	2.10 [1.54 to 2.62]
	SSP2−4.5	2.18 [1.62 to 3.14]	2.60 [1.92 to 3.20]

Figure 2.7 shows our probabilistic forecasts of GMST in a time dependent fashion for the AR6 Framework. Time-dependent projections of GMST for the Baseline Framework are in Fig.

2A.3. Similar to AAWR and EffCS discussed above, the probabilistic forecasts of the GMST anomaly are provided by weighting model results that provide good fits to the climate record within the λ_{Σ}−ERF_{AER} grid. The weighting procedure uses the Gaussian functions that describe the assessed likelihood of various values of RF of climate due to aerosols shown on the top panels of Fig. 2.3. The colors on Fig. 2.7 correspond to the probability of the ΔT anomaly being equal to or greater than a given value. The figure also shows the HadCRUT5 GMST observations in black, as well as the likely range of warming for 2016 to 2035 provided by the authors of Chapter 11 of the AR5 report (Kirtman et al., 2013) in recognition of the fact that the CMIP5 models tended to over-estimate observed warming. Gold horizontal lines represent the 1.5 ºC and 2.0 ºC GMST anomalies relative to pre−industrial, while gold circles correspond to the years where the 1.5 ºC and 2 ºC thresholds are crossed with 5, 50 and 95% probability (hereafter termed crossover years). The probabilistic GMST anomaly forecast using SSP1−1.9 in the AR6 Framework lies below the 2 ºC threshold until the end of century throughout the ensemble (Fig. 2.7a), whereas the projection of GMST for SSP2−4.5 exceeds the 1.5 ºC threshold in all cases (Fig. 2.7d).

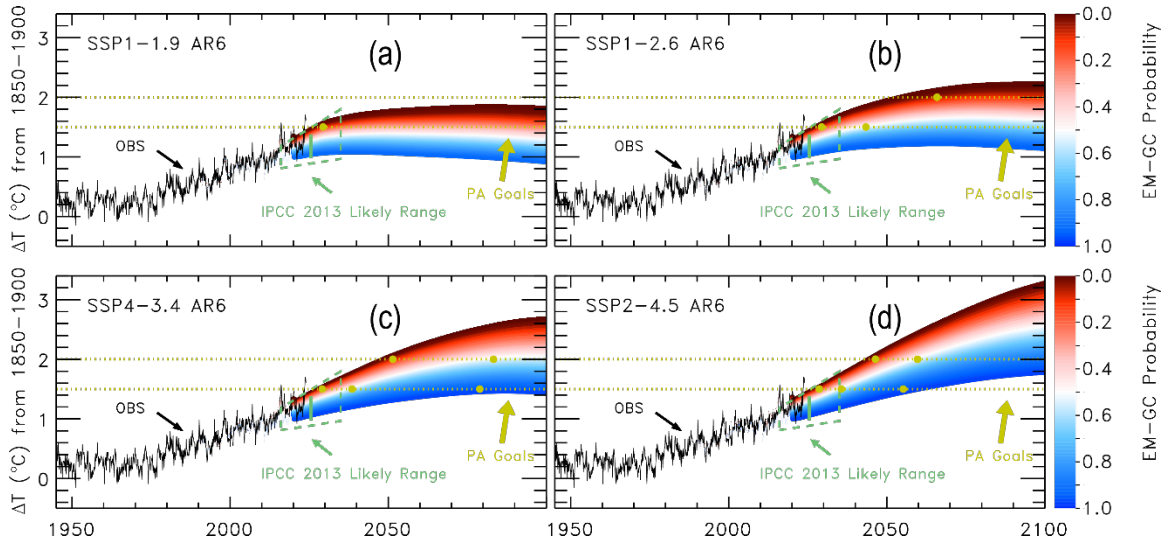

Figure 2.7: Time-dependent probabilistic forecasts of the GMST anomaly beyond 2019 within the AR6 Framework. The black line represents the HadCRUT5 GMST record on which EM−GC was trained for these simulations, relative to an 1850−1900 baseline. Colors represent the probability of reaching a certain

temperature or higher at a given time, as indicated by the color bars on the right. The green trapezoid represents the likely range of warming as shown in Fig. 11.25b of the IPCC AR5 report (Kirtman et al., 2013). The target and upper limit of the Paris Agreement are shown with horizontal lines in gold. Circle markers on these lines correspond to the projected GMST anomaly crossing these thresholds with the probability indicated by the colors. (a) GMST projections for SSP1−1.9. (b) GMST projections for SSP1−2.6. (c) GMST projections for SSP4−3.4. (d) GMST projections for SSP2−4.5. Results for the Baseline Framework are shown in the same fashion in Fig. 2A.3.

Table 2.2 provides the year that temperature anomaly thresholds are crossed for the median as well as the 5th and 95th percentiles of the probabilistic forecasts of ΔT. Figure 2.8 shows the probability distribution functions (PDFs) of ΔT_{2100}. Results for both the Baseline and AR6 Framework are shown in Table 2.2 and Fig. 2.8, although we generally discuss only the results found for the latter. For the 5th percentile of the AR6 Framework, the 1.5 ºC threshold is crossed in either 2028 or 2029 for all four SSP scenarios. For the median member of our probabilistic forecasts, the 1.5 ºC threshold is crossed in the years 2035, 2038, and 2043 for the SSP2−4.5, SSP4−3.4, and SSP1−2.6 scenarios, respectively, whereas the 1.5 ºC threshold is not crossed for the median member of the SSP1−1.9 scenario. For the 95th percentile of the forecasts within the AR6 Framework, the 1.5 ºC warming threshold is crossed in 2055 and 2079 for the SSP2−4.5 and SSP4−3.4 scenarios, respectively, and is not crossed for the other two scenarios. Here, the 5th percentile has more warming than the 95th percentile, due to the fact that Fig. 2.7 shows probabilistic forecasts that ΔT will exceed a given amount.

Median projections of ΔT_{2100} within the AR6 Framework are found to be between 0.2 ºC (SSP1−1.9, SSP1−2.6) and 0.4 ºC (SSP2−4.5) greater than in the case of the Baseline Framework, mainly due to the larger projected anthropogenic ERF for AR6 (Fig. 2.1i). The PDF of ΔT_{2100} for the AR6 Framework is narrower and shifted a bit to the right (higher chance of more warming), compared to the Baseline Framework (Fig. 2.8), primarily due to two factors: the ability to obtain good fits to the GMST anomaly at the highest values of climate feedback only for the Baseline

Framework, and the larger weight given to ensemble members with large, contemporary aerosol cooling in the AR6 Framework (Fig. 2.3).

Our median, 5th and 95th percentile estimates of ΔT_{2100} (Table 2.1) agree well with the long-term warming assessed by AR6, for years 2081−2100. Table 4.5 of AR6, which uses Global Surface Air Temperatures (GSAT) rather than GMST, projects warmings (median and 5−95% range) of 1.4 [1.0 to 1.8 ºC], 1.8 [1.3 to 2.4 ºC], and 2.7 [2.1 to 3.5 ºC] for SSP1−1.9, SSP1−2.6 and SSP2−4.5, respectively. As described in Chapters 1, 2 and 4 of AR6 (Chen et al., 2021; Gulev et al., 2021; Lee et al., 2021), GMST and GSAT differ by up to 10%, but the sign of the difference is highly uncertain. Our projections of end-of-century warming and for crossing the 1.5 ºC and 2.0 ºC GMST thresholds are generally consistent with the GSAT-based assessments of AR6 (Lee et al., 2021).

Finally, our study relies on SSP−based ERF data and does not factor in the significant decline of maritime sulfur emissions (and connected change in ERF_{AER}) caused by updated regulations on the sulfur content of ship fuels, introduced by the International Maritime Organization (IMO) in 2020. Varying estimates exist on the magnitude of ΔERF_{AER} from the new IMO regulations and their impact on GMST/GSAT (Yuan et al., 2024; Skeie et al., 2024a; Quaglia and Visioni, 2024; Yoshioka et al., 2024). The reduction in shipping emissions may have brought forward global warming by 2−3 years (Gettelman et al., 2024; Jordan and Henry, 2024). Such a change would also help explain the unexpectedly high GMST anomalies of the year 2023, which have not otherwise been captured by climate model projections (Schmidt, 2024). The impact of IMO regulations on GMST in our model framework will be quantified in a future study.

Table 2.2: Years of crossing the 1.5 ºC and 2.0 ºC GMST anomaly thresholds for the four SSP scenarios studied. For each entry, we present the 50% probability as our central estimate, as well as the 5−95% range. The label "n.c" is used consistent with Table 4.5 of AR6 (Lee et al., 2021) and corresponds to a given threshold not being crossed in the 2020−2100 period.

	1.5 ºC Crossover		2.0 ºC Crossover	
	Baseline	**AR6**	**Baseline**	**AR6**
SSP1−1.9	n.c [2028 to n.c]	n.c [2029 to n.c]	n.c [n.c to n.c]	n.c [n.c to n.c]
SSP1−2.6	n.c [2029 to n.c]	2043 [2029 to n.c]	n.c [2059 to n.c]	n.c [2065 to n.c]
SSP4−3.4	2048 [2030 to n.c]	2038 [2029 to 2079]	n.c [2050 to n.c]	2083 [2051 to n.c]
SSP2−4.5	2042 [2030 to 2080]	2035 [2028 to 2055]	2082 [2047 to n.c]	2059 [2046 to n.c]

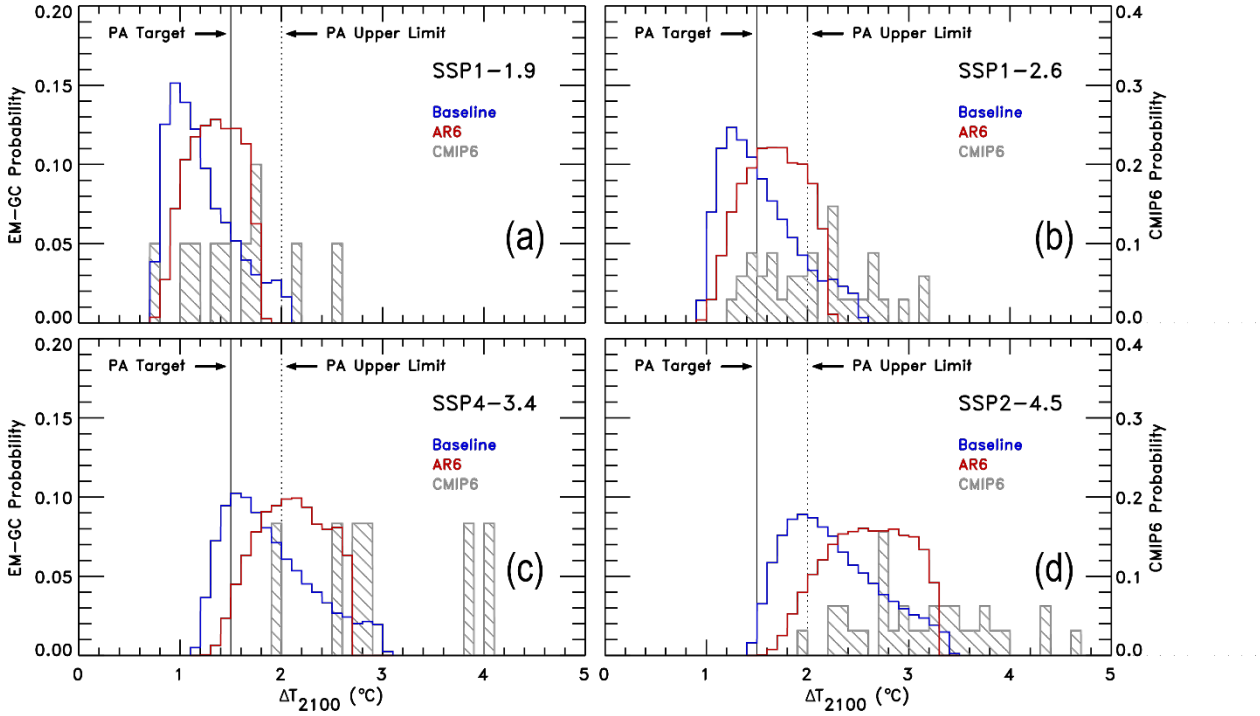

Figure 2.8: Probability Distribution Functions (PDFs) for ΔT_{2100} obtained from EM−GC simulations trained on the HadCRUT5 temperature dataset. Model runs for the Baseline and AR6 Frameworks are shown in blue and red, respectively. Grey color represents the PDFs obtained from a CMIP6 multi−model ensemble as described in Section 3.3.1 of McBride et al. (2021), and are shown for comparison with EM−GC results. The left-hand y axis corresponds to the EM−GC probabilities, and the right-hand y axis is for the CMIP6 probabilities. The PA target and upper limit are shown as solid and dashed vertical lines, respectively. (a) PDFs for SSP1−1.9. (b) PDFs for SSP1−2.6. (c) PDFs for SSP4−3.4. (d) PDFs for SSP2−4.5.

Figure 2.8 also shows PDFs of ΔT_{2100} from CMIP6 models. Consistent with many prior studies, including the Reduced Complexity Model Intercomparison Project (Nicholls et al., 2020; Nicholls et al., 2021), the free-running CMIP6 models exhibit larger end-of-century warming than projected by our model.

Tokarska *et al.* (2020b) reported that observationally constrained CMIP6 projections of end-of century warming are 9% to 13% lower than unconstrained CMIP6 projections for SSP1−2.6 and SSP2−4.5, respectively. Tokarska *et al.* (2020b) found the median and 5−95% ranges of end-of century warming relative to a 1995−2014 baseline to be 0.94 [0.41 to 1.46] ºC and 1.84 [1.15 to 2.52] ºC for SSP1−2.6 and SSP2−4.5, respectively, using observationally constrained CMIP6 models. Our values of ΔT_{2100} in Table 2.1, relative to 1995−2014, are 0.81 [0.32 to 1.27] ºC and 1.74 [1.06 to 2.34] ºC for SSP1−2.6 and SSP2−4.5. Consequently, our quantification of ΔT_{2100} is in good agreement with the findings of Tokarska *et al.* (2020b). As for the comparison with Fig. 4.2a of AR6 (Lee et al., 2021), it is important to highlight that our estimates use GMST, whereas Tokarska *et al.* (2020b) presents (adjusted) GSAT. Therefore, some of the differences between the forecasts can be explained by the difference in GSAT and GMST. Further, Chylek *et al.* (2024) recently found GSAT to be 2.41 ºC in the year 2100 for SSP2−4.5 using a set of CMIP6 models that accurately reproduce the 2014−2023 warming, about 0.5 ºC smaller than the average obtained from an unconstrained ensemble, in reasonably good agreement with our median estimate for ΔT_{2100} of 2.6 ºC.

In summary, our projections of ΔT_{2100} using the EM−GC model, trained within the AR6 Framework, produces estimates consistent with the output of observationally constrained CMIP6 models presented in numerous other studies. These estimates were obtained assuming climate feedback is constant between 1850 and 2100 (that is, $\alpha' = 0$ W m^{-2} K^{-1}). The close consistency between our ΔT_{2100} projections and the prior literature provides confidence in the virtue of the assumption that climate feedback has been mainly constant over the past century and a half, even though the actual values of climate feedback is not well known. The interested reader is directed

towards Sect. 3.3.6 of McBride *et al.* (2021), for projections of ΔT in our model framework that allow the value of climate feedback to vary over time.

Table 2.3: EM−GC computed probabilities of achieving the Paris Agreement target (1.5 ºC) and upper limit (2.0 ºC). Columns with the "Baseline" header represent EM−GC simulations using the Baseline Framework, while "AR6" represents simulations utilizing the AR6 Framework. The values presented in this table are derived from the PDFs shown in Fig. 2.8.

	Paris 1.5 ºC		**Paris 2.0 ºC**	
	Baseline	**AR6**	**Baseline**	**AR6**
SSP1−1.9	81%	70%	98%	100%
SSP1−2.6	54%	32%	87%	85%
SSP4−3.4	21%	3%	65%	40%
SSP2−4.5	1%	0%	35%	8%

We conclude this section by evaluating the probability of achieving both the target (1.5 ºC) and upper limit (2.0 ºC) of the Paris Agreement (PA). Table 2.3 provides the probability that end-of century warming will be below either the target or the upper limit, relative to pre-industrial conditions. These estimates were obtained from our probabilistic forecasts of ΔT, for both the Baseline and AR6 Frameworks (Fig. 2.8). As shown above, median projections of ΔT_{2100} are larger within the AR6 Framework relative to the Baseline for all four SSPs, which leads to a decline in the probability of accomplishing the PA within the AR6 Framework (Table 2.3). For the SSP1−1.9 and SSP1−2.6 scenarios, the probability of limiting global warming to 2.0 ºC is high (at least 85%) for both model frameworks. For SSP4−3.4, the probability of limiting warming to 2.0 ºC falls from 65% (Baseline) to 40% (AR6). Most notably, the 2.0 ºC probability drops from 35% to 8%, for the SSP2−4.5 scenario. The 1.5 ºC warming probabilities for the AR6 Framework are all uniformly lower than for the Baseline Framework, with the SSP1−2.6 scenario dropping from 54% (Baseline) to 32% (AR6). The takeaway message from Table 2.3 is that, for society to have high confidence in achieving at least the upper limit of the PA, the radiative forcing of climate due to GHGs must

be placed close to the SSP1−2.6 pathway over the coming decades. More aggressive reductions in GHG radiative forcing are needed to achieve the target of the PA, such as those of the SSP1−1.9 scenario.

2.4 Conclusions

The extent of global warming is proportional to the ERF from greenhouse gases and tropospheric aerosols. In this work, we use a multiple linear regression energy balance model (EM−GC) to quantify how updates to the ERF formulations of GHGs and tropospheric aerosols adapted by the IPCC AR6 report (termed AR6 Framework in our study) impact estimates of climate sensitivity and projected future warming compared to forecasts made based on pre−AR6 datasets (Baseline Framework). Our study focuses on four policy-relevant SSP scenarios: SSP1−1.9, SSP1−2.6, SSP4−3.4 and SSP2−4.5 (O'Neill et al., 2014; O'Neill et al., 2016). Our model framework has two key elements: numerical representation of ocean heat export as well as the impact of uncertainty in radiative forcing due to tropospheric aerosols. The numerical values given below are results based on 160,000 member ensembles for each SSP.

First, we compare ERF for GHGs and tropospheric aerosols between the two Frameworks. We find that the projected ERF due to GHGs – particularly CO_2 and CH_4 − is considerably higher in the AR6 Framework relative to the Baseline, for all four of the SSP scenarios. This increase in ERF_{GHG} originates from the updated assessments of future concentrations as well as updates to the formulations of ERF due to GHGs in AR6, in combination with updated adjustments to the RF of GHGs that now include responses throughout the troposphere, in addition to the stratosphere (Smith et al., 2018b; Hodnebrog et al., 2020; Meinshausen et al., 2020; Forster et al., 2021a; Smith et al., 2021a; IPCC, 2021a). End-of-century ERF is found to be up to 0.7 W m^{-2} higher within the AR6 Framework relative to the Baseline for SSP2−4.5. While some minor deviation of end-of-

century ERF from the nameplate RF value of SSP scenarios is expected (van Vuuren et al., 2014), the AR6 Framework results in a level of increase in ERF such that end-of-century values are considerably larger than the nameplate RF for all four SSP scenarios.

The magnitude of Effective Climate Sensitivity (EffCS) inferred from the historical GSMT record was found to be 2.29 [1.54 to 3.11 ºC, 5−95% range] within the AR6 Framework, and 2.26 [1.45 to 4.37 ºC] for the Baseline Framework. The median value of EffCS is nearly identical between the two Frameworks, and there is a much narrower range within the AR6 Framework. Equilibrium Climate Sensitivity (ECS) is estimated to be 3.24 [1.92 to 5.15 ºC] within the AR6 Framework, using the AR6 best estimate for the pattern effect ($\alpha' = 0.5$ W m^{-2} K^{-1}). This estimate of ECS is quite similar to the AR6 assessment of 3.0 [2.0 to 5.0 ºC] given in Table 7.13 of Forster *et al.* (2021a). Overall, our estimates of EffCS and ECS within the AR6 Framework compare very well with values reported by several other recent studies (Armour et al., 2024; Cooper et al., 2024; Skeie et al., 2024b). The rate of human−induced warming between 1974 and 2014 (AAWR) was found to be 0.18 [0.13 to 0.21 ºC $decade^{-1}$] within the AR6 Framework, a slight increase relative to the central estimate and range of 0.16 [0.12 to 0.20 ºC $decade^{-1}$] for the Baseline Framework. Our estimate of AAWR within the AR6 Framework is also consistent with other recent studies (Gulev et al., 2021; Forster et al., 2023; Samset et al., 2023).

Our projections of GMST show good consistency with GSAT estimates from observationally constrained CMIP6 ensembles but fall below the estimates of global warming when considering unconstrained CMIP6 ensembles. Overall, our estimates of EffCS, ECS, AAWR and end-of century warming using the AR6 Framework are all consistent with values found by CMIP6 models that accurately reproduce observed warming trends over the past three or four

decades. Our work highlights the importance of ensuring that CMIP6 models used for policy purposes succeed in reproducing observed trends in GMST.

Our probabilistic projections on future warming consider the uncertainty in the magnitude of ERF from tropospheric aerosols, as assessed by AR6 and AR5, for the AR6 and Baseline Frameworks, respectively. Global warming projections that utilize the uncertainty in aerosol ERF is a common product of RCMs (Nicholls et al., 2020; Nicholls et al., 2021; Hope et al., 2017; McBride et al., 2021) and is not usually found using GCMs due to the computational demand of global models. Median projections on end-of century warming using our RCM, are higher by 0.2 ºC to 0.4 ºC within the AR6 Framework relative to projections found in the Baseline Framework. This increase corresponds to a general decline in the likelihood of limiting warming to the Paris Agreement (PA) thresholds, for the AR6 Framework compared to the Baseline. Notably, model simulations using SSP2−4.5 and SSP1−2.6 − which reflect trends in the absence of further climate policies and full implementation of currently proposed emission targets (Meinshausen et al., 2024) – are found to offer 32% and 0% chance of accomplishing the PA target of limiting the rise in GMST to 1.5 ºC by 2100. Model simulations conducted using the SSP4−3.4 (intermediate scenario between SSP1−2.6 and SSP2−4.5) and SSP1−1.9 (aggressive future reductions in GHG emissions) show probabilities of 3% and 70% of limiting warming to 1.5 ºC by end-of-century. The likelihood of limiting warming to the PA upper limit of 2.0 ºC is found to be 40% and 8% within the AR6 Framework for SSP4−3.4 and SSP2−4.5, respectively. There is high confidence (85% and 100% probabilities) that global warming could be limited to 2.0 ºC if the radiative forcing of climate due to GHGs could be placed on either the SSP1−2.6 or SSP1−1.9 pathways.

Appendix A

We provide a summary of the ERF formulations used to compute ERF due to GHGs for the Baseline and AR6 frameworks in Table 2A.1. The coefficients used in the equations of Table 2A.1 are listed in Table 2A.2. Table 2A.3 summarizes the central−, 1σ− and 2σ values for ERF_{AER} from which the Gaussians used to weigh the EM−GC output ensemble are constructed. These numerical values correspond to the highlighted points on the Gaussians shown in Figure 2.3a−b and are derived from the IPCC range of ERF_{AER} shown in Table 2A.3. For the Baseline framework, the 1σ boundaries of the Gaussian were set to match the IPCC AR5 "likely range" of ERF_{AER}, while the 2σ boundaries were adapted from the AR5 range (Table 2A.3). For the AR6 framework, the 2σ boundaries were adapted from the AR6 range for ERF_{AER} in 2019, while the 1σ boundaries were determined to be halfway between the 2σ ERF and the IPCC "Central" estimate (Table 2A.3), for each side of the Gaussian.

The Planck−feedback is considered in our work through the mathematical representation shown in Eqs. 2.1−2 with the use of the λ_p constant. For both frameworks, we use the value of 3.2 W m^{-2} $^{o}C^{-1}$ for λ_p. This value is consistent with the CMIP5 mean Planck−feedback of −3.2 W m^{-2} $^{o}C^{-1}$ in Table 7.10 of Forster *et al.* (2021b). The CMIP6−based updated central estimate for the Planck feedback is −3.22 W m^{-2} $^{o}C^{-1}$ (Table 7.10 of Forster *et al.* (2021b)). We ignore this minor difference between the CMIP5 and CMIP6−based value for the Planck feedback in our work and use the same value of 3.2 W m^{-2} $^{o}C^{-1}$ for λ_p for the simulations within both frameworks.

Equation A2.1 showcases the mathematical form of the ocean heat uptake efficiency constant κ, used in Eq. (2.4), following McBride *et al.* (2021). OHE in Eq. (2A.1) represents ocean heat export, and is quantified as the slope of a linear fit to the observed OHC record based on Canty *et al.* (2013). During the training of the model, κ is computed using the computed

anthropogenic warming with a 6 year lag as shown in the denominator in Eq. (2A.1). A lag of 6 years is used to account for the fact that it takes about 6 years for energy from the atmosphere to heat the upper ocean and penetrate the depth of the oceans. EM−GC simulations are insensitive to whether a 6 year or 10 year lag for OHE are used, as described in Sect. 2.1 of McBride *et al.* (2021). The f_0 constant in Eq. (2A.1) with a value of 8.76×10^{-5} ºC m^2 W^{-1} following McBride *et al.* (2021).

Equations 2A.2−2A.4 show the computation of the three separate χ^2 values, used to quantify the goodness of the fit to the historical GMST record for a given combination of λ_Σ and $ERF_{AER,t}$. In Eqs. 2A.2−2A.4, $<\Delta T_{OBS}>$, $<\Delta T_{MDL}>$ and $<\sigma_{OBS}>$ correspond to the annually averaged observed and modeled GMST anomaly, and the observational uncertainty of the GMST record, respectively. Annual averages are used instead of monthly values based on the Supplement of Canty *et al.* (2013) and Section 2.1 of McBride *et al.* (2021). More details on the computation of χ^2 values are provided in Section 2.1 of McBride *et al*. (2021). Only those fits to the historical GMST record are accepted, where all three χ^2 parameters are lower than 2.0.

Figure 2A.1 provides a visual depiction of the EM−GC ERF_{AER} ensemble, obtained by scaling the IPCC best−estimate time series by a series of constant multiplicative factors, as described in Section 2.2.4. We do not show every ensemble member on this figure to avoid visual clutter. Figure 2A.2 shows values of ΔT_{2100} within the Baseline Framework for the entire λ_Σ−$ERF_{AER,t}$ grid. This figure is analogous to Fig. 2.6 of the main text, where values of ΔT_{2100} are shown for the AR6 Framework. The numerical values for the range of ΔT_{2100} from Fig. 2A.2 are also listed in Table 2.1 of our paper. Figure 2A.3 shows the time-dependent GMST forecast for the Baseline Framework. This figure is analogous to Fig. 2.7 of the main paper, where the time-dependent GMST projections are shown for the AR6 Framework. Similarly to Fig. 2.7, the

projected times of crossing the 1.5 ºC and 2.0 ºC thresholds at 5%, 50% and 95% probabilities are shown with gold circles on Fig. 2A.3 as well. The crossover years marked in Fig. 2A.3 are listed in Table 2.2 of the main paper, alongside values derived from the simulations within the AR6 Framework (Fig. 2.7).

Table 2A.1: Formulations of SARF, and tropospheric adjustments used to compute ERF for the Baseline and AR6 frameworks. C, M and N represent the concentrations of CO_2, CH_4 and N_2O, respectively, at a given time. C_0, M_0 and N_0 are the pre−industrial concentrations of these three GHGs. Values of C_0, M_0 and N_0 used in this study are listed in Table 2A.2. Coefficients used in the SARF formulations are also listed in Table 2A.2.

Frame-work	GHG	SARF Formula	Trop. Adj.	Primary References
Baseline	CO_2	$SARF = \alpha_{CO2} \ln(\frac{C}{C_0})$	None	(Myhre et al., 1998; Myhre et al., 2013b)
	CH_4	$SARF = \alpha_{CH4}\left(\sqrt{M} - \sqrt{M_0}\right) - (f(M, N_0) - f(M_0, N_0))$ where $f(M,N) = 0.47 \ln(1 + 2.01 \times 10^{-5}(MN)^{0.75} + 5.31 \times 10^{-15} \times M(MN)^{1.52})$	None	
	N_2O	$SARF = \alpha_{N2O}\left(\sqrt{N} - \sqrt{N_0}\right) - (f(M_0, N) - f(M_0, N_0))$ where $f(M,N) = 0.47 \ln(1 + 2.01 \times 10^{-5}(MN)^{0.75} + 5.31 \times 10^{-15} \times M(MN)^{1.52})$	None	
AR6	CO_2	$C_{\alpha_{max}} = C_0 - \frac{b_1}{2a_1}$ $\alpha' = \begin{cases} d_1 - \frac{b_1^2}{4a_1} \; if \; C > C_{\alpha_{max}} \\ d_1 + a_1(C - C_0)^2 + b_1(C - C_0) \; if \; C_0 < C < C_{\alpha_{max}} \\ d_1 \; if \; C < C_0 \end{cases}$ $\alpha_{N2O} = C_1 \times \sqrt{N}$ $SARF = (\alpha' + \alpha_{N2O}) \times \ln(\frac{C}{C_0})$	+5%	(Meinshausen et al., 2020; Forster et al., 2021b; Smith et al., 2021a)
	CH_4	$SARF = (a_3\sqrt{M} + b_3\sqrt{N} + d_3)(\sqrt{M} - \sqrt{M_0})$	−14%	
	N_2O	$SARF = (a_2\sqrt{C} + b_2\sqrt{N} + c_2\sqrt{M} + d_2)(\sqrt{N} - \sqrt{N_0})$	+7%	

Table 2A.2: Coefficients and pre−industrial concentrations of GHGs used in the formulations listed in Table 2A.1 for the computation of SARF and ERF in this study.

Framework	GHG	SARF Coefficients	Primary References
Baseline	CO_2	α_{CO2}= 5.35 W m^{-2} C_0= 278 ppm	(Myhre et al., 1998; Myhre et al., 2013a; Myhre et al., 2013b)
	CH_4	α_{CH4}= 0.036 W m^{-2} $ppb^{-1/2}$ M_0= 722 ppb N_0= 270 ppb	
	N_2O	α_{N2O}= 0.12 W m^{-2} $ppb^{-1/2}$ M_0= 722 ppb N_0= 270 ppb	
AR6	CO_2	a_1= −2.4785 × 10^{-7} W m^{-2} ppm^{-2} b_1= 7.5906 × 10^{-4} W m^{-2} ppm^{-1} c_1= −2.1492 × 10^{-3} W m^{-2} $ppb^{-1/2}$ d_1= 5.2488 W m^{-2} C_0= 278.3 ppm	(Meinshausen et al., 2020; Forster et al., 2021b; Smith et al., 2021a)
	CH_4	a_3= −8.9603 × 10^{-5} W m^{-2} ppb^{-1} b_3= −1.2462 × 10^{-4} W m^{-2} ppb^{-1} c_3= 0.045194 W m^{-2} $ppb^{-1/2}$ M_0= 729 ppb	
	N_2O	a_2= −3.4197 × 10^{-4} W m^{-2} $ppm^{-1/2}$ $ppb^{-1/2}$ b_2= 2.5455 × 10^{-4} W m^{-2} ppb^{-1} c_2= −2.4357 × 10^{-4} W m^{-2} ppb^{-1} d_2= 0.12173 W m^{-2} $ppb^{-1/2}$ N_0= 270.1 ppb	

Table 2A.3: Central values, 1σ and 2σ boundaries of the Gaussians used to weigh the EM−GC output grid for the Baseline and AR6 frameworks. Values shown in this table are marked by circles on the Gaussians in Fig. 2.3a−b.

Frame-work	Reference year (t)	$ERF_{AER,t}$ (W m^{-2})						
		2σ	**1σ**	**Central**	**1σ**	**2σ**	**Corresponding IPCC Range**	**Primary References**
Baseline	2011	−0.1	−0.4	−0.9	−1.5	−1.9	−0.9 [−0.1 to −1.9] (AR5 range) and [−0.4 to −1.5] (AR5 "likely" range)	(Myhre et al., 2013b)
AR6	2019	−0.4	−0.75	−1.1	−1.4	−1.7	−1.1 [−0.4 to −1.7] (AR6 range)	(Forster et al., 2021b)

$$\kappa = \frac{OHE \times \Delta t}{\int_{t_{START}}^{t_{END}} \left(\left[\frac{1+\gamma}{\lambda_p}\left(RF_{GHG,i-72}+RF_{AER,i-72}+RF_{LUC,i-72}\right)\right]-[f_0 \sum_0^{i-72} Q_{OCEAN}]\right)dt} \quad (2A.1)$$

$$\chi^2_{ATM} = \frac{1}{N_{YEARS}-N_{FITTING\ PARAMETERS}-1} \times \sum_{j=1}^{N_{YEARS}} \frac{1}{\langle\sigma_{OBS}\rangle^2} \left(\langle\Delta T_{OBS,j}\rangle - \langle\Delta T_{MDL,j}\rangle\right)^2 \quad (2A.2)$$

$$\chi^2_{RECENT} = \frac{1}{N_{YEARS,REC}-N_{FITTING\ PARAMETERS}-1} \times \sum_{j=1}^{N_{YEARS,REC}} \frac{1}{\langle\sigma_{OBS}\rangle^2} \left(\langle\Delta T_{OBS,j}\rangle - \langle\Delta T_{MDL,j}\rangle\right)^2 \quad (2A.3)$$

$$\chi^2_{OCEAN} = \frac{1}{N_{YEARS,OHC}-N_{FITTING\ PARAMETERS}-1} \times \sum_{j=1}^{N_{YEARS,OHC}} \frac{1}{\langle\sigma_{OBS}\rangle^2} \left(\langle \mathrm{OHC}_{OBS,j}\rangle - \langle \mathrm{OHC}_{MDL,j}\rangle\right)^2 \quad (2A.4)$$

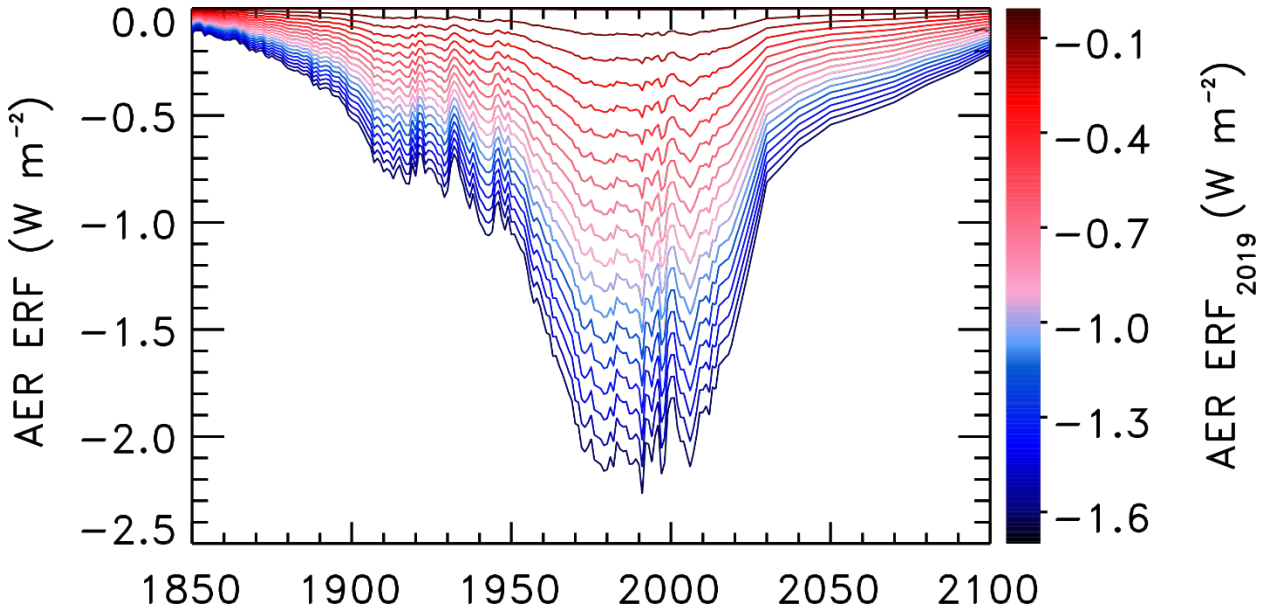

Figure 2A.1: Visual depiction of the EM−GC ERF_{AER} ensemble used in the AR6 Framework, generated by the scaling of the IPCC−prescribed timeseries of ERF_{AER} from Annex III of AR6 (IPCC, 2021a) as described in Sect. 2.2.4. For this figure, beyond 2019, the SSP1−1.9 time series was scaled. Colors denote ERF_{AER} in 2019 as indicated by the color bar. Not all ensemble members are shown to avoid visual clutter.

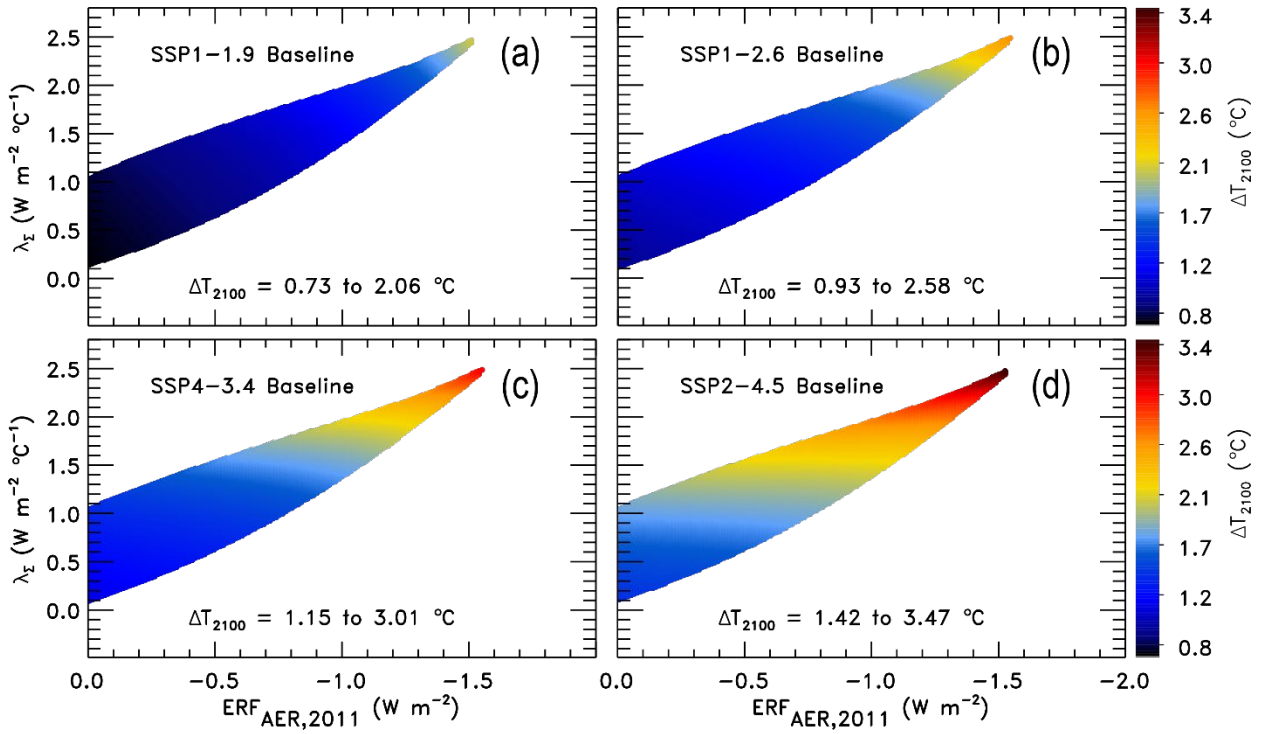

Figure 2A.2: Projected end-of century warming as in Fig. 2.6, with results being shown for the Baseline framework.

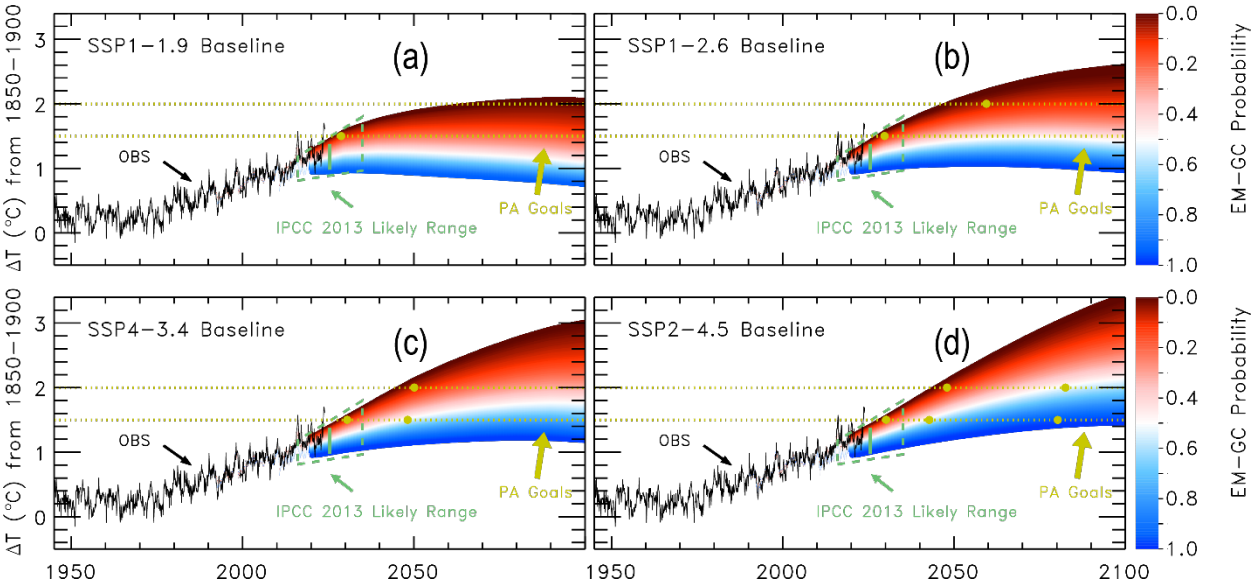

Figure 2A.3: Time-dependent probabilistic GMST forecast as in Fig. 2.7, but for the Baseline framework.

Chapter 3: Implementation of a New Two-layer Energy Balance Module to the EM−GC Model

3.1 Introduction

Earlier versions of EM−GC used a simplified two-layer model to represent the loss of heat to oceans, which, based on the analysis of ocean warming extracted from the General Circulation Models of phase 5 of the Coupled Model Intercomparison Project (CMIP5 GCMs), assumed that 13.7% of the rise in total OHC occurs in the upper 100 meters of the ocean (see Sect. 2.1 of McBride et al., (2021)). In this Chapter, we describe the technical implementation of EBM−1 (Held et al., 2010; Geoffroy et al., 2013b) into the EM−GC model, the calibration of the EBM using observed time series of GMST and OHC, and the results of our benchmark simulations performed using the updated EBM component of our model.

One weakness of the representation of Ocean Heat Export (OHE) used in earlier versions of EM−GC (Canty et al., 2013; Hope et al., 2020; McBride et al., 2021; Farago et al., 2025) is that the temperature response to an abrupt change in ERF leads to an immediate response of GMST, similar to the "deep-layer model" formulation described in Gregory et al., (2015). The updated ocean module presented here provides a more realistic short-term temperature response to sudden changes in ERF, relative to previous versions of the EM−GC model, which were primarily used to quantify the long-term response of GMST to changes in ERF under various Representative Concentration Pathway (RCP) (Canty et al., 2013; Mascioli et al., 2012; Hope et al., 2020) and Shared Socioeconomic Pathway (SSP) scenarios (McBride et al., 2021; Farago et al., 2025).

3.2 Implementation of EBM−1 in EM−GC

The two-layer approximation separates the climate system into two layers, an upper layer of small heat capacity, representing the well-mixed layer of oceans, as well as the land and the

atmosphere, and the lower layer, which corresponds to the deeper layers of Earth's oceans. The atmosphere and the land are assumed to have a negligible heat capacity relative to that of the oceans, and therefore, the states of the upper and lower layers are described by Eqs. (3.1) and (3.2), respectively (Geoffroy et al., 2013a; Geoffroy et al., 2013b). The exact mathematical formulation that describes the states of the two layers in the two-layer EBM differs between studies. Here and throughout, our formulation is based on Eqs. (1) and (2) of Geoffroy et al., (2013a) and Eq. (7.SM.2.1) of Smith et al., (2021a).

$$C_u \frac{dT_u}{dt} = F - \alpha T_u - \gamma\varepsilon(T_u - T_d) \tag{3.1}$$

$$C_d \frac{dT_d}{dt} = \gamma(T_u - T_d) \tag{3.2}$$

In Eqs. (3.1) and (3.2), T_u and T_d (units of K) represent the temperature anomalies of the upper, and the lower layer, respectively, relative to pre-industrial conditions. The quantities C_u and C_d are the effective heat capacities of the upper and lower layers per unit area (in units of J m^{-2} K^{-1}), respectively. The quantity F is the effective radiative forcing of the climate (units of W m^{-2}) relative to pre-industrial conditions, while α is the climate feedback parameter (in W m^{-2} K^{-1}). The quantity γ is the heat transport coefficient between the two layers of the ocean (in W m^{-2} K^{-1}). The dimensionless parameter ε represents the efficacy of the deep ocean heat uptake (Geoffroy et al., 2013a; Geoffroy et al., 2013b). The two-layer EBM described by Eqs. (3.1) and (3.2) is commonly termed EBM−ε.

The EBM−ε representation can be simplified using the assumption that ε = 1 (Geoffroy et al., 2013b). This simplification leads to the formulation commonly referred to as EBM−1. As shown in Geoffroy et al., (2013b), the EBM−1 representation provides a highly similar temperature response to EBM−ε on the timescale of our simulations, but requires the calibration of one less parameter. Therefore, we implemented the EBM−1 representation into EM−GC, and have

assumed that ε = 1 throughout this paper. Equations (3.1) and (3.2) are converted to a monthly time grid to match the temporal resolution of EM−GC as described below, and are then used to express the temperature anomalies of the upper (T_u) and lower ocean layers (T_d). We consider the time series of the temperature anomaly of the upper layer (T_u) to be equal to the anthropogenic contribution to the GMST (ΔT_{ANTH}). This treatment of OHE is consistent with earlier versions of the EM−GC model, which also assumed that the warming of the climate and the oceans are primarily driven by anthropogenic activity.

Internally, EM−GC uses a time-invariant climate feedback parameter λ_Σ, which is the sum of all feedbacks (water vapor, lapse rate, clouds, etc.), except for the Planck-feedback (McBride et al., 2021; Farago et al., 2025). The quantity λ_Σ relates to the climate feedback parameter α in Eq. (3.1) such that $\alpha = \lambda_p - \lambda_\Sigma$, where λ_p is the response of a black body to a perturbation in the absence of climate feedback (Bony et al., 2006), and has the value of $\lambda_p = 3.2$ W m^{-2} (McBride et al., 2021).

To convert Eqs. (3.1) and (3.2) to a monthly timescale, we use the backward Euler method, which assumes that the change in the temperature anomalies between two timesteps (ΔT_u and ΔT_d for the upper and lower layers, respectively) are expressed as shown in Eq. (3.3). We use the backward Euler method because this formulation is less sensitive to the size of the timestep and reduces numerical instability for stiff differential equations.

$$\frac{dT_u}{dt} = \frac{\Delta T_u}{\Delta t} = \left(T_{u,i} - T_{u,i-1}\right) \; and \; \frac{dT_d}{dt} = \frac{\Delta T_d}{\Delta t} = \left(T_{d,i} - T_{d,i-1}\right) \tag{3.3}$$

Consequently, Eqs. (3.1) and (3.2) are expressed on a monthly grid as shown in Eqs. (3.4) and (3.5), where i is the index of a given month, and Δt represents the length of each month, in units of seconds.

$$C_u(T_{u,i} - T_{u,i-1})\frac{1}{\Delta t} = F_i - \alpha T_{u,i} - \gamma(T_{u,i} - T_{d,i}) \tag{3.4}$$

$$C_d(T_{d,i} - T_{d,i-1})\frac{1}{\Delta t} = \gamma(T_{u,i} - T_{d,i}) \tag{3.5}$$

Rearranging Eqs. (3.4) and (3.5) to express the temperature anomalies of the upper and lower layers at a given time ($T_{u,i}$ and $T_{d,i}$, respectively) yields Eqs. (3.6) and (3.7):

$$T_{u,i} = \frac{F_i + \gamma T_{d,i} + \frac{C_u}{\Delta t} T_{u,i-1}}{(\frac{C_u}{\Delta t} + (\alpha + \gamma))} \tag{3.6}$$

$$T_{d,i} = \frac{\gamma T_{u,i} + \frac{C_d}{\Delta t} T_{d,i-1}}{(\frac{C_d}{\Delta t} + \gamma)} \tag{3.7}$$

The expression of $T_{u,i}$ in Eq. (3.6) includes the value of $T_{d,i}$; similarly, the $T_{d,i}$ in Eq. (3.7) is a function of $T_{u,i}$. We define the values of C_u and C_d prior to the beginning of the simulation (see Sect. 3.4), while the time series of effective radiative forcing, F(t) and the climate feedback parameter α are considered using an ensemble method. Consequently, for each ensemble member, a value of the parameter γ defines a pair of T_u−T_d time series. This feature is highly similar to earlier versions of the EM−GC ocean module (Hope et al., 2020; McBride et al., 2021; Farago et al., 2025), where a given value of the ocean heat transfer parameter defined the temperature anomaly time series of the upper layer of oceans for a given ensemble member. A key difference between the updated two-layer EBM component in comparison to previous versions of EM−GC, is that in earlier versions of EM−GC, the temperature of the upper layer was computed such that a fixed percentage of total OHC is retained in the upper layer of the oceans. Consequently, earlier versions of our model resulted in an immediate jump in modelled GMST when a step-forcing was applied, similar to the behavior of the "deep-layer model" formulation described in Gregory et al., (2015), thereby overestimating the short-term temperature response to sudden increases in ERF. The two-layer EBM component presented here improves the energy balance component of EM−GC to provide a more realistic short-term response to sudden changes in radiative forcing, while retaining the concept of the iterative loop used to quantify the ocean heat transfer parameter based on observations, that was used in earlier versions of the EM−GC model (Hope et al., 2020;

McBride et al., 2021; Farago et al., 2025). We present the observation-driven calibration of the ocean heat transfer parameter γ in Sect. 3.3.

To compute $T_{u,i}$ from Eqs. (3.6) and (3.7), we substitute $T_{d,i}$ from Eq. (3.7) into Eq. (3.6), which we then rearrange to express $T_{u,i}$ as shown in Eq. (3.8).

$$T_{u,i} = \frac{F_i + \frac{C_u}{\Delta t} T_{u,i-1} + \frac{\gamma \frac{C_d}{\Delta t} T_{d,i-1}}{(\frac{C_d}{\Delta t} + \gamma)}}{(\frac{C_u}{\Delta t} + (\alpha + \gamma) - \frac{\gamma^2}{(\frac{C_d}{\Delta t} + \gamma)})} \quad (3.8)$$

The expression of $T_{u,i}$ shown in Eq. (3.8) is only affected by various constants (γ,C_u,C_d,α and Δt), the value of radiative forcing in a given month (F_i), and the temperature anomalies of the upper and lower layers in the previous month ($T_{u,i-1}$ and $T_{d,i-1}$, respectively). Using the initial conditions of T_u (t = 0) = T_d (t = 0) = 0 K, and F (t = 0) = 0 W m^{-2}, which correspond to the unperturbed state of the pre-industrial climate, the model computes the time series of T_u, which is then substituted into Eq. (3.7) to obtain the time series of T_d for a given value of the parameter γ.

3.3 Quantification of the ocean heat transfer parameter γ

The two-layer EBM is commonly calibrated using CMIP5/6 simulations, where the concentration of CO_2 is abruptly quadrupled (hereafter termed *abrupt4xCO_2* simulations) (Geoffroy et al., 2013a; Geoffroy et al., 2013b; Smith et al., 2021a). Here, we present the calibration of the ocean heat transfer parameter γ within the EBM−1 component of EM−GC, using the observed rise in GMST and OHC.

In earlier versions of the EM−GC model (Hope et al., 2020; McBride et al., 2021; Farago et al., 2025), the ocean heat transfer parameter, which was termed κ in these papers, was quantified based on the observed rise in OHC, using an iterative cycle between the value of κ, and the temperature of the well-mixed layer of the ocean. The calibration of EBM−1 described here

follows the same logic: the model runs an iterative cycle between the value of the parameter γ, and the pair of temperature anomaly time series T_u and T_d. The heat capacities of the upper and lower layers (C_u and C_d, respectively) are pre-defined at the beginning of the simulation. We describe the setup of these two parameters in Sect. 3.4.

The observed rise in OHC over a given period can be approximated using the slope of a linear fit to the observed OHC record (Ocean Heat Export, OHE) following Canty et al., (2013). Similar to C_u and C_d, OHE is also expressed per unit area of the oceans, and has the dimension of W m^{-2}. We quantify the parameter γ by making equal the modelled and observed rise in OHC over the period where OHC data is available as shown in Eq. (3.9). In Eq. (3.9), *start* and *finish* correspond to the first and last months of OHC data availability during the training period (1850 to 2019) of the model. In this paper, we use OHC data starting in 1955, and therefore, *start* and *finish* correspond to January 1955 and December 2019, respectively. The quantity *tspn* is the difference in time between *start* and *finish*, in the units of seconds.

$$\int_{start}^{finish}\left(C_u \frac{dT_u}{dt} + C_d \frac{dT_d}{dt}\right) dt = OHE \times tspn \tag{3.9}$$

By substituting Eq. (3.2) into Eq. (3.9), we obtain Eq. (3.10), which is then rearranged and converted to a monthly timescale to yield the expression of γ shown in Eq. (3.11).

$$\int_{start}^{finish}\left(C_u \frac{dT_u}{dt} + \gamma(T_u - T_d)\right) dt = OHE \times tspn \tag{3.10}$$

$$\gamma = \frac{OHE \times tspn - C_u \times \sum_{start}^{finish}(T_{u,i} - T_{u,i-1})}{\sum_{start}^{finish}((T_{u,i} - T_{d,i}) \times \Delta t)} \tag{3.11}$$

An initial value of γ is used to compute the pair of T_u – T_d time series using Eqs. (3.6) and (3.7), which are then inserted into Eq. (3.11) to obtain a new value of γ. This iterative loop continues until a convergence is reached, or until the model fails to find a value of γ that is consistent with observed rise in OHC. Equation (3.11) serves as an extension of Eq. (5) from

McBride et al., (2021), and allows the quantification of the ocean heat transfer parameter γ within the updated two-layer EBM module of EM−GC, based on the observed rise in OHC.

EM−GC simulations are constrained by the model's ability to reproduce the observed rise in OHC through the use of a reduced chi-square metric, termed χ^2_{OCEAN}. We compute χ^2_{OCEAN} by using the time series of modelled and observed OHC in the upper 700 m of oceans, as shown by the red and black lines in Fig. 4.1g, respectively. Similarly to earlier versions of the EM−GC model (Hope et al., 2020; McBride et al., 2021; Farago et al., 2025), the total modelled OHC (left side of Eq. (3.10)) in EM−GC is scaled to 70% of its value to obtain the modelled OHC in the upper 700 m of oceans, using the assumption that the upper 700 m of oceans hold 70 % of the heat (IPCC, 2007). This ratio is broadly consistent with Table 2.7 of the IPCC AR6 report (Gulev et al., 2021), which estimated that about 66% of total OHC was held in the upper 700 m of oceans over the 1901 to 2018 time period.

3.4 Calibration of heat capacities

In this section, we describe the setup of the effective heat capacities of the upper and lower layers of the two-layer EBM, termed C_u and C_d, respectively. C_u and C_d are expressed per unit area of the ocean, and have the dimensions of J m^{-2} K^{-1}. Geoffroy et al., (2013a) and Geoffroy et al., (2013b) calibrated the two-layer EBM using the output of *abrupt4xCO₂* simulations from a set of CMIP5 models. Geoffroy et al., (2013b) found the values of C_u = 7.3 W yr m^{-2} K^{-1} and C_d = 106 W yr m^{-2} K^{-1} based on the CMIP5 multi-model mean, which correspond to equivalent depths of 77 and 1105 meters. For the simulations presented in this paper, we use the same equivalent depths for the two layers within our model.

An important consideration for the implementation of EBM−1 within the EM−GC is the model's sensitivity to the heat capacities of the two layers. Therefore, we performed a set of

simulations to test the sensitivity of our model output to the values of C_u and C_d. We tested three values of C_u, combined with three values of C_d, for a total of nine simulations. The equivalent depths that correspond to these heat capacities are 30, 65 and 100 m for the upper layer, and 935, 1500 and 3600 m for the lower layer. These values were picked to represent a wide range of heat capacities, and to include pairings where the ratio of C_u to C_d is similar to that inferred from CMIP5/6 simulations.

Figure 3.1 shows the values of AAWR for the λ_Σ–ERF_{AER} ensemble across the nine benchmark simulations. The panels in Fig. 3.1 correspond to the nine combinations of equivalent depths for the two layers, as indicated in the individual panels. The colored regions in Fig. 3.1 correspond to values of AAWR as indicated by the color bars to the right, for combinations of λ_Σ and $ERF_{AER,2019}$ that satisfy all three reduced χ^2 constraints. We also provide computed values of the effective climate sensitivity (EffCS) and the parameter γ for the nine benchmark simulations in a similar manner in Figs. 3B.1 and 3B.2, respectively.

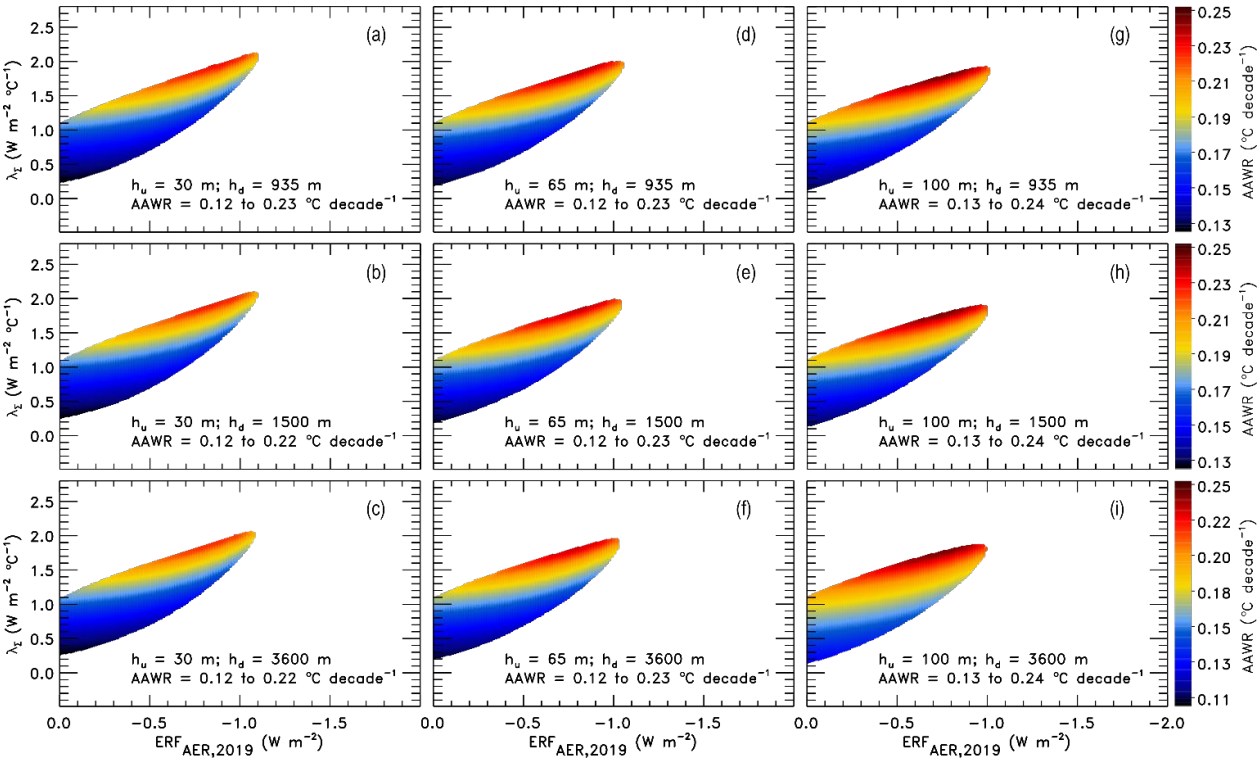

Fig. 3.1: Values of AAWR as the function of climate feedback and $ERF_{AER,2019}$, for nine different combinations of the equivalent depth of the upper (h_u) and lower (h_d) layers of the two-layer EBM.

Across the nine simulations, we find that the values of EffCS are generally consistent, while the range of AAWR is virtually identical. Therefore, while the estimated range of γ changes considerably depending on the heat capacities of the upper and the lower layers (Fig. 3B.2), the regression to the historical GMST and OHC record is largely unaffected (Figs. 3.1 and 3B.1). Further, the values of EffCS shown in Fig. 3B.1 are in good general agreement with previous estimates from the EM−GC model (Farago et al., 2025). Finally, the simulations for the IMO−0.1 scenario, described in Sect. 4.2.2.2 were also performed for all nine benchmark depth combinations. We find that the results presented in Chapter 4 are largely insensitive to the specific values of C_u and C_d used during the simulations.

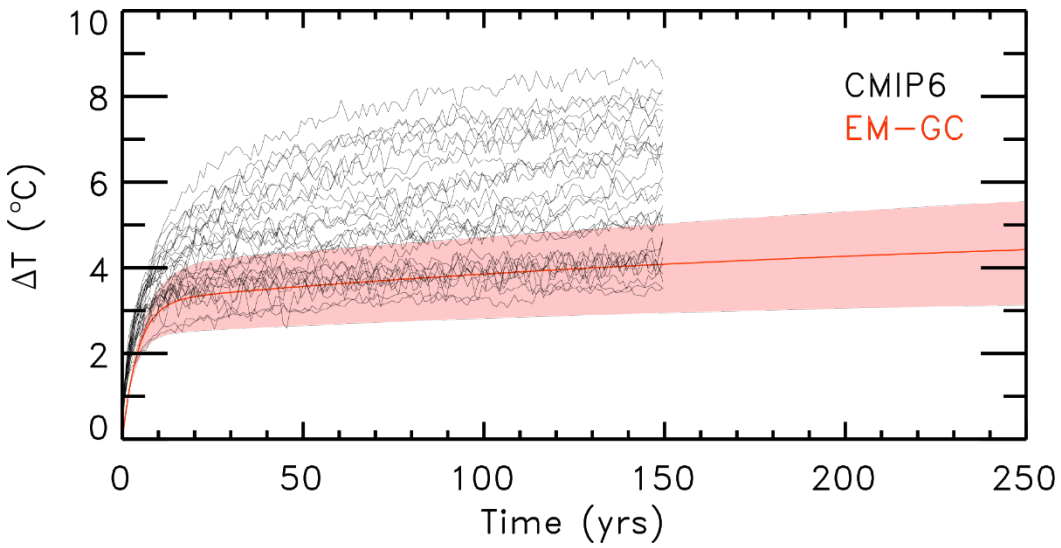

Fig. 3.2: Modelled surface temperature during an abrupt4xCO_2 experiment performed with the updated ocean module of EM−GC (red). The black lines correspond to abrupt4xCO_2 simulations from an ensemble of 28 CMIP6 models as described in McBride et al., (2021). The solid line and the shading for the EM−GC simulation correspond to the 50th percentile, and the 5−95% range, respectively.

The *abrupt4xCO_2* experiment was performed with the observationally calibrated EM−GC EBM module. This experiment used the same equivalent depths for the two layers of the EBM as

the simulations presented in Chapter 4 (77 m and 1105 m for the upper and lower layers, respectively). Fig. 3.2 shows the time evolution of the GMST under *abrupt4xCO_2* conditions projected by EM−GC (red), and by an ensemble of 28 CMIP6 models from McBride et al., (2021). McBride et al., (2021) found that eight members of this CMIP6 ensemble produces EffCS and AAWR consistent with EM−GC estimates. These models are listed in Fig. S17 of McBride et al., (2021). There are nine CMIP6 models in Fig. 3.2, which produce a temperature response that is are within the range simulated by EM−GC. Eight of these models are the same as the ones in Fig. S17 of McBride et al., (2021). In addition to these eight models, the temperature response of the GISS−E2−2−G model was also found to be consistent with EM−GC in Fig. 3.2.

Appendix B

Figures 3B.1 and 3B.2 show the EM−GC model output for the nine benchmark simulations that were used to test the sensitivity of the two-layer EBM to the heat capacities of the upper and lower layers (Sect. 3.4) in a manner similar to Fig. 3.1. Panels differ in the equivalent depth of the upper (h_u) and lower (h_d) layers used for a given simulation. Figure 3B.1 and 3B.2 show values of EffCS and the parameter γ for the nine simulations, respectively, while the values of AAWR for the nine benchmark simulations are shown in Fig. 3.1.

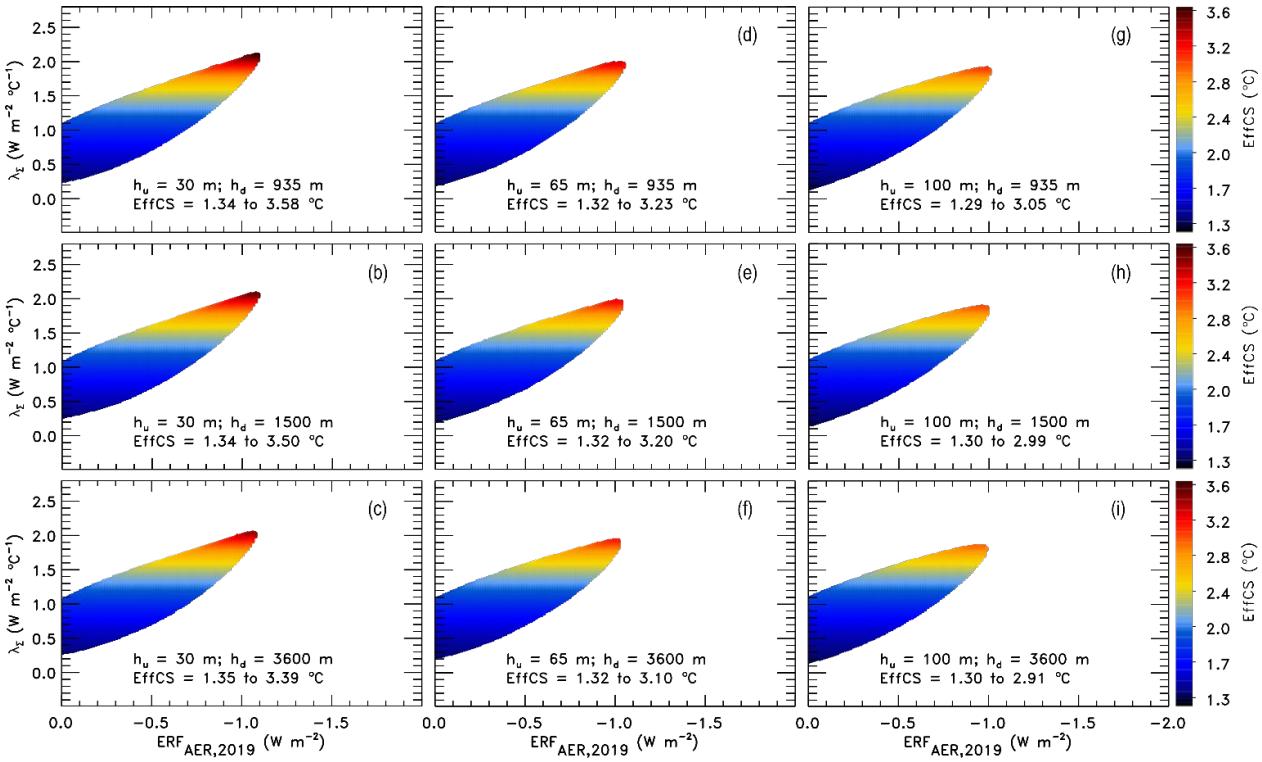

Figure 3B.1: Values of EffCS as the function of climate feedback and $ERF_{AER,2019}$, for nine different combinations of the equivalent depth of the upper (h_u) and lower (h_d) layers of the two-layer EBM.

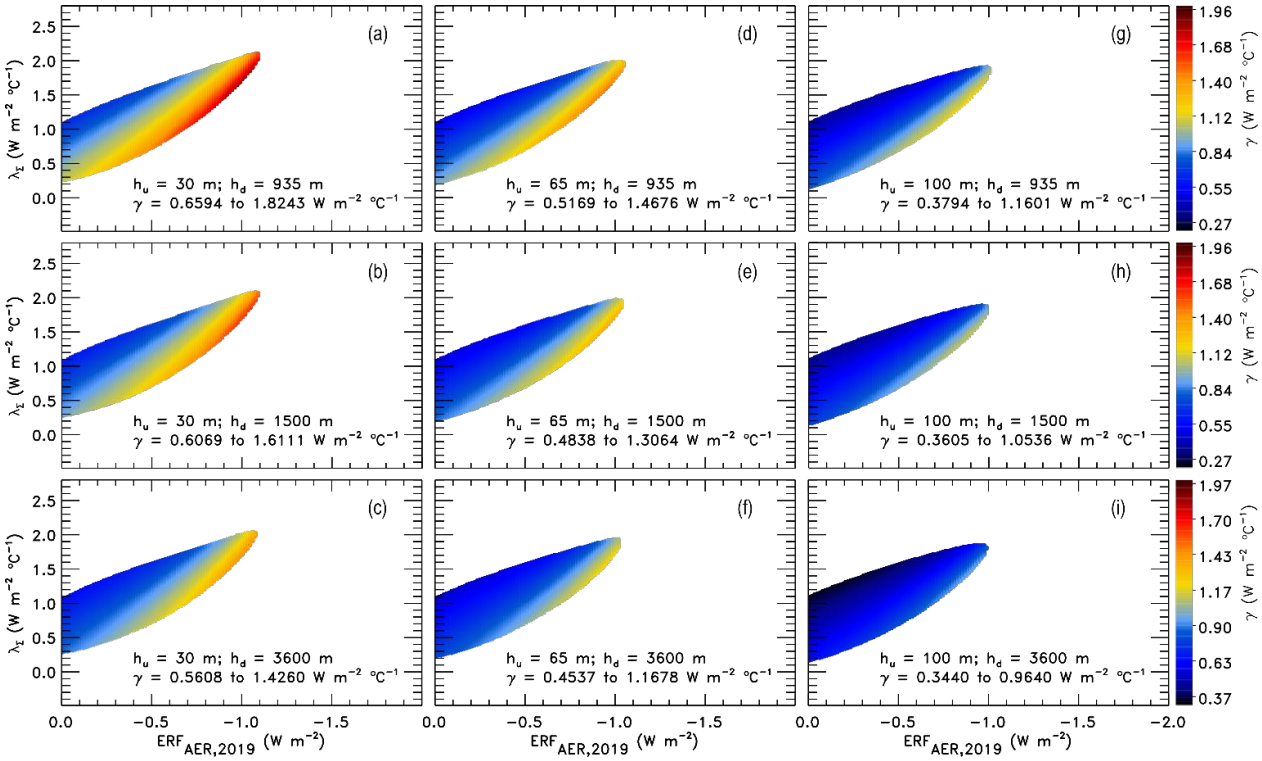

Figure 3B.2: Values of the parameter γ as the function of climate feedback and $ERF_{AER,2019}$, for nine different combinations of the equivalent depth of the upper (h_u) and lower (h_d) layers of the two-layer EBM.

Chapter 4: Quantification of the Natural and Anthropogenic Contributors to the GMST Anomalies in 2023 and 2024

4.1 Introduction

The global mean surface temperature (GMST) anomaly measured in 2023 and 2024 greatly exceeded expectations (Schmidt, 2024; Tollefson, 2025) and raised questions about the underlying cause. Several natural and anthropogenic factors, such as the onset of El Niño after a rare triple-dip La Niña event (Raghuraman et al., 2024), a record-low planetary albedo (Goessling et al., 2025), the eruption of the Hunga Ha'apai volcano (Millán et al., 2022; Vömel et al., 2022; Zhang et al., 2022; Zhu et al., 2022; Asher et al., 2023; Evan et al., 2023; Jenkins et al., 2023; Schoeberl et al., 2023; Schoeberl et al., 2024; Randel et al., 2024; Gupta et al., 2025), or the reduction of sulfur emissions from international shipping (Gettelman et al., 2024; Jordan and Henry, 2024; Quaglia and Visioni, 2024; Watson-Parris et al., 2024; Yoshioka et al., 2024; Yuan et al., 2024) are among the proposed causes of the unusually high GMST observed in 2023 and 2024.

Tropospheric sulfate aerosols, which originate from anthropogenic emissions exhibit a considerable cooling effect on GMST (Twomey, 1974; Albrecht, 1989; Bellouin et al., 2020; Forster et al., 2021a) and offset a fraction of the Greenhouse Gas (GHG) induced global warming. Efforts to improve air quality have resulted in a gradual reduction of sulfur emissions in the recent two decades (Smith and Bond, 2014). A new effort to improve air quality is the regulation on the sulfur content of fossil fuel used in international shipping, which began in January 2020 under the auspices of the International Maritime Organization (IMO). The IMO regulation limits the allowed sulfur content of marine fuels to 0.5% outside of Emission Control Areas, which is much lower than the previous value of 3.5% (IMO, 2019). Here and throughout, we refer to this regulation as

IMO2020. Sulfate aerosols are major contributors to the overall Effective Radiative Forcing (ERF) from tropospheric aerosols (ERF_{AER}), both through the aerosol direct (ERF_{ari}) and indirect (ERF_{aci}) effects (Albrecht, 1989; Twomey, 1974; Szopa et al., 2021; Forster et al., 2021a). Several recent studies have quantified how IMO2020 affects ERF_{AER} and GMST, using various observational and modelling products (Diamond, 2023; Gettelman et al., 2024; Quaglia and Visioni, 2024; Jordan and Henry, 2024; Skeie et al., 2024a; Watson-Parris et al., 2024; Yoshioka et al., 2024; Yuan et al., 2024). Table A1 of Jordan and Henry (2024) provides an overview of recent estimates on the impact of the IMO2020 regulations on ERF_{AER}.

In this paper, we quantify the impact of several natural and anthropogenic factors on the GMST using a multiple linear regression (MLR) energy balance model (EBM), the Empirical Model of Global Climate, EM−GC (Canty et al., 2013; Mascioli et al., 2012; Hope et al., 2017; McBride et al., 2021; Farago et al., 2025). Our model is trained on 170 years of historical climate data from various measurements, and provides an estimate of Effective Climate Sensitivity (EffCS) consistent with recent literature values (Farago et al., 2025). A major advantage of EM−GC is the inclusion of internal variability in simulations, a feature not present in other EBM-based analyses of the impacts of IMO2020 on GMST (Watson-Parris et al., 2024). Consequently, EM−GC has the ability to quantify the impact of various natural (such as El Niño Southern Oscillation, ENSO) and anthropogenic factors (i.e., IMO2020) on the GMST anomaly in a computationally efficient manner. For this paper, EM−GC was outfitted with an updated two-layer ocean module that follows similar core equations as the simplified climate model (SCM) emulators used by the authors of the Sixth Assessment Report of the Intergovernmental Panel on Climate Change (IPCC AR6, Sect. 7.SM.2 of Smith et al., (2021a)).

4.2 Data and Methods

4.2.1 Empirical Model of Global Climate

In this section, we provide a brief overview of the EM−GC model, and the datasets used in this study. A more detailed description of EM−GC can be found in Farago et al., (2025) and McBride et al., (2021). For this paper, the energy balance component of the model was updated to the two-layer EBM formulation proposed by Held et al., (2010). We briefly summarize this update in Sect. 4.2.1.1, and provide a more detailed description, including the calibration of the energy balance component of our model in Chapter 3.

EM−GC uses a multiple linear regression (MLR) analysis of the historical climate record (Lean and Rind, 2008, 2009; Zhou and Tung, 2013; Canty et al., 2013; Chylek et al., 2014) between 1850 and 2019 to compute the C_0−C_6 regression coefficients in Eq. (4.1), in a manner that the cost function in Eq. (4.2) is minimized. We refer to this process as the training of the model.

$$\Delta T_{MDL,i} = \Delta T_{ANTH,i} + C_0 + C_1 \times SAOD_{i-6} + C_2 \times TSI_{i-1} + C_3 \times ENSO_{i-2} + C_4 \times AMV_i + C_5 \times PDO_i + C_6 \times IOD_i \quad (4.1)$$

$$Cost\ function = \sum_{i=1}^{N_{MONTHS}} \frac{1}{\sigma_{OBS,i}^2} (\Delta T_{OBS,i} - \Delta T_{MDL,i})^2 \quad (4.2)$$

In Eq. (4.1), ΔT_{ANTH} corresponds to the change in GMST due to anthropogenic activity. This value is computed by the EBM component of our model from the magnitude of time-invariant climate feedback, the ERF of the climate due to GHGs, tropospheric aerosols and land-use change, as well as the export of heat to oceans. The model uses a monthly time grid, with *i* being the indicator of a given month. ΔT_{MDL} and ΔT_{OBS} in Eqs. (4.1) and (4.2) correspond to the modelled, and observed GMST anomaly, respectively; $\sigma_{OBS,i}$ in Eq. (4.2) represents the uncertainty in the observations of GMST. EM−GC considers the natural factors of Stratospheric Aerosol Optical Depth from volcanic eruptions (SAOD), Total Solar Irradiance (TSI), ENSO, Atlantic

Multidecadal Variability (AMV), Pacific Decadal Oscillation (PDO) and Indian Ocean Dipole (IOD) as shown in Eq. (1). SAOD, TSI and ENSO are lagged by 6,1 and 2 months, respectively, following McBride et al., (2021). While we refer to AMV being a natural factor, the AMV is believed to be the result of a combination of internally and externally forced processes (Ting et al., 2009; Zhang et al., 2019b; Deser and Phillips, 2021). This important detail is addressed further in Sect. 4.2.2.5.

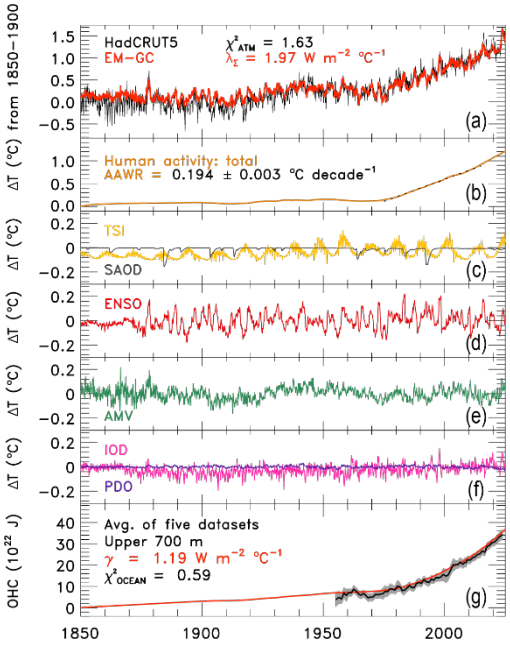

Fig. 4.1: (a) Observed (black) and modelled (red) GMST anomaly, relative to an 1850−1900 baseline. This panel also displays the values of λ_Σ and χ^2_{ATM} (see text). (b) Contribution of anthropogenic activity (ΔT_{anth}, orange) to the modelled GMST. The value of AAWR (see text) and the corresponding 2σ uncertainty of the linear fit is also shown. This uncertainty only considers the goodness of fit between the linear fit and ΔT_{anth}, and does not account for the uncertainty in climate feedback or ERF_{AER}. The uncertainty in climate feedback or ERF_{AER} is accounted for using an ensemble method (see text). (c) Contribution of SAOD (gray) and TSI (gold) to ΔT_{MDL}. (d) Contribution of ENSO to ΔT_{MDL}. (e) Contribution of AMV (green) ΔT_{MDL}. (f) Contribution of IOD (pink) and PDO (purple) to ΔT_{MDL}. (g) Observed OHC in the upper 700 m of global oceans, based on an average of five OHC datasets (black), and modelled OHC (red). This panel also displays the values of γ and χ^2_{OCEAN} (see text). The single ensemble member shown in this figure is obtained from an EM−GC simulation trained between 1850 and 2019, and corresponds to the IPCC AR6 best estimate trajectory of ERF_{AER} from Annex III of AR6 (IPCC, 2021a; Smith et al., 2021b).

Figure 4.1a shows a single modelled fit (red line) to the observed GMST record obtained from version 5 of the Hadley Centre Climatic Research Unit (HadCRUT5, (Morice et al., 2021),

black). Panels b−f show the modelled contributions to the GMST from anthropogenic activity (ΔT_{ANTH} in Eq. (4.1), Fig. 4.1b) and natural variability (Fig. 4.1c−f). The rate of rise in GMST due to anthropogenic activity, termed the Attributable Anthropogenic Warming Rate (AAWR), is computed as the slope of a linear fit to ΔT_{ANTH} between 1975 and 2014 (McBride et al., 2021) and is given in Fig. 4.1b. Fig. 4.1g shows the modelled Ocean Heat Content (OHC) in the upper 700 m of global oceans (red), overlaid with the time series of observed OHC. The observed OHC record (black), and the corresponding uncertainty time series (grey shading in Fig. 4.1g) used here is a composite of five observational OHC datasets, which we describe in Sect. 4.2.2.6. In Fig. 4.1g, we also display the value of the heat transfer parameter (γ, (Geoffroy et al., 2013b)) between the two layers of the EBM component of the model, which we describe in detail in Chapter 3. The single fit shown in Fig. 4.1 assumes a certain value of time-invariant climate feedback (λ_Σ, panel (a)) and a single time series of ERF_{AER} (see caption). The parameter λ_Σ is the sum of all feedbacks (water vapor, lapse rate, clouds, etc.), except for the Planck-feedback (Farago et al., 2025); we describe the mathematical relation of this quantity to the feedback parameter commonly used in two-layer EBMs in Chapter 3.

The uncertainty in the magnitude of climate feedback and ERF_{AER} is considered using an ensemble method (McBride et al., 2021; Farago et al., 2025). For the ensemble, regressions are performed for 160,000 members as described in Sect. 4.2.1.2. Each ensemble member is constrained by the model's ability to reproduce observed GMST and OHC using three reduced chi-square metrics as described in Sect. 4.2.1.2. The values of two of these reduced chi-square indicators (χ^2_{ATM} and χ^2_{OCEAN}) for the single ensemble member shown in Fig. 4.1 are listed on panels (a) and (g).

4.2.1.1 Two−layer Energy Balance Model

In this section, we briefly summarize the updates to the energy balance component of the EM−GC model adapted for this paper, with additional details provided in Chapter 3. To capture the short-term response to a sudden increase of ERF by a constant magnitude (hereafter termed step forcing), we employ the two-layer EBM formulation from Held et al., (2010). The two-layer EBM is sufficiently simple for use in reduced complexity climate models, and provides a temperature response under step forcing scenarios that is consistent with the response of Earth System Models (ESMs) (Gregory et al., 2015; Geoffroy et al., 2013a; Geoffroy et al., 2013b; Tsutsui and Smith, 2025). In this paper, we use the EBM−1 formulation described by Geoffroy et al., (2013b), and associate the temperature of the upper layer in the two-layer EBM with ΔT_{ANTH} in Eq. (4.1). The two-layer EBM approximation was also used extensively by the authors of the IPCC AR6 report (Sect. 7.SM.2 of Smith et al., (2021a)) in emulators calibrated using the output of CMIP6 models. Importantly, while two-layer EBMs are usually calibrated using CMIP model output, we use the observed rise in GMST and OHC for calibration, also described in Chapter 3.

4.2.1.2 Ensemble Method and Probabilistic Forecasts

Here we describe the quantitative manner in which the impact of the uncertainties in the magnitude of climate feedback and ERF_{AER} are evaluated. An ensemble of 160,000 members, comprised of combinations of the time-invariant climate feedback parameter λ_{Σ}, and time series of ERF due to anthropogenic activity is generated and then used in the regression model (McBride et al., 2021; Farago et al., 2025). The time series of the total ERF is expressed from the sum of ERF due to GHGs, the radiative forcing due to land-use change (LUC), and a best estimate time series of ERF_{AER}, scaled with a constant multiplicative factor (s), as shown in Eq. (4.5).

$$ERF\ (t) = \sum ERF_{GHG}\ (t) + s \times ERF_{AER}\ (t) + ERF_{LUC}\ (t) \tag{4.5}$$

We pair 400 different values of λ_Σ with 400 values of the scaling parameter *s*, thereby creating an ensemble of 160,000 members, which accounts for the uncertainties in both the magnitude of climate feedback, and the magnitude of the radiative forcing due to tropospheric aerosols. The time series of ERF (t) in Eq. (4.5) is used as the radiative forcing input to the two-layer EMB component of EM−GC (F in Eq. (3.1)) for each ensemble member. The input time series of ERF_{GHG}, ERF_{AER} and ERF_{LUC} in Eq. (4.5) are based on the time series published in Annex III of the IPCC AR6 report (IPCC, 2021a; Smith et al., 2021b), as described in Sect. 2.2.2.

The EM−GC ensemble is constrained by observed GMST and OHC through the use of three reduced χ^2 indicators, as described in Sect 2.1 of McBride et al., (2021) and Sect. 2.7 of Farago et al., (2025). Only those ensemble members are accepted that satisfy all three reduced χ^2 constraints, defined as the value of each χ^2 indicator being lower than 2. Two of these indicators, χ^2_{ATM} and χ^2_{RECENT}, represent how well the time series of modelled GMST aligns with observed GMST during the entire training period (1850 to 2019) and the recent few decades (1940 to 2019), respectively. The use of χ^2_{RECENT} as a constraint ensures that all accepted ensemble members succeed in capturing the rapid rise of GMST due to anthropogenic activity since the 1940s. The third indicator, termed χ^2_{OCEAN}, quantifies how well the modelled OHC compares to the observed OHC data. After the application of the observational constraints, the ensemble members are weighted by the magnitude of ERF_{AER} using an asymmetrical Gaussian function that is centered around the IPCC AR6 best estimate of −1.1 W m^{-2} for the value of ERF_{AER} in 2019 relative to 1750 (Farago et al., 2025). This weighted ensemble is then used to provide a probabilistic forecast of the GMST between 2020 and 2025, which we then compare to the observed GMST anomalies in Sect. 4.3.2 and 4.3.3.

4.2.2 Data and Model Input

4.2.2.1 Temperature Records

Throughout this paper, we use the HadCRUT5 GMST record (Morice et al., 2021) between 1850−2019 for the training of EM−GC, and for comparison with modelled GMST anomalies from 2020 to 2024. All values of the GMST anomaly, denoted ΔT, are with respect to a pre-industrial baseline (1850 to 1900).

4.2.2.2 Effective Radiative Forcing

We use ERF as defined in Chapter 7 of AR6 (Forster et al., 2021a) to compute the influence of GHGs and tropospheric aerosols on ΔT. The ERF due to GHGs is the sum of ERF due to CO_2, CH_4, N_2O, halogenated compounds, tropospheric ozone (O_3) and stratospheric water vapor from the oxidation of methane, obtained from Annex III of AR6 and the corresponding data repository (IPCC, 2021a; Smith et al., 2021b). These time series, provided on an annual time grid, are interpolated to a monthly grid for use as inputs to the EM−GC.

Between 2020 and the end of 2024, we use the global concentrations of CO_2, CH_4 and N_2O, inferred from the measurements obtained at a globally distributed network of air sampling sites and averaged by the NOAA Global Monitoring Laboratory (GML) (Lan et al., 2024a; Lan et al., 2024b). Here and throughout, we refer to these time series as NOAA-GML global GHG concentrations. The NOAA-GML GHG concentrations are converted to ERF using the formulations and tropospheric adjustments described in the Supplement of Chapter 7 of AR6 (Smith et al., 2021a). For the ERF of halogenated compounds and tropospheric ozone, we use the SSP2−4.5 ERF trajectories from 2020 onwards from Annex III of AR6 (IPCC, 2021a; Smith et al., 2021b). The ERF due to stratospheric water vapor from the oxidation of methane is a linear function of ERF_{CH4} (IPCC, 2021a), which we compute by scaling the NOAA-GML based ERF_{CH4}

with a scaling value of 9.19% following Farago et al., (2025). The ERF due to stratospheric water vapor described in this section does not account for the abrupt injection of water vapor from volcanic eruptions, such as the eruption of the Hunga in 2022. We address the inclusion of the eruption of Hunga in Sect 4.2.2.4.

We compute the total ERF due to tropospheric aerosols (ERF_{AER} in Eq. (4.5)) between 1850 and 2019 by summing the ERF time series of the direct (ERF_{ARI}) and indirect effects (ERF_{ACI}) from Annex III of AR6 (IPCC, 2021a; Smith et al., 2021b). Between 2020 and the end of 2024, we use the sum of the direct and indirect effects under an SSP2−4.5 scenario (O'Neill et al., 2016) as the baseline trajectory for ERF_{AER}. This baseline trajectory is used as a reference scenario, where the IMO2020 regulations are assumed to have had no impact on ERF_{AER}. To simulate the effects of the IMO regulations on global ERF_{AER}, we create two alternative time series, where values of +0.1 W m^{-2} and +0.15 W m^{-2} are added to this baseline trajectory, as immediate step-forcing adjustments starting in January 2020. We refer to these three scenarios as Reference, IMO−0.1, and IMO−0.15 and the increase in global ERF due to IMO2020 as ΔERF_{IMO}. We use the SSP2−4.5 scenario as the baseline for ERF_{AER}, similar to Gettelman et al. (2024) and Jordan and Henry (2024), because this SSP scenario is the one that is most consistent with recent trends in anthropogenic emissions of GHGs and aerosols (Meinshausen et al., 2024). The values of +0.1 W m^{-2} and +0.15 W m^{-2} for ΔERF_{IMO} were chosen based on recently published estimates of the increase in global radiative forcing due to the introduction of the IMO regulations (Table A1 in Jordan and Henry (2024)).

4.2.2.3 El-Niño Southern Oscillation, Indian Ocean Dipole and Pacific Decadal Oscillation

We use Version 2 of the Multivariate ENSO Index (MEI.v2) (Wolter and Timlin, 1993; Zhang et al., 2019a) to characterize the influence of ENSO on GMST. This index starts in 1979,

and extends to the end of 2024. Between 1850 and 1978, a historical extension based on Wolter and Timlin (2011) and the HadSST3 dataset (Kennedy et al., 2011) is used, following Sect. 2.2.6 of McBride et al., (2021).

The NOAA Dipole Mode Index (DMI) (Saji and Yamagata, 2003) time series, which spans from 1870 to 2024, is used as model input for the IOD. For 1850 to 1870, we use the 1º x 1º Sea Surface Temperatures (SSTs) from the Centennial in situ Observation-Based Estimate (COBE) (Ishii et al., 2005) to compute the time series of the difference in SSTs between the western equatorial Indian Ocean (50−70º E and 10º S – 10º N) and southeastern equatorial Indian Ocean (90−110º E and 10º S − 0º N). This formulation of IOD is consistent with the methods used to compute the NOAA DMI index. The resulting time series is treated as the IOD index between 1850 and 1870, and is appended to the NOAA DMI time series to obtain an IOD index between 1850 and the end of 2024.

The PDO input for EM−GC is based on a time series provided by NOAA at https://psl.noaa.gov/pdo/ (Mantua et al., 1997; Newman et al., 2016). NOAA provides multiple PDO indices, based on the HadISST1.1, COBE2, and ERSST V5 SST datasets, respectively, as well as an index constructed from the combination of these three SST datasets, which we will refer to as the NOAA Ensemble PDO Index. The individual PDO indices provided by NOAA differ in their first year of data availability. We use the NOAA Ensemble PDO index, which covers 1870 to December 2024, appended to the NOAA COBE2 PDO index for 1850 to 1870. We chose the COBE2-based index for this purpose, as this was the only PDO index from NOAA that provides data as early as 1850.

4.2.2.4 Total Solar Irradiance and Volcanic Activity

The 11-year solar cycle has a small, but noticeable influence on simulated GMST (McBride et al., 2021). In this paper, we use the NOAA Climate Data Record (CDR) composite observational TSI record (Coddington et al., 2024), which provides daily observed TSI data starting in late 1978. We use this time series between 1979 and the end of 2024 to create a time series of monthly average TSI, which we append to the CMIP6 TSI input time series from Matthes et al., (2017), that covers 1850 to 1978. The resulting TSI time series, which covers the 1850 to 2024 period, is then converted to anomalies by subtracting the long-term average from the time series of absolute TSI (McBride et al., 2021).

Next, we describe the construction of our SAOD input that corresponds to volcanic eruptions, and the inclusion of the eruption of Hunga in our simulations. We use the time series of SAOD at 550 nm, obtained from the Global Space-based Stratospheric Aerosol Climatology (GloSSAC v2.0) (Thomason et al., 2018) between 1979 and the end of 2023, to compute a globally averaged time series of SAOD, using cosine-latitude weighting from 80º S to 80º N. For the year 2024, we use the globally averaged SAOD value from December 2023. To obtain a time series of SAOD between 1850 to 1978, we use the 550 nm extinction coefficients from 80º S to 80º N from the Volcanic Forcing Dataset (Arfeuille et al., 2014) made for CMIP6 GCM runs. The 550 nm extinction coefficients are integrated from the tropopause to 39.5 km, then weighted by the cosine of latitude from 80º S to 80º N to obtain a time series of globally averaged SAOD from 1850 to 1978. This time series is then combined with the GloSSAC-based time series of SAOD, which covers the 1979 to 2024 period, to obtain the model input time series for SAOD between 1850 and 2024.

The eruption of the Hunga in January 2022 injected a large amount of water vapor into the stratosphere (Millán et al., 2022; Vömel et al., 2022; Randel et al., 2024; Evan et al., 2023), raising questions about whether the warming effect due to the injection of stratospheric water vapor is greater than the cooling effect from SAOD. Studies differ in their conclusions as to whether the net effect of the Hunga eruption was a warming (Jenkins et al., 2023; Millán et al., 2022) or cooling (Schoeberl et al., 2023; Schoeberl et al., 2024; Gupta et al., 2025) of the climate. However, studies generally agree that the magnitude of the change in GMST due to the eruption of the Hunga Ha'apai is on the scale of 10^{-2} ºC (Jenkins et al., 2023; Schoeberl et al., 2023). EM−GC simulations do not explicitly account for the injection of water vapor to the stratosphere from volcanic eruptions. Given that the net effect of the eruption of Hunga on GMST is small, we chose to use SAOD as a proxy for the impact of the Hunga Ha'apai on GMST, while neglecting the additional radiative forcing from the injection of stratospheric water vapor. This representation, while simplified, results in a cooling of −0.024 ºC and −0.027 ºC due to SAOD in the years of 2022 and 2023, respectively (see Sect. 3.2 for additional details). Consequently, our SAOD-based proxy for the eruption of Hunga Ha'apai produces a small net cooling effect, similar to the estimates presented in Schoeberl et al., (2023).

4.2.2.5 Atlantic Multidecadal Variability

The variations in SSTs in the North Atlantic due to the Atlantic Multidecadal Variability (AMV) have a well-documented influence on the GMST (e.g. Schlesinger and Ramankutty (1994), Canty et al., (2013) and Sect. 4.6 of Zhang et al., (2019b)). We use the term AMV, rather than Atlantic Multidecadal Oscillation (AMO), as the term AMV is believed to be more appropriate when describing the multidecadal fluctuations in the Atlantic (Sect. 1 of Zhang et al., (2019b)). How internal processes and external radiative forcing affect AMV is a topic of extensive debate

(Zhang et al., 2019b; Qin et al., 2020; Deser and Phillips, 2021). AMV is believed to be driven by a combination of internal processes, such as the Atlantic Meridional Overturning Circulation (AMOC) (Zhang et al., 2019b), and external forcings, such as from tropospheric aerosols (Booth et al., 2012).

AMV indices are traditionally obtained by the detrending and subsequent low-pass filtering of the spatially averaged North Atlantic SST anomalies. Several detrending methods have been proposed (Zhang et al., 2019b), but most commonly, the detrending is done using the time series of global-mean SSTs (Trenberth and Shea, 2006) or a linear function (Enfield et al., 2001), though both methods carry certain disadvantages (e.g. Sect. 3.2.3 of Canty et al. (2013)). Therefore, following Canty et al., (2013), we detrend the area-weighted monthly mean North Atlantic SSTs between the equator and 60 ºN, which are based on the HadSST4 dataset (Kennedy et al., 2019), using the magnitude of global anthropogenic radiative forcing. We treat the resulting index as our AMV input, and use this input for the simulations presented in Sect. 4.3.2. We also create an alternative AMV index, where the high-frequency component of our original AMV index is removed using a Fourier-filter, which restricts frequencies higher than 1/9 yr^{-1} (Canty et al., 2013). We will refer to this second AMV dataset as our Fourier-filtered AMV input, and present simulations that use this input dataset in Sect. 4.3.3.

4.2.2.6 Ocean Heat Content

EM−GC simulations quantitatively account for the export of heat to Earth's oceans, and the ability of ensemble members to reproduce the observed rise in OHC is one of the observational constraints within the model (Sect. 4.2.1.2). In this paper, we use a composite OHC time series, which covers the 1955 to 2024 period, created using an average of five different OHC anomaly records (Levitus et al., 2012; Balmaseda et al., 2013; Ishii et al., 2017; Carton et al., 2018; Cheng

et al., 2024). The time series for the uncertainty in the observed OHC is based on the 1σ uncertainty computed from the five datasets. The individual OHC time series, the average of the five datasets, and the corresponding uncertainty time series are shown in Fig. 4C.1. Additional details on the construction of the composite OHC dataset are provided in our Appendix C.

4.3 Results

4.3.1 Long-term warming trends

The primary purpose of our paper is to analyze why the years 2023 and 2024 experienced much higher GMST anomalies relative prior years, such as 2021 or 2022. However, the long-term warming impact of rising GHG emissions serves as an important backdrop. Therefore, we begin by analyzing the long-term warming of the global temperature due to anthropogenic activity. To quantify the rise in GMST due to anthropogenic activity in recent decades, we use the quantity AAWR, which is computed as the slope of a linear fit to the anthropogenic component of the modelled GMST (Sect. 4.2.1) between 1975 and 2014. Figure 4.2b−c show AAWR as the function of climate feedback (vertical axis) and the magnitude of ERF_{AER} (horizontal axis). Colors correspond to values of AAWR, as indicated by the color bars to the right, and are shown only for combinations of ERF_{AER} and λ_{Σ} for which the reconstructed GMST and OHC satisfy the three reduced χ^2 observational constraints over the training period (1850 to 2019). Panels (b) and (c) differ in that, for the simulation shown in Fig. 4.2b, the high frequency component of the AMV input time series, that is frequencies greater than 1/9 yr^{-1}, was removed using a Fourier-filter (Sect. 4.2.2.5). Figure 4.2a shows the asymmetrical Gaussian function that is used to weight the ensemble (Sect. 4.2.1.2). The center point, as well as the 1σ and 2σ boundaries of this Gaussian function, are based on the best estimate and likely range for ERF_{AER} in 2019 provided by the IPCC AR6 report.

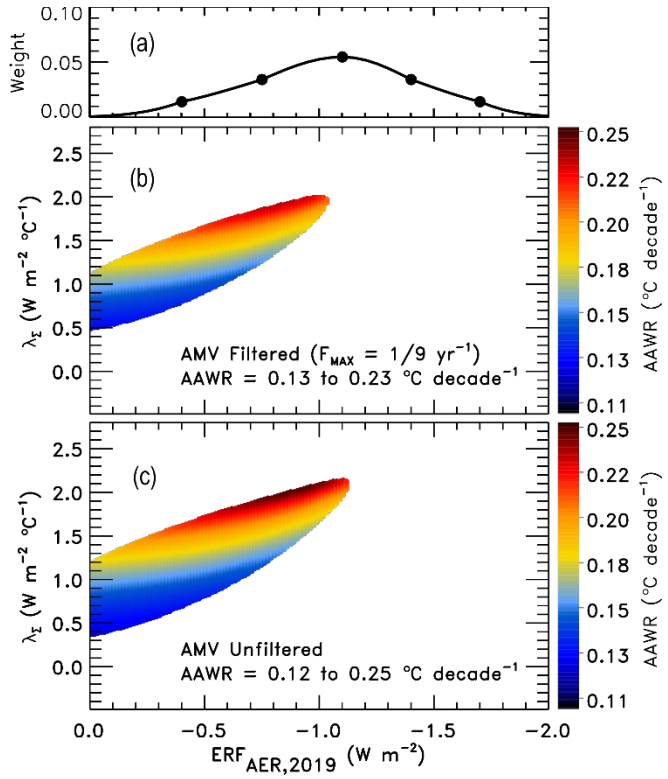

Figure 4.2: Aerosol weighting method, and computed values of AAWR for the EM−GC ensemble. (a): Asymmetrical Gaussian function used to weight the ensemble. The points marked on the Gaussian represent the center point, the 1σ and 2σ boundaries of the Gaussian (see Sect. 2.7 and Table S3 of Farago et al., (2025)). (b) Values of AAWR as the function of λ_Σ and $ERF_{AER,2019}$. Colors denote specific values of AAWR as indicated by the color bar on the right. AAWR is only shown for those combinations of λ_Σ and $ERF_{AER,2019}$, where all three χ^2 observational constraints are satisfied. The AMV input of the simulation used to produce this panel has been Fourier-filtered to remove frequencies greater than 1/9 yr^{-1} (see text). (c) As in (b), but without a Fourier-filter having been applied to the AMV input.

The reconstruction of GMST and OHC over the training period is largely unaffected by the removal of the high-frequency component of the AMV input. As shown in Fig. (4.2b) and (4.2c), the range of AAWR is similar between the two sets of simulations. Further, the weighted central estimate and 5−95% range for AAWR is 0.19 ºC decade^{-1} [0.14 to 0.23 ºC decade^{-1}], and 0.19 ºC decade^{-1} [0.15 to 0.22 ºC decade^{-1}] for the simulations where the AMV input was unfiltered and Fourier-filtered, respectively. Similarly, EffCS is also consistent between these two sets of simulations (Fig. 4C.2). Our estimates of AAWR, based on the 1975 to 2014 period, are generally consistent with Samset et al., (2023), who found the rate of warming to be 0.19 ºC decade^{-1}

between 1971 and 2020 using the HadCRUT5 dataset, with an acceleration in the rate of warming starting in 1990s. The values of AAWR shown here imply that a sizeable portion of the rise in GMST in the recent few years can be explained with the continued trend of anthropogenic GHG emissions. For example, the rate of 0.19 ºC decade^{-1} corresponds to an increase in GMST of about 0.1 ºC in 2024 relative to 2019. As a comparison, Gettelman et al., (2024) suggested that the IMO2020 regulations increase global temperatures by about 0.04 ºC and 0.08 ºC by 2023 and 2030, respectively, relative to 2020. Therefore, the change in GMST due to the IMO2020 regulations would correspond to only a few years of continued anthropogenic activity at the 1975 to 2014 rates. A similar comparison can be drawn with Jordan and Henry (2024), who found that IMO2020 increases global surface temperature by 0.046 ºC in the 2020−29 period, and concluded that temperature impact of IMO2020 corresponds to about 2−3 years' worth of continued global warming.

4.3.2 Natural and anthropogenic contributions to temperature anomalies in 2023 and 2024

Next, we quantify the contribution of various natural and anthropogenic factors to the GMST over the past half-decade. Figure 4.3 shows the modelled GMST for the Reference (left), IMO−0.1 (middle) and IMO−0.15 (right) simulations. The top panels of each column show the observed GMST anomaly from the HadCRUT5 dataset (black) and the EM−GC simulated range. Colors denote the EM−GC simulated probability of the GMST being greater or equal than a given value at a time, as indicated by the color bar to the right. Panels (d−f) show the simulated rise in GMST due to IMO2020, based on global energy balance. Panels (g−r) show the simulated contributions of natural variability to the GMST, computed based on observed climate indices (Sect. 4.2.1 and 4.2.2). We will refer to these contributions shown in Fig. 4.3g−r as *natural*, with

the understanding that some of these processes, and hence the corresponding climate indices, may have been influenced by external anthropogenic factors, including possibly even IMO2020.

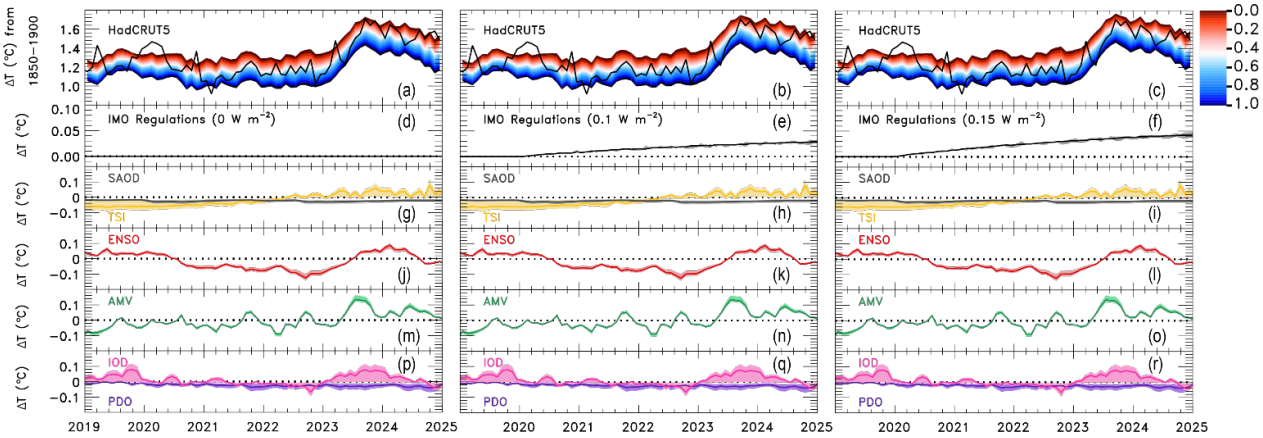

Figure 4.3: Probabilistic simulation of GMST and the contributions of various factors to GMST for the Reference (left), IMO−0.1 (middle) and IMO−0.15 (right) scenarios. Panels (a−c) show the EM−GC simulated GMST, with colors denoting the probability of the GMST being a given value, or greater, as indicated by the color bar on the right. The black line is the observed GMST from the HadCRUT5 dataset. All GMST anomalies are with respect to an 1850−1900 pre-industrial baseline. (d−f) Contribution of IMO2020 to the GMST anomaly based on global energy balance. (g−r): Contribution of natural factors (see text) to GMST. On panels (d−r), the solid line is the EM−GC median estimate (which we define as the 50% probability), while the shading corresponds to the 5−95% uncertainty range.

The IMO2020 regulations are found to have increased GMST by 0.028 ºC [0.027 ºC to 0.031 ºC, 5−95% range] and 0.043 ºC [0.038 ºC to 0.048 ºC] by the end of 2024 for the IMO−0.1 and IMO−0.15 scenarios, respectively. We refer to these quantities as ΔT_{IMO}, and we term this computed warming as being due to global energy balance, since these values have been computed using the two-layer EBM component of our model. As noted above, additional localized effects from IMO2020 may be blended into the observed climate indices, upon which the contributions to changes in GMST shown in Fig. 4.3c−f are based. We briefly address this topic in Sect. 4.3.3.

Table 4.1 summarizes our estimates of ΔT_{IMO} in response to a given change in global radiative forcing due to IMO2020 (ΔERF_{IMO}). Our estimates of ΔT_{IMO} of 0.028 ºC [0.027 ºC to 0.031 ºC, 5−95% range] and 0.043 ºC [0.038 ºC to 0.048 ºC] under the IMO−0.1 and IMO−0.15 scenarios, respectively, are consistent with values ΔT_{IMO} obtained both from EBMs (Gettelman et

al., 2024) and ESMs (Jordan and Henry, 2024; Yoshioka et al., 2024; Watson-Parris et al., 2024). Studies provide estimates of ΔT_{IMO} over different time periods, which we specify in Table 4.1. Our values of ΔT_{IMO} compare well to most estimates presented in Table 4.1. While the EBM-based estimates of Gettelman et al., (2024) were obtained using an EBM calibrated on CMIP6 model output, our results are based on an EBM trained on observational datasets. There are two studies that provide values of ΔT_{IMO} considerably larger than our estimates. Quaglia and Visioni (2024) estimate ΔT_{IMO} to be about 0.08 ºC, a factor of 2 greater than our IMO−0.15 values. They also found significant warming in the North Atlantic, highlighting that localized effects of IMO2020 may be substantial. As noted above, a portion of the localized effects may be blended into the observational datasets that are used as our inputs. Consequently, the contributions of these localized effects to GMST, particularly for the North Atlantic, are not attributed to IMO2020 in the simulations presented in Fig. 4.3 and summarized in Table 4.1. Finally, as highlighted by Watson-Parris et al, (2024), the estimate of ΔERF_{IMO} provided in Yuan et al., (2024) is reported only over the global oceans. Consequently, global values of ΔERF_{IMO} and ΔT_{IMO} would be lower than those presented in Yuan et al., (2024). In Table 4.1 we therefore show both the original values presented in Yuan et al., (2024) as well as the adjusted estimates provided by Watson-Parris et al., (2024). The estimates of ΔT_{IMO} provided by Yuan et al., (2024) nevertheless remain considerably higher than the values presented in our paper, as well as those in several other studies.

Table 4.1: Estimates of the change in global radiative forcing due to IMO2020 (ΔERF_{IMO}), and the corresponding change in global surface temperature (ΔT_{IMO}). For Yuan et al., (2024), we present the non-global values as published in their paper, as well as the globally scaled values (italic) suggested by Watson-Parris et al., (2024).

	Method	Model	ΔERF_{IMO} (W m^{-2})	Timeframe	ΔT_{IMO} (ºC)
Quaglia and Visioni (2024)	ESM	CESM2	0.14	2030	0.08
Yoshioka et al., (2024)		HadGEM3-GC3.1-LL	0.13	2020−49	0.04
Watson-Parris et al., (2024)		CESM2	N/A	2020−40	0.03
Jordan and Henry (2024)		UKESM1	0.14	2020−29	0.046
Yuan et al., (2024) *Yuan et al., (2024), adjusted*	EBM	One-layer EBM	0.2 *0.14*	7 years	0.16 *0.06 to 0.10*
Gettelman et al., (2024)		FAIR v2.1.0	0.12	2023	0.04
This Study: IMO−0.1		**EM−GC**	**0.1**	**2024**	**0.028**
This Study: IMO−0.15			**0.15**	**2024**	**0.043**

Next, we quantify the contributions of various natural factors to GMST. We show the modelled contribution of ENSO to the GMST between 2019 and the end of 2024 in Fig. 4.3j−*l*. We find that the annual mean GMST in 2023 and 2024 increased by about 0.08 ºC and 0.10 ºC respectively, relative to 2022, as a consequence of a shift from La Niña to El Niño (Fig. 4.3j−*l*). The difference between the annual mean GMST anomaly in 2022 and 2023 is about 0.3 ºC in the HadCRUT5 dataset. Therefore, about one third of the difference in GMST between 2022 and 2023 can be explained with the shift from La Niña to El Niño. Our results align well with the estimates of Goessling et al., (2025), who found that the onset of El Niño contributed about 0.07 ºC to the temperature anomaly in 2023. Estimates for the contribution of ENSO to the 2023 and 2024 temperature anomalies were also provided by the *State of the Global Climate 2024* report of the World Meteorological Organization (WMO) (WMO, 2025), hereafter WMO24. Using linear regression to the Niño 3.4 index, WMO24 found that annual temperatures rose by about 0.08 ºC

in 2023 relative to 2022 due to ENSO (see their Datasets and methods section), which aligns exceptionally well with our estimate of 0.08 ºC for this period. However, WMO24 suggests that an additional increase of 0.12 ºC in the annual global mean temperature between 2023 and 2024 can also be attributed to ENSO. We find the increase of GMST due to ENSO between 2023 and 2024 to be only 0.02 ºC, which is much lower than the WMO24 estimate. Raghuraman et al. (2024) suggested that prolonged La Niña events may lead to sudden changes in the GMST of 0.25 ºC or greater during the subsequent El Niño event, based on the analysis of several CMIP models. Conversely, our results do not indicate the occurrence of an ENSO-driven spike in GMST of the magnitude suggested in Raghuraman et al., (2024).

Starting in January 2023, a positive IOD event was also found to have influenced GMST (Fig. 4.3f). This IOD event contributed 0.047 ºC [−0.003 ºC to 0.071 ºC, 5−95% range] to the annual mean GMST in 2023, and corresponds to a rise in GMST of 0.072 ºC [0.032 ºC to 0.078 ºC] in 2023, relative to 2022. This positive IOD event persisted into early 2024, and gradually shifted to a negative phase by the end of 2024, resulting in a contribution to the annual mean GMST of 0.008 ºC [−0.015 to 0.024 ºC] in 2024. In 2024, the contribution of IOD to the annual mean GMST decreased by 0.039 ºC [0.012 to 0.047 ºC], relative to 2023. Xie et al. (2025) suggested that while the co-occurrence Extreme Positive IOD (EXpIOD) events, such as the one observed in 2023, may be coincidental with the onset of El Niño, co-occurring El Niño and positive IOD events result in the amplification of the intensity of IOD. Since the 1980s, EXpIOD events have occurred in 1994, 1997, 2006, 2019 and 2023 (Xie et al., 2025). We find however, that based on the NOAA DMI index, the 2023 EXpIOD was the longest of all of these events. Our computation of the increase in GMST of 0.072 ºC from 2022 to 2023 due to IOD is comparable in magnitude to ENSO's impact on the GMST between these two years (0.08 ºC).

Increased TSI due to the 11-year solar cycle also contributed to the observed rise in GMST in 2023 and 2024, relative to 2022 (Fig. 4.3g–i). The increase in TSI is found to have contributed 0.028 ºC [0.001 ºC to 0.044 ºC, 5–95% range] and 0.032 ºC [0.002 ºC to 0.049 ºC] to the annual mean GMST in 2023 and 2024, respectively. Our estimates for the impact of TSI on GMST are generally consistent with, albeit on the lower end of those of WMO24, who found the contribution of the changes in the solar cycle to GMST to be about 0.04 ºC [0.015 to 0.065 ºC, 95% confidence] and 0.07 ºC [0.045 to 0.095 ºC] in 2023 and 2024, respectively. Our central estimate of the contribution of TSI to GMST (0.028 ºC) in 2023 aligns exceptionally well with the estimate of 0.027 ºC found by Goessling et al., (2025), though we find a wider range of uncertainty at [0.001 ºC to 0.044 ºC, 5–95% range] in contrast to their range of [0.022 to 0.032 ºC, 90% confidence].

The contributions of SAOD and PDO to the GMST anomalies in 2023 and 2024 are found to be small relative to ENSO and IOD (Fig. 4.3g–i and Fig. 4.3p–r). The median estimates of the contribution of PDO to the modelled GMST are −0.027 ºC, −0.028 ºC and −0.030 ºC for the years 2022, 2023 and 2024, respectively. SAOD is found to be responsible for a slight cooling effect of −0.024 ºC, −0.027 ºC and −0.022 ºC in 2022, 2023 and 2024, respectively. As described in Sect. 4.2.2.4, for the simulations presented in this paper, we neglected the injection of water vapor into the stratosphere from the eruption of Hunga. Nevertheless, our SAOD-based proxy for volcanic activity leads to an estimated −0.027 ºC cooling in 2023, in line with the values of −0.02 ºC [−0.01 ºC to −0.03 ºC] presented in WMO24. Therefore, the neglect of the injection of water vapor from Hunga appears to have no major consequence on our results.

4.3.3 North Atlantic warming

We now discuss the contribution of AMV and North Atlantic SST anomalies to the GMST in 2023 and 2024 (Fig. 4.3m–o). Multiple recent studies have highlighted the unusually high SST

anomalies in the North Atlantic (Kuhlbrodt et al., 2024; Carton et al., 2025), alongside reduced low-cloud cover in the region during 2023 (Goessling et al., 2025). Gettelman et al., (2024) suggested that the resulting increase in local temperatures due to IMO2020 may be much greater than implied by the EBM-based global values, particularly in the Northern Hemisphere mid-latitude oceans. Similarly, Quaglia and Visioni (2024) found a considerable rise in the surface air temperature in the North Atlantic due to IMO2020. While a global EBM, such as our EM−GC cannot directly be used to study localized temperature anomalies, a few key conclusions can still be drawn, as described below.

The variability in North Atlantic SSTs is represented by our AMV index, which we obtained by detrending the time series area weighted North Atlantic SSTs with the magnitude of global anthropogenic ERF (Sect. 4.2.2.5). The contribution of AMV to GMST has shown a steady increase since 2019, with a particularly large contribution in the second half of 2023 (Fig. 4.3m−o). AMV is found to have contributed 0.048 ºC [0.040 ºC to 0.062 ºC, 5−95% range] and 0.048 ºC [0.041 ºC to 0.059 ºC] to the annual mean GMST in 2023 and 2024, respectively. The modelled contribution of AMV to the GMST anomaly in 2022 is −0.024 ºC [−0.018 ºC to −0.032 ºC]. Consequently, an increase in GMST of about 0.072 ºC from 2022 to 2023 is attributed to AMV in our model framework, which is on the scale of the ENSO and IOD-related rise in GMST between the same two years.

The peak in our AMV index (and therefore, the contribution of this proxy to GMST in Fig. 4.3m−o) in mid-late 2023 is consistent with the record high observed North Atlantic SSTs in 2023 (Carton et al., 2025). Samset et al., (2024) also found that conditions in the North Atlantic contribute strongly to the global temperatures in 2023, using a Green's function-based method. They estimated that SSTs in the tropical and subtropical North Atlantic contribute about 0.04 ºC

and 0.02 ºC to the annual mean global surface temperature anomaly in 2023. These values are generally in line with our estimates derived from the AMV index noted in the prior paragraph.

Next, we analyze whether the substantial contributions from AMV in our simulations originate from long-term trends, or short-term variability. We perform the same analysis that was shown in Sect. 4.3.2 with a second set of simulations, where the high-frequency component of the AMV index, that is, frequencies greater than 1/9 yr^{-1}, is removed using a Fourier filter (Sect. 4.2.2.5). The regression to the historical GMST and OHC during the model training period of 1850 to 2019 is largely unaffected by the choice of AMV input (Sect. 4.3.1). Figure 4.4 shows the EM−GC simulations that use a Fourier-filtered AMV input for the Reference, IMO−0.1 and IMO−0.15 scenarios in a manner similar to Fig. 4.3. The contributions of all factors to the GMST shown in Fig. 4.4g−r are highly similar to those in Fig. 4.3g−r, except for the contributions of AMV. The contribution of AMV to the annual mean GMST is found to be 0.009 ºC [0.008 ºC to 0.010 ºC] higher in 2023 relative to 2022, due to a slow rising trend in the AMV index (Fig. 4.4m−o). This value, however, is eight times smaller than that quantified from simulations where the AMV input was not Fourier-filtered. Further, the simulated GMST shown in Fig. 4.4a−c is lower than the observations in mid-late 2023 and late 2024. For both of these time periods, there is a substantial contribution to GMST from AMV when the AMV index has not been Fourier-filtered (Fig. 4.3m−o), which is absent in simulations that use Fourier-filtered AMV input (Fig. 4.4m−o). Consequently, our simulations imply that short-term variability in the North Atlantic SSTs was likely a strong contributor to the observed GMST anomalies in late 2023 and 2024.

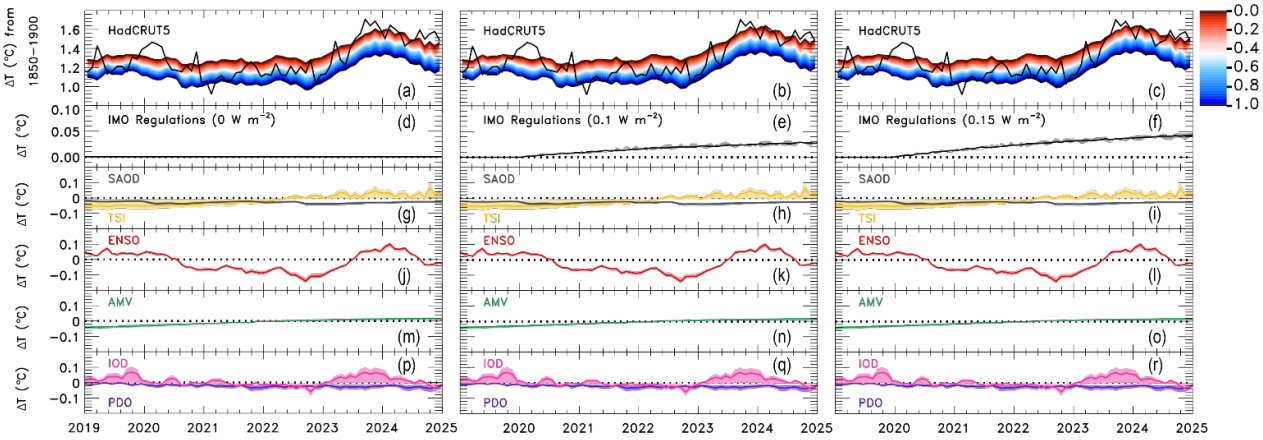

Figure 4.4: Probabilistic simulation of GMST and the contribution of various factors for the Reference (left), IMO−0.1 (middle) and IMO−0.15 (right) scenarios. As in Fig. (4.3), except that the input time series for AMV has been Fourier-filtered to remove frequencies greater than 1/9 yr^{-1} (see text).

Establishing a connection between the high North Atlantic SSTs and the IMO2020 regulations remains challenging. In our model framework, we detrended the AMV index using the time series of global anthropogenic radiative forcing. Local anomalies in ERF that exceed the global values would result in parts of the AMV index carrying an additional, localized anthropogenic component. Consequently, localized effects of IMO2020 may be blended into the AMV index, which would correspond to the impact of IMO2020 on GMST to be greater than implied solely by the global energy balance approach. If we assume that the short-term variability in North Atlantic SSTs described above is driven primarily by IMO2020, than an additional 0.06 ºC in the increase in GMST from 2022 to 2023 can be attributed to IMO2020, which result in estimates of ΔT_{IMO} that align quite well with those of Quaglia and Visioni (2024) (Table 4.1).

Watson-Parris et al., (2024) reported that IMO2020 produces a pattern of North Atlantic SSTs that is similar to those observed in 2023 in CESM2, but only after about 20 years, and no significant warming in this region is simulated between 2020 and 2025. This result contradicts Quaglia and Visioni (2024), who found notable warming in the North Atlantic over the 2021−23 period with the CESM2 model. As highlighted in Watson-Parris et al., (2024), the experimental setup and

framing of results accounts for some of the differences between ESM-based results that investigate the effects of IMO regulations. Jordan and Henry (2024) report lower cloud albedo in the North Atlantic due to IMO2020, which aligns with the observed albedo described in Goessling et al., (2025). Consequently, Jordan and Henry (2024) suggest that the increase in ERF due to IMO2020 is about 2.5 times greater in the North Atlantic region than the value of the global mean. Meanwhile, Carton et al., (2025) attributed the record high SSTs to a combination of increased downwelling radiation, as well as reduced latent and sensible heat loss due to lower trade wind speeds. Carton et al., (2025) also highlighted that the temperature of the North Atlantic mixed layer was already high in March 2023, and therefore, that the mixed layer was preconditioned to be unusually warm. Overall, studies vary in their estimates of how much of the warming in the North Atlantic region is directly attributable to the IMO2020 regulations. Our results suggest that short-term variability in the North Atlantic SSTs was responsible for a portion of the observed rise in GMST between 2022 and 2023, but whether this variability was influenced substantially by the IMO2020 regulations remains unclear.

4.4 Conclusions

Several factors may have contributed to the observed temperatures exceeding expectations in 2023 and 2024. In this paper, we use a multiple linear regression energy balance model (EM−GC) to quantify the influence of various natural and anthropogenic factors on the GMST in these years, including the reduction of sulfate emissions from international shipping starting in 2020. Our model is trained on 170 years of historical GMST data and 65 years of OHC measurements, and uses observed climate indices to simulate the impact of internal variability on GMST, thereby providing a quantification of warming due to various natural and anthropogenic factors. Therefore, our simulations provide observation-driven projections of the GMST anomaly

in 2023 and 2024, and serve as a complementary modelling effort to simulations performed with ESMs, as well as EBMs calibrated using CMIP model output.

We find that the IMO2020 regulations are responsible for an increase in GMST (ΔT_{IMO}) of 0.028 ºC [0.027 ºC to 0.031 ºC, 5−95% range] and 0.043 ºC [0.038 ºC to 0.048 ºC] from the start of 2020 to the end of 2024, for increases in ERF due to IMO2020 of +0.1 and +0.15 W m^{-2}, respectively. These values of ΔT_{IMO} are in line with several other recent estimates.

We also find that GMST increased by about 0.08 ºC from 2022 to 2023 due to the shift from La Niña to El Niño conditions, which explains about one third of the observed rise in GMST between these two years. An additional increase in the annual mean GMST of 0.072 ºC from 2022 to 2023 can be attributed to a strong positive IOD event, which spanned the entire year of 2023. Further, about 0.072 ºC of the rise in GMST from 2022 to 2023 is attributed to AMV; this value is considerably lower, only 0.009 ºC, when the high-frequency component of the AMV index is removed. We find that the removal of the high-frequency component of the AMV index leads to an underrepresentation of GMST in mid-late 2023 and late 2024, which suggests that short-term variability in the North Atlantic SSTs may have been a significant factor that influenced the GMST anomalies observed in 2023 and 2024. Whether these changes in North Atlantic SSTs are a direct result of the introduction of the IMO2020 regulations remains unclear; better understanding of the internal and external drivers of North Atlantic SSTs is required to make a definitive attribution. Finally, the rise in GMST attributable to IMO regulations likely corresponds to only a few years of global warming based on recent trends. Therefore, the anthropogenic emissions of GHGs remain the primary cause of the continued rise of GMST.

Appendix C

Section 4.2.2.6 states that "the time series for the uncertainty in the observed OHC is based on the 1σ uncertainty computed from the five datasets". Using five OHC anomaly records (Levitus et al., 2012; Balmaseda et al., 2013; Ishii et al., 2017; Carton et al., 2018; Cheng et al., 2024), we compute an annual average OHC anomaly time series for the 1955 – 2024 period, which we then normalize to 1989. The year 1989 was chosen for this purpose, as this is the midway point of the 1955 to 2024 period. To obtain an uncertainty time series for our average OHC dataset, we use the 1σ standard deviation, computed from the five OHC datasets, at a given time, or the value of the average standard deviation across the 1955 – 2024 time period, whichever the greater. The average standard deviation between 1955 – 2024 is computed from the time series of the 1σ standard deviations. From this average, we exclude the years 1988 to 1990, as these years have low values of standard deviation due to the OHC anomalies having been normalized to 1989. The use of the long-term mean uncertainty to construct the OHC uncertainty time series eliminates the low values of uncertainty in the late 1980s and early 1990s, which are an artifact of the datasets having been normalized to 1989. Figure 4C.1 shows the five OHC datasets (colors) used to construct our composite OHC dataset (black), and the corresponding uncertainty time series (gray shading). Further information regarding our formulation of OHC, and the use of the reduced χ^2 metric for OHC, is given in Hope et al., (2020) and McBride et al., (2021).

As described in Sect. 4.2.1.2, we scale the time series of ERF_{AER} by a constant multiplicative factor (s in Eq. (4.5)) to obtain an ensemble of ERF_{AER} trajectories. The ERF adjustment from IMO2020 is added to each time series for ERF_{AER} after this scaling occurs.

Figure 4C.2 shows the values of Effective Climate Sensitivity (EffCS) as the function of climate feedback and ERF_{AER}. Figure 4C.2 is similar to Fig. 4.2 in the main paper, which shows

computed values of AAWR in the same coordinate system. Colored regions correspond to ensemble members that satisfy all three reduced χ^2 observational constraints, with the colors corresponding to values of EffCS as indicated by the color bars to the right.

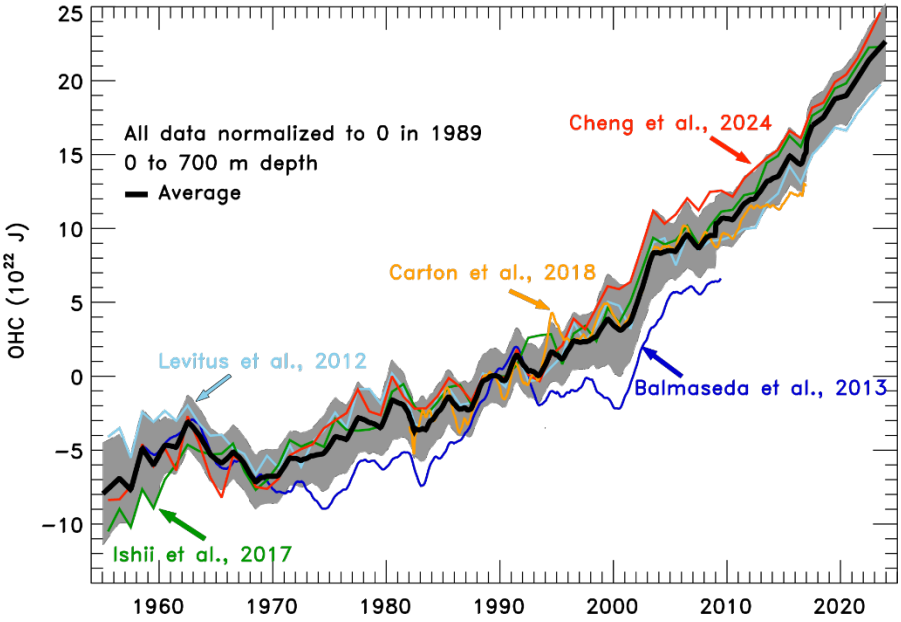

Figure 4C.1: Ocean heat content time series. Colors represent the individual OHC time series, that were used to compute the average OHC time series. The average OHC time series, and the corresponding range of uncertainty is shown by the black line and gray shading, respectively.

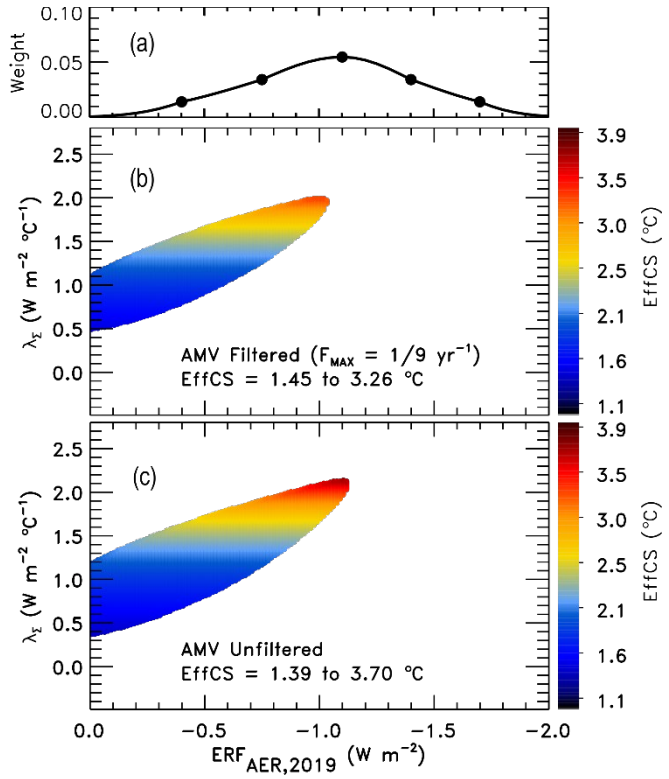

Figure 4C.2: Aerosol weighting method, and computed values of EffCS for the EM−GC ensemble. (a): Asymmetrical Gaussian function used to weight the ensemble. The points marked on the Gaussian represent the center point, the 1σ and 2σ boundaries of the Gaussian (see Sect. 2.7 and Table S3 of Farago et al., (2025)). (b) Values of EffCS as the function of λ_Σ and $ERF_{AER,2019}$. Colors denote specific values of EffCS as indicated by the color bar on the right. EffCS is only shown for those combinations of λ_Σ and $ERF_{AER,2019}$, where all three χ^2 observational constraints are satisfied. The AMV input of the simulation used to produce this panel has been Fourier-filtered to remove frequencies greater than 1/9 yr^{-1} (see text). (c) As in (b), but without a Fourier-filter having been applied to the AMV input.

Chapter 5: Conclusions and Future Opportunities

5.1 Summary and Conclusions

In this dissertation, the multiple linear regression energy balance model, the Empirical Model of Global Climate (EM−GC) is used to perform a series of policy-relevant climate model simulations. The EM−GC model simulates the rise of the global mean surface temperature (GMST) in response to increasing effective radiative forcing (ERF) from anthropogenic activity. Consequently, updated projections of the future time evolution of ERF affect the magnitude of forecasted GMST.

Chapter 7 and Annex III of the IPCC AR6 report (Forster et al., 2021a; Smith et al., 2021a; IPCC, 2021a) introduced several updates to the formulation of ERF. Chapter 2 of this dissertation focuses on quantifying the differences in the forecasted GMST under these updated projections for future ERF, relative to simulations based on ERF datasets that predate the AR6 report. The simulations are performed for four Shared Socioeconomic Pathway (SSP) scenarios. For all four SSP scenarios investigated, the adoption of the AR6 ERF datasets results in higher projected warming relative to forecasts based on pre-AR6 ERF inputs. Consequently, the simulated probability of accomplishing the target and upper limit of the Paris Agreement (PA) − that is, limiting global warming at the end of this century to 1.5 ºC and 2.0 ºC relative to pre-industrial conditions, respectively − declines substantially upon the adoption of the AR6 ERF datasets, for all four SSP scenarios investigated. Critically, the SSP2−4.5 scenario, which is considered to be the most consistent with recent trends in anthropogenic emissions of GHGs (Meinshausen et al., 2024), only offers an 8% chance of accomplishing the PA upper limit, based on simulations performed using the AR6 ERF datasets. This value is considerably smaller than the 35%

probability projected based on pre-AR6 ERF inputs (McBride et al., 2021). The GMST forecasted by several models of Phase 6 of the Coupled Model Intercomparison Project (CMIP6) nevertheless exceeds even the estimates from the AR6-based EM−GC simulations, consistent with the notion that certain CMIP6 models may overestimate the magnitude of future warming (Tokarska et al., 2020b; McBride et al., 2021; Hausfather et al., 2022; Voosen, 2022; Rugenstein et al., 2023).

Chapter 2 of this dissertation also introduces a recently proposed method (Armour, 2017; Proistosescu and Huybers, 2017; Andrews et al., 2018) for estimating Equilibrium Climate Sensitivity (ECS) by applying a correction factor to the effective climate sensitivity (EffCS) inferred from the EM−GC reconstruction of the historical GMST record. Using the best estimate for this correction factor, termed α', provided by Chapter 7 of AR6 (Forster et al., 2021a), ECS is found to be 3.24 [1.92 to 5.15 ºC, 5−95% range], which is well aligned with the combined assessment of ECS of 3.0 [2.0 ºC to 5.0 ºC] provided in AR6.

The contents of Chapter 2 of this dissertation were submitted to the EGU journal *Earth System Dynamics* (Farago et al., 2025), available online at: https://egusphere.copernicus.org/preprints/2025/egusphere-2025-342/.

Chapter 4 of this dissertation focuses on examining the record-high temperature anomalies observed in 2023 and 2024, which came as a surprise to the climate modelling community (Schmidt, 2024). A key research question for this chapter is how the stricter regulations on the sulfur content of fuel used in international shipping, beginning in January 2020 under the IMO2020 regulations, impacted the GMST anomalies observed in the following years.

Earlier versions of the EM−GC model lacked the ability to accurately capture the short-term temperature response to a sudden change in ERF, such as the abrupt reduction of sulfur emissions due to IMO2020. This problem was addressed in Chapter 3, by updating the ocean

module of EM−GC based on the two-layer energy balance model (EBM) formulations proposed by Held et al., (2010) and Geoffroy et al., (2013b). Importantly, such the two-layer EBMs are usually calibrated using the output of CMIP6 models (e.g. Geoffroy et al., (2013b), Smith et al., (2021a)). Chapter 3 describes the calibration of the two-layer EBM component of EM−GC using the observed rise in GMST and OHC. These updates therefore equip EM−GC with an ocean module capable of capturing the short-term temperature response to an abrupt change in ERF, while retaining the observation-driven nature of the previous versions of the model (Hope et al., 2020; McBride et al., 2021).

Using this updated version of EM−GC, Chapter 4 examines the impact of the IMO2020 regulations on the GMST under two scenarios, termed IMO−0.1 and IMO−0.15. These scenarios assume that the rise in global ERF due to IMO2020 (ΔERF_{IMO}) was 0.10 W m^{-2} and 0.15 W m^{-2}, respectively. These values were chosen based on recently published estimates of ΔERF_{IMO} (Table A1 in Jordan and Henry (2024)). IMO2020 is found to result in an increase in GMST of 0.028 ºC [0.027 ºC to 0.031 ºC, 5−95% range] and 0.043 ºC [0.038 ºC to 0.048 ºC] under the IMO−0.1 and IMO−0.15 scenarios, respectively. These estimates for the rise in GMST are highly consistent with other estimates currently available in the literature.

The shift from La Niña to El Niño conditions is found to be responsible for an increase in GMST of 0.08 ºC from 2022 to 2023, which explains about one third of the observed rise in GMST between these two years. Further, a strong positive IOD event, which spanned the entire year of 2023, is found to be responsible for a rise in GMST of 0.072 ºC from 2022 to 2023. Finally, short-term variability in the sea surface temperatures (SSTs) of the North Atlantic region was also found to have contributed to the elevated GMST anomalies observed in 2023 and 2024. Whether this short-term variability is a direct consequence of the introduction of the IMO2020 regulations

remains unclear, and is the subject of further research. The combined content of Chapters 3 and 4 is in preparation for submission to the EGU journal *Atmospheric Chemistry and Physics*.

5.2 Future Directions

The main body of this dissertation introduces several updates to the EM−GC modelling framework, which include updates to the input datasets as well as to the code of the model and various auxiliary codes, as described in Sect. 1.5. There are, however, several additional adjustments to the model that could be considered, which are described in this section.

The main weakness of the treatment of the ERF due to aerosols (ERF_{AER}) within EM−GC is that the temporal evolution of ERF_{AER}, in practice, the "shape" of the ERF_{AER} time series, is not allowed to vary during a simulation. As shown in Fig. 2A.1, the uncertainty in ERF_{AER} is considered through the scaling of a "best estimate" ERF_{AER} time series using a series of constant, multiplicative factors. Consequently, the model simulations rely overly heavily on the shape of the best estimate time series for ERF_{AER}. A key benefit of this method, however, is that each value of ERF_{AER} in a given reference year defines the whole time series of ERF_{AER}. Therefore, the ERF_{AER} ensemble can be represented by the values of ERF_{AER} in a given reference year, as done throughout this dissertation (e.g. Fig. 2.3). Allowing the shape of the ERF_{AER} time series to vary would break this relationship, as multiple different shapes could correspond to the same value of ERF_{AER} in a given year, similarly to Fig. 5 of Smith et al., (2021c). Further, the implementation of different shapes for ERF_{AER} would require a method to compute the various shapes for ERF_{AER}. Computing the time evolution of ERF_{AER} is quite complex however, due to the variety of parameters that influence the shape of the ERF_{AER} time series (Smith et al., 2021c). Consequently, a careful consideration of these factors is required before the model can be outfitted with a module that enables the shape of the ERF_{AER} time series to vary.

The EM−GC assumes that climate feedback is constant over the entire duration of a simulation. While this approximation was found to be appropriate in McBride et al., (2021), it remains intriguing to explore the possibility of allowing the value of the climate feedback parameter to change during a simulation. One simplified approach to implement this feature would be to include a temperature dependence in the feedback parameter. Bloch-Johnson et al., (2021) recently quantified the temperature dependence of the feedback parameter in a set of CMIP6 models. The feedback parameter was found to increase, on average, by about 0.029 W m^{-2} K^{-1} for every 1 K of a rise in the global surface temperature, though this value varies substantially between individual models. Using the above estimate, EM−GC could be equipped with a module that re-computes feedback based on the simulated GMST. If climate feedback is temperature dependent, then GMST and climate feedback mutually depend on each other. Therefore, the implementation of the temperature dependence of climate feedback would require an iterative loop and would likely result in extended simulation times. Such an improvement of the model would allow for a more accurate quantification of the uncertainty in the long-term rise in GMST, as well as the magnitude of committed warming (Mauritsen and Pincus, 2017).

The two-layer EBM representation described in Chapter 3 has been used extensively in other RCMs, such as in several versions of the FaIR model (Smith et al., 2018a; Leach et al., 2021). The most recent version of FaIR presented in Leach et al., (2021) includes a third layer, which is based upon the extension of the two-layer EBM, termed k-box EBM (Cummins et al., 2020), where k is an integer representing the amount of layers. The k-box EBM uses the same core equations as the two-layer EBM described in Chapter 3, but allows for the inclusion of additional layers to the climate system. The inclusion of additional layers leads to a more appropriate and detailed representation of vertical heat diffusion in the oceans. However, the inclusion of every additional

layer introduces a new heat transfer parameter that needs to be calibrated. Consequently, to add additional layers to the EBM module presented in Chapter 3, a method to calibrate each new heat transfer parameter would also need to be established. Further, quantifying each new heat transfer parameter based on the observed distribution of heat between various layers of the oceans would require near-global observational datasets that sample the entire depth of the oceans over multiple decades. Such datasets are not currently available, primarily due to the very limited sampling of the deep oceans at depths greater than 2000 m, particularly prior to this century (Meyssignac et al., 2019; Fox-Kemper et al., 2021). This limitation in data availability also poses challenges to the CMIP modelling community, as the simulated OHC below 2000 m depth cannot be directly compared to observations. This issue makes it challenging to verify whether CMIP6 models underestimate the rise in OHC between 700 and 2000 meters, while overestimating OHC gain below 2000 meters (Eyring et al., 2021; Fox-Kemper et al., 2021), which may result in the erroneous quantification of climate sensitivity (e.g. Mascioli et al., (2012)).

Chapter 2 has shown that there is a considerably uncertainty in computing GHG concentrations from their respective emissions. Very recently, the proposal for the standardized scenarios of the CMIP7 protocol were presented (van Vuuren et al., 2025), based on the conclusions drawn from the CMIP6 and AR6 scenario development process (Pirani et al., 2024). The proposal by van Vuuren et al., (2025) recommends emission-driven runs for CMIP7 models, thereby reducing the dependence on the pre-calculation of GHG concentrations. This new approach poses a challenge for future EM−GC modelling studies: EM−GC uses ERF as the input for anthropogenic activity, which is pre-calculated from GHG concentrations. Since EM−GC does not possess the ability to calculate GHG concentrations from emissions, future comparisons to emissions-based simulations of other climate models may be challenging. Therefore, the

possibility of including a simplified gas-cycle module to EM−GC could be explored. Such a module would likely have to be an external module of the model, rather than being directly embedded into the main code. There are several examples of such an approach in literature, and inspiration could be taken from implementations such as the one shown in Fig. 1 of Smith et al., (2018a). The EM−GC modelling team has several connections to previous efforts that modelled the atmospheric loss of methane (Nicely et al., 2020) and the efficacy of CO_2 sinks (Bennett et al., 2024), that could be leveraged for such an endeavor. Alternatively, the EM−GC model could be used in its current configuration to provide projections of future warming under the new CMIP7 scenarios proposed in van Vuuren et al., (2025), based on the pre-calculated time series of ERF shown in their Fig. 2.

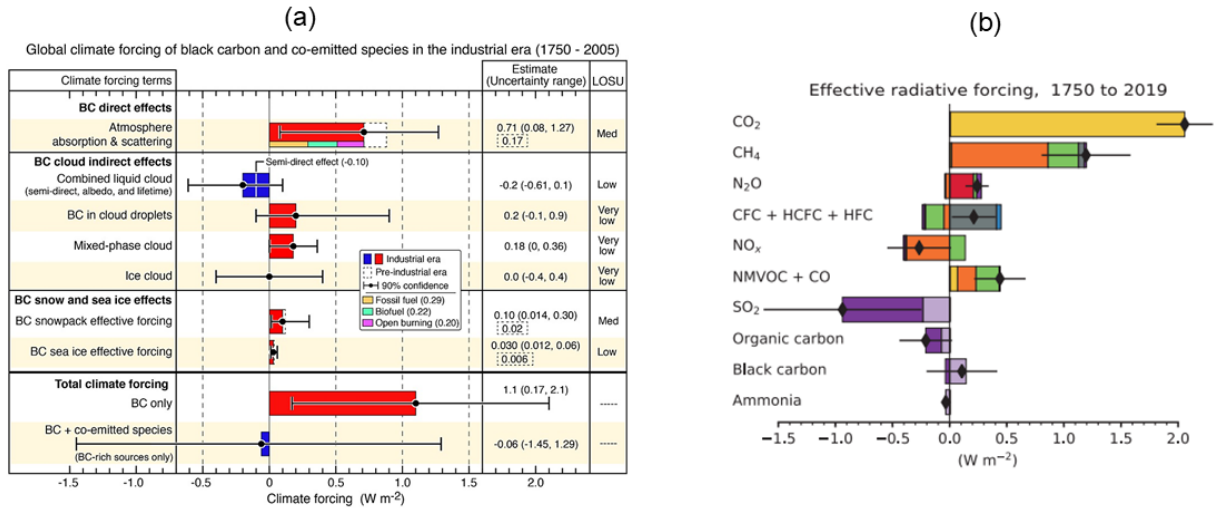

Figure 5.1: (a) Contributions of black carbon to the radiative forcing of the climate in 2005. Reproduction of Figure 35 of Bond et al., (2013). (b) ERF due to various GHGs and aerosols in 2019. Reproduction of Fig. 6.12 of Szopa et al., (2021). Values reported on both panels are with respect to a 1750 baseline. All error bars correspond to 5−95% ranges.

Chapter 4 of this dissertation examined the impact of reduced SO_2 emissions on the GMST. Emissions of SO_2 have declined not only due to the introduction of the IMO2020 regulations, but also due to lower emissions from East Asia since 2010, which has recently been linked to the

acceleration of the rate of human-induced warming (Samset et al., 2025). In contrast, emissions of black carbon, which contribute to the warming of the climate, have remained near-constant over the 2019 to 2024 period (Forster et al., 2025). The radiative forcing due to black carbon has been a topic of considerable debate and uncertainty in recent years. This uncertainty is illustrated by Fig. 5.1, which shows two estimates for the ERF due to black carbon: from the comprehensive review paper of Bond et al. (2013) on the left, and Chapter 6 of the AR6 report (Szopa et al., 2021) on the right. Figure 5.1b also shows ERF due to GHGs and other types of aerosols, but the focus of this section is the ERF due to black carbon. Bond et al. (2013) estimated the ERF due to black carbon to be 1.1 Wm^{-2} in 2005, for an annual emission rate of 7.5 Tg. This rate of emissions is nearly identical to the 2019 value of 7.8 Tg in Forster et al. (2025), yet the ERF due to black carbon was quantified by AR6 to be only 0.11 Wm^{-2} (Fig. 5.1), with a much narrower uncertainty range relative to that of Bond et al. (2013). If the estimate of ERF due to black carbon in Bond et al. (2013) is correct, then, as noted by the authors of Bond et al. (2013), an ERF of 1.1 Wm^{-2} would make black carbon the second highest contributor to the total anthropogenic ERF behind CO_2.

Quantifying the ERF of black carbon is challenging, however, not only due to the uncertainty in the estimates of anthropogenic emissions (Bond et al., 2013) and the interactions of black carbon aerosols with clouds, but also due to the large uncertainty in the rapid adjustments to the radiative forcing of black carbon (Forster et al., 2021a; Myhre et al., 2025). Conflicting evaluations exist on the magnitude and the sign of the rapid adjustments to the IRF of black carbon, with both negative (Stjern et al., 2017; Smith et al., 2018b) and positive (Allen et al., 2019) adjustments reported. While the large uncertainty in the ERF due to black carbon makes it challenging to assess the potential climate benefits of lowering the emissions of black carbon, examining the impact of reduced black carbon emissions on the GMST in a manner similar to

Chapter 4 would be a valuable contribution to the exploration of short-term climate mitigation strategies.

Bibliography

Albrecht, B. A.: Aerosols, Cloud Microphysics, and Fractional Cloudiness, Science, 245, 1227-1230, 10.1126/science.245.4923.1227, 1989.

Allen, R. J., Amiri-Farahani, A., Lamarque, J.-F., Smith, C., Shindell, D., Hassan, T., and Chung, C. E.: Observationally constrained aerosol–cloud semi-direct effects, npj Climate and Atmospheric Science, 2, 16, 10.1038/s41612-019-0073-9, 2019.

Andrews, T., Gregory, J. M., and Webb, M. J.: The Dependence of Radiative Forcing and Feedback on Evolving Patterns of Surface Temperature Change in Climate Models, Journal of Climate, 28, 1630-1648, https://doi.org/10.1175/JCLI-D-14-00545.1, 2015.

Andrews, T., Gregory, J. M., Paynter, D., Silvers, L. G., Zhou, C., Mauritsen, T., Webb, M. J., Armour, K. C., Forster, P. M., and Titchner, H.: Accounting for changing temperature patterns increases historical estimates of climate sensitivity, Geophys. Res. Lett., 45, 8490-8499, 10.1029/2018GL078887, 2018.

Andrews, T., Andrews, M. B., Bodas-Salcedo, A., Jones, G. S., Kuhlbrodt, T., Manners, J., Menary, M. B., Ridley, J., Ringer, M. A., Sellar, A. A., Senior, C. A., and Tang, Y.: Forcings, Feedbacks, and Climate Sensitivity in HadGEM3-GC3.1 and UKESM1, Journal of Advances in Modeling Earth Systems, 11, 4377-4394, https://doi.org/10.1029/2019MS001866, 2019.

Arfeuille, F., Weisenstein, D., MacK, H., Rozanov, E., Peter, T., and Brönnimann, S.: Volcanic forcing for climate modeling: A new microphysics-based data set covering years 1600-present, Climate of the Past, 10, 10.5194/cp-10-359-2014, 2014.

Armour, K. C.: Energy budget constraints on climate sensitivity in light of inconstant climate feedbacks, Nature Climate Change, 7, 10.1038/nclimate3278, 2017.

Armour, K. C., Proistosescu, C., Dong, Y., Hahn, L. C., Blanchard-Wrigglesworth, E., Pauling, A. G., Jnglin Wills, R. C., Andrews, T., Stuecker, M. F., Po-Chedley, S., Mitevski, I., Forster, P. M., and Gregory, J. M.: Sea-surface temperature pattern effects have slowed global warming and biased warming-based constraints on climate sensitivity, Proceedings of the National Academy of Sciences, 121, e2312093121, 10.1073/pnas.2312093121, 2024.

Asher, E., Todt, M., Rosenlof, K., Thornberry, T., Gao, R.-S., Taha, G., Walter, P., Alvarez, S., Flynn, J., Davis, S. M., Evan, S., Brioude, J., Metzger, J.-M., Hurst, D. F., Hall, E., and Xiong, K.: Unexpectedly rapid aerosol formation in the Hunga Tonga plume, Proceedings of the National Academy of Sciences, 120, e2219547120, 10.1073/pnas.2219547120, 2023.

Balmaseda, M. A., Trenberth, K. E., and Källén, E.: Distinctive climate signals in reanalysis of global ocean heat content, Geophysical Research Letters, 40, 10.1002/grl.50382, 2013.

Bellouin, N., Quaas, J., Gryspeerdt, E., Kinne, S., Stier, P., Watson-Parris, D., Boucher, O., Carslaw, K. S., Christensen, M., Daniau, A. L., Dufresne, J. L., Feingold, G., Fiedler, S., Forster, P., Gettelman, A., Haywood, J. M., Lohmann, U., Malavelle, F., Mauritsen, T., McCoy, D. T., Myhre, G., Mülmenstädt, J., Neubauer, D., Possner, A., Rugenstein, M.,

Sato, Y., Schulz, M., Schwartz, S. E., Sourdeval, O., Storelvmo, T., Toll, V., Winker, D., and Stevens, B.: Bounding Global Aerosol Radiative Forcing of Climate Change, 10.1029/2019RG000660, 2020.

Bennett, B. F., Salawitch, R. J., McBride, L. A., Hope, A. P., and Tribett, W. R.: Quantification of the Airborne Fraction of Atmospheric CO2 Reveals Stability in Global Carbon Sinks Over the Past Six Decades, Journal of Geophysical Research: Biogeosciences, 129, e2023JG007760, https://doi.org/10.1029/2023JG007760, 2024.

Bindoff, N. L., Stott, P. A., AchutaRao, K. M., Allen, M. R., Gillett, N., Gutzler, D., Hansingo, K., Hegerl, G., Hu, Y., Jain, S., Mokhov, I. I., Overland, J., Perlwitz, J., R., Sebbari, and Zhang, X.: Detection and Attribution of Climate Change: from Global to Regional. In: Climate Change 2013: The Physical Science Basis.

Contribution of Working Group I to the Fifth Assessment Report of the Intergovernmental Panel on Climate Change, doi:10.1017/CBO9781107415324.022, 2013.

Bloch-Johnson, J., Rugenstein, M., Stolpe, M. B., Rohrschneider, T., Zheng, Y., and Gregory, J. M.: Climate Sensitivity Increases Under Higher CO2 Levels Due to Feedback Temperature Dependence, Geophysical Research Letters, 48, e2020GL089074, https://doi.org/10.1029/2020GL089074, 2021.

Bond, T. C., Doherty, S. J., Fahey, D. W., Forster, P. M., Berntsen, T., Deangelo, B. J., Flanner, M. G., Ghan, S., Kärcher, B., Koch, D., Kinne, S., Kondo, Y., Quinn, P. K., Sarofim, M. C., Schultz, M. G., Schulz, M., Venkataraman, C., Zhang, H., Zhang, S., Bellouin, N., Guttikunda, S. K., Hopke, P. K., Jacobson, M. Z., Kaiser, J. W., Klimont, Z., Lohmann, U., Schwarz, J. P., Shindell, D., Storelvmo, T., Warren, S. G., and Zender, C. S.: Bounding the role of black carbon in the climate system: A scientific assessment, Journal of Geophysical Research Atmospheres, 118, 10.1002/jgrd.50171, 2013.

Bony, S., Colman, R., Kattsov, V. M., Allan, R. P., Bretherton, C. S., Dufresne, J. L., Hall, A., Hallegatte, S., Holland, M. M., Ingram, W., Randall, D. A., Soden, B. J., Tselioudis, G., and Webb, M. J.: How well do we understand and evaluate climate change feedback processes?, 10.1175/JCLI3819.1, 2006.

Booth, B. B. B., Dunstone, N. J., Halloran, P. R., Andrews, T., and Bellouin, N.: Aerosols implicated as a prime driver of twentieth-century North Atlantic climate variability, Nature, 484, 228-232, 10.1038/nature10946, 2012.

Boucher, O. and Randall, D.: Chapter 7: Clouds and Aerosols, in: Climate Change 2013 the Physical Science Basis: Working Group I Contribution to the Fifth Assessment Report of the Intergovernmental Panel on Climate Change, 2013.

Byrne, B. and Goldblatt, C.: Radiative forcing at high concentrations of well-mixed greenhouse gases, Geophysical Research Letters, 41, 152-160, https://doi.org/10.1002/2013GL058456, 2014.

Calvin, K., Bond-Lamberty, B., Clarke, L., Edmonds, J., Eom, J., Hartin, C., Kim, S., Kyle, P., Link, R., Moss, R., McJeon, H., Patel, P., Smith, S., Waldhoff, S., and Wise, M.: The SSP4: A world of deepening inequality, Global Environmental Change, 42, 284-296, 2017.

Canty, T., Mascioli, N. R., Smarte, M. D., and Salawitch, R. J.: An empirical model of global climate-Part 1: A critical evaluation of volcanic cooling, Atmospheric Chemistry and Physics, 13, 10.5194/acp-13-3997-2013, 2013.

Carpenter, L. J., Daniel, J. S., Lead, A., Fleming, E. L., Hanaoka, T., Ravishankara, A. R., Ross, M. N., Tilmes, S., Wallington, T. J., and Wuebbles, D. J.: Scenarios and information for policymakers, World Meteorological Organization, Geneva, Switzerland, 2018.

Carslaw, K. S., Lee, L. A., Reddington, C. L., Pringle, K. J., Rap, A., Forster, P. M., Mann, G. W., Spracklen, D. V., Woodhouse, M. T., Regayre, L. A., and Pierce, J. R.: Large contribution of natural aerosols to uncertainty in indirect forcing, Nature, 503, 67-71, 10.1038/nature12674, 2013.

Carton, J. A., Chepurin, G. A., and Chen, L.: SODA3: A new ocean climate reanalysis, Journal of Climate, 31, 10.1175/jcli-d-18-0149.1, 2018.

Carton, J. A., Chepurin, G. A., Hackert, E. C., and Huang, B.: Remarkable 2023 North Atlantic Ocean Warming, Geophysical Research Letters, 52, e2024GL112551, https://doi.org/10.1029/2024GL112551, 2025.

Charney, J. G., Arakawa, A., Baker, D. J., Bolin, B., Dickinson, R. E., Goody, R. M., Leith, C. E., Stommel, H. M., and Wunsch, C. I.: Carbon dioxide and climate: a scientific assessment, National Academy of Sciences, Washington, DC,1979.

Chen, D., Rojas, M., Samset, B. H., Cobb, K., Diongue Niang, A., Edwards, P., Emori, S., Faria, S. H., Hawkins, E., Hope, P., Huybrechts, P., Meinshausen, M., Mustafa, S. K., Plattner, G. K., and Tréguier, A. M.: Framing, Context, and Methods, in: Climate Change 2021: The Physical Science Basis. Contribution of Working Group I to the Sixth Assessment Report of the Intergovernmental Panel on Climate Change, edited by: Masson-Delmotte, V., Zhai, P., Pirani, A., Connors, S. L., Péan, C., Berger, S., Caud, N., Chen, Y., Goldfarb, L., Gomis, M. I., Huang, M., Leitzell, K., Lonnoy, E., Matthews, J. B. R., Maycock, T. K., Waterfield, T., Yelekçi, O., Yu, R., and Zhou, B., Cambridge University Press, Cambridge, United Kingdom and New York, NY, USA, 147–286, 10.1017/9781009157896.003, 2021.

Cheng, L., Trenberth, K. E., Fasullo, J., Boyer, T., Abraham, J., and Zhu, J.: Improved estimates of ocean heat content from 1960 to 2015, 10.1126/sciadv.1601545, 2017.

Cheng, L., Pan, Y., Tan, Z., Zheng, H., Zhu, Y., Wei, W., Du, J., Yuan, H., Li, G., Ye, H., Gouretski, V., Li, Y., Trenberth, K. E., Abraham, J., Jin, Y., Reseghetti, F., Lin, X., Zhang, B., Chen, G., Mann, M. E., and Zhu, J.: IAPv4 ocean temperature and ocean heat content gridded dataset, Earth Syst. Sci. Data, 16, 3517-3546, 10.5194/essd-16-3517-2024, 2024.

Church, J. A., Clark, P. U., Cazenave, A., Gregory, J. M., Jevrejeva, S., Levermann, A., Merrifield, M. A., Milne, G. A., Nerem, R. S., Nunn, P. D., Payne, A. J., Pfeffer, W. T., Stammer, D., and Unnikrishnan, A. S.: Sea Level Change. In: Climate Change 2013: The Physical Science Basis. Contribution of Working Group I to the Fifth Assessment Report of the Intergovernmental Panel on Climate Change [Stocker, T.F., D. Qin, G.-K. Plattner, M. Tignor, S.K. Allen, J. Boschung, A. Nauels, Y. Xia, V. Bex and P.M. Midgley (eds.)] doi:10.1017/ CBO9781107415324.026, 2013.

Chylek, P., Klett, J. D., Lesins, G., Dubey, M. K., and Hengartner, N.: The Atlantic Multidecadal Oscillation as a dominant factor of oceanic influence on climate, Geophysical Research Letters, 41, 10.1002/2014GL059274, 2014.

Chylek, P., Folland, C. K., Klett, J. D., Wang, M., Lesins, G., and Dubey, M. K.: Why Does the Ensemble Mean of CMIP6 Models Simulate Arctic Temperature More Accurately Than Global Temperature?, 10.3390/atmos15050567, 2024.

Cissé, G., McLeman, R., Adams, H., Aldunce, P., Bowen, K., Campbell-Lendrum, D., Clayton, S., Ebi, K. L., Hess, J., Huang, C., Liu, Q., McGregor, G., Semenza, J., and Tirado, M. C.: Health, Wellbeing, and the Changing Structure of Communities. In: Climate Change 2022: Impacts, Adaptation and Vulnerability. Contribution of Working Group II to the Sixth Assessment Report of the Intergovernmental Panel on Climate Change, doi:10.1017/9781009325844.009, 2022.

Coddington, O., Lean, J. L., Lindholm, C., and Pilewskie, P.: NOAA Climate Data Record (CDR) of NASA NOAA LASP Total Solar Irradiance (NNLTSI), Version 3. NOAA National Centers for Environmental Information, https://doi.org/10.25921/k2ff-p712, 2024.

Cooper, V. T., Armour, K. C., Hakim, G. J., Tierney, J. E., Osman, M. B., Proistosescu, C., Dong, Y., Burls, N. J., Andrews, T., Amrhein, D. E., Zhu, J., Dong, W., Ming, Y., and Chmielowiec, P.: Last Glacial Maximum pattern effects reduce climate sensitivity estimates, Science Advances, 10, eadk9461, 10.1126/sciadv.adk9461, 2024.

Cummins, D. P., Stephenson, D. B., and Stott, P. A.: A new energy-balance approach to linear filtering for estimating effective radiative forcing from temperature time series, Adv. Stat. Clim. Meteorol. Oceanogr., 6, 91-102, 10.5194/ascmo-6-91-2020, 2020.

Deser, C. and Phillips, A. S.: Defining the Internal Component of Atlantic Multidecadal Variability in a Changing Climate, Geophysical Research Letters, 48, e2021GL095023, https://doi.org/10.1029/2021GL095023, 2021.

Diamond, M. S.: Detection of large-scale cloud microphysical changes within a major shipping corridor after implementation of the International Maritime Organization 2020 fuel sulfur regulations, Atmos. Chem. Phys., 23, 8259-8269, 10.5194/acp-23-8259-2023, 2023.

Dong, Y., Armour, K. C., Zelinka, M. D., Proistosescu, C., Battisti, D. S., Zhou, C., and Andrews, T.: Intermodel Spread in the Pattern Effect and Its Contribution to Climate Sensitivity in CMIP5 and CMIP6 Models, Journal of Climate, 33, 7755-7775, https://doi.org/10.1175/JCLI-D-19-1011.1, 2020.

Dudok de Wit, T., Kopp, G., Fröhlich, C., and Schöll, M.: Methodology to create a new total solar irradiance record: Making a composite out of multiple data records, Geophysical Research Letters, 44, 10.1002/2016GL071866, 2017.

Edwards, D. P.: GENLN2: A general line-by-line atmospheric transmittance and radiance model, National Center for Atmospheric Research1992.

Enfield, D. B., Mestas-Nuñez, A. M., and Trimble, P. J.: The Atlantic Multidecadal Oscillation and its relation to rainfall and river flows in the continental U.S, Geophysical Research Letters, 28, 2077-2080, https://doi.org/10.1029/2000GL012745, 2001.

Etminan, M., Myhre, G., Highwood, E. J., and Shine, K. P.: Radiative forcing of carbon dioxide, methane, and nitrous oxide: A significant revision of the methane radiative forcing, Geophysical Research Letters, 43, 12,614-612,623, https://doi.org/10.1002/2016GL071930, 2016.

Evan, S., Brioude, J., Rosenlof, K. H., Gao, R.-S., Portmann, R. W., Zhu, Y., Volkamer, R., Lee, C. F., Metzger, J.-M., Lamy, K., Walter, P., Alvarez, S. L., Flynn, J. H., Asher, E., Todt, M., Davis, S. M., Thornberry, T., Vömel, H., Wienhold, F. G., Stauffer, R. M., Millán, L., Santee, M. L., Froidevaux, L., and Read, W. G.: Rapid ozone depletion after humidification of the stratosphere by the Hunga Tonga Eruption, Science, 382, eadg2551, 10.1126/science.adg2551, 2023.

Eyring, V., Bony, S., Meehl, G. A., Senior, C. A., Stevens, B., Stouffer, R. J., and Taylor, K. E.: Overview of the Coupled Model Intercomparison Project Phase 6 (CMIP6) experimental design and organization, Geoscientific Model Development, 9, 10.5194/gmd-9-1937-2016, 2016.

Eyring, V., Gillett, N. P., Achuta Rao, K. M., Barimalala, R., Barreiro Parrillo, M., Bellouin, N., Cassou, C., Durack, P. J., Kosaka, Y., McGregor, S., Min, S., Morgenstern, O., and Sun, Y.: Human Influence on the Climate System, in: Climate Change 2021: The Physical Science Basis. Contribution of Working Group I to the Sixth Assessment Report of the Intergovernmental Panel on Climate Change, edited by: Masson-Delmotte, V., Zhai, P., Pirani, A., Connors, S. L., Péan, C., Berger, S., Caud, N., Chen, Y., Goldfarb, L., Gomis, M. I., Huang, M., Leitzell, K., Lonnoy, E., Matthews, J. B. R., Maycock, T. K., Waterfield, T., Yelekçi, O., Yu, R., and Zhou, B., Cambridge University Press, Cambridge, United Kingdom and New York, NY, USA, 423–552, 10.1017/9781009157896.005, 2021.

Farago, E. Z., McBride, L. A., Hope, A. P., Canty, T. P., Bennett, B. F., and Salawitch, R. J.: AR6 updates to RF by GHGs and aerosols lowers the probability of accomplishing the Paris Agreement compared to AR5 formulations, EGUsphere, 2025, 1-43, 10.5194/egusphere-2025-342, 2025.

Forster, P., Storelvmo, T., Armour, K., Collins, W., Dufresne, J. L., Frame, D., Lunt, D. J., Mauritsen, T., Palmer, M. D., Watanabe, M., Wild, M., and Zhang, H.: The Earth's Energy Budget, Climate Feedbacks, and Climate Sensitivity, in: Climate Change 2021: The Physical Science Basis. Contribution of Working Group I to the Sixth Assessment Report of the Intergovernmental Panel on Climate Change, edited by: Masson-Delmotte, V., Zhai, P., Pirani, A., Connors, S. L., Péan, C., Berger, S., Caud, N., Chen, Y., Goldfarb, L., Gomis, M. I., Huang, M., Leitzell, K., Lonnoy, E., Matthews, J. B. R., Maycock, T. K., Waterfield, T., Yelekçi, O., Yu, R., and Zhou, B., Cambridge University Press, Cambridge, United Kingdom and New York, NY, USA, 923–1054, 10.1017/9781009157896.009, 2021a.

Forster, P. M., Storelvmo, T., Armour, K., Collins, W., Dufresne, J. L., Frame, D., Lunt, D. J., Mauritsen, T., Palmer, M. D., Watanabe, M., Wild, M., and Zhang, H.: Chapter 7: The Earth's Energy Budget, Climate Feedbacks, and Climate Sensitivity, Climate Change 2021: The Physical Science Basis. Contribution of Working Group I to the Sixth Assessment Report of the Intergovernmental Panel on Climate Change, 2021b.

Forster, P. M., Smith, C. J., Walsh, T., Lamb, W. F., Lamboll, R., Hauser, M., Ribes, A., Rosen, D., Gillett, N., Palmer, M. D., Rogelj, J., von Schuckmann, K., Seneviratne, S. I., Trewin,

B., Zhang, X., Allen, M., Andrew, R., Birt, A., Borger, A., Boyer, T., Broersma, J. A., Cheng, L., Dentener, F., Friedlingstein, P., Gutiérrez, J. M., Gütschow, J., Hall, B., Ishii, M., Jenkins, S., Lan, X., Lee, J. Y., Morice, C., Kadow, C., Kennedy, J., Killick, R., Minx, J. C., Naik, V., Peters, G. P., Pirani, A., Pongratz, J., Schleussner, C. F., Szopa, S., Thorne, P., Rohde, R., Rojas Corradi, M., Schumacher, D., Vose, R., Zickfeld, K., Masson-Delmotte, V., and Zhai, P.: Indicators of Global Climate Change 2022: annual update of large-scale indicators of the state of the climate system and human influence, Earth Syst. Sci. Data, 15, 2295-2327, 10.5194/essd-15-2295-2023, 2023.

Forster, P. M., Smith, C., Walsh, T., Lamb, W. F., Lamboll, R., Cassou, C., Hauser, M., Hausfather, Z., Lee, J. Y., Palmer, M. D., von Schuckmann, K., Slangen, A. B. A., Szopa, S., Trewin, B., Yun, J., Gillett, N. P., Jenkins, S., Matthews, H. D., Raghavan, K., Ribes, A., Rogelj, J., Rosen, D., Zhang, X., Allen, M., Aleluia Reis, L., Andrew, R. M., Betts, R. A., Borger, A., Broersma, J. A., Burgess, S. N., Cheng, L., Friedlingstein, P., Domingues, C. M., Gambarini, M., Gasser, T., Gütschow, J., Ishii, M., Kadow, C., Kennedy, J., Killick, R. E., Krummel, P. B., Liné, A., Monselesan, D. P., Morice, C., Mühle, J., Naik, V., Peters, G. P., Pirani, A., Pongratz, J., Minx, J. C., Rigby, M., Rohde, R., Savita, A., Seneviratne, S. I., Thorne, P., Wells, C., Western, L. M., van der Werf, G. R., Wijffels, S. E., Masson-Delmotte, V., and Zhai, P.: Indicators of Global Climate Change 2024: annual update of key indicators of the state of the climate system and human influence, Earth Syst. Sci. Data, 17, 2641-2680, 10.5194/essd-17-2641-2025, 2025.

Fox-Kemper, B., Hewitt, H. T., Xiao, C., Aðalgeirsdóttir, G., Drijfhout, S. S., Edwards, T. L., Golledge, N. R., Hemer, M., Kopp, R. E., Krinner, G., Mix, A., Notz, D., Nowicki, S., Nurhati, I. S., Ruiz, L., Sallée, J. B., Slangen, A. B. A., and Yu, Y.: Ocean, Cryosphere and Sea Level Change, in: Climate Change 2021: The Physical Science Basis. Contribution of Working Group I to the Sixth Assessment Report of the Intergovernmental Panel on Climate Change, edited by: Masson-Delmotte, V., Zhai, P., Pirani, A., Connors, S. L., Péan, C., Berger, S., Caud, N., Chen, Y., Goldfarb, L., Gomis, M. I., Huang, M., Leitzell, K., Lonnoy, E., Matthews, J. B. R., Maycock, T. K., Waterfield, T., Yelekçi, O., Yu, R., and Zhou, B., Cambridge University Press, Cambridge, United Kingdom and New York, NY, USA, 1211–1362, 10.1017/9781009157896.011, 2021.

Fricko, O., Havlik, P., Rogelj, J., Klimont, Z., Gusti, M., Johnson, N., Kolp, P., Strubegger, M., Valin, H., Amann, M., Ermolieva, T., Forsell, N., Herrero, M., Heyes, C., Kindermann, G., Krey, V., McCollum, D. L., Obersteiner, M., Pachauri, S., Rao, S., Schmid, E., Schoepp, W., and Riahi, K.: The marker quantification of the Shared Socioeconomic Pathway 2: A middle-of-the-road scenario for the 21st century, Global Environmental Change, 42, 10.1016/j.gloenvcha.2016.06.004, 2017.

Fu, B., Li, B., Gasser, T., Tao, S., Ciais, P., Piao, S., Balkanski, Y., Li, W., Yin, T., Han, L., Han, Y., Peng, S., and Xu, J.: The contributions of individual countries and regions to the global radiative forcing, Proceedings of the National Academy of Sciences, 118, e2018211118, 10.1073/pnas.2018211118, 2021.

Fujimori, S., Hasegawa, T., Masui, T., Takahashi, K., Herran, D. S., Dai, H., Hijioka, Y., and Kainuma, M.: SSP3: AIM implementation of Shared Socioeconomic Pathways, Global Environmental Change, 42, 10.1016/j.gloenvcha.2016.06.009, 2017.

Geoffroy, O., Saint-Martin, D., Bellon, G., Voldoire, A., Olivié, D. J. L., and Tytéca, S.: Transient Climate Response in a Two-Layer Energy-Balance Model. Part II: Representation of the Efficacy of Deep-Ocean Heat Uptake and Validation for CMIP5 AOGCMs, Journal of Climate, 26, 1859-1876, https://doi.org/10.1175/JCLI-D-12-00196.1, 2013a.

Geoffroy, O., Saint-Martin, D., Olivié, D. J. L., Voldoire, A., Bellon, G., and Tytéca, S.: Transient Climate Response in a Two-Layer Energy-Balance Model. Part I: Analytical Solution and Parameter Calibration Using CMIP5 AOGCM Experiments, Journal of Climate, 26, 1841-1857, https://doi.org/10.1175/JCLI-D-12-00195.1, 2013b.

Gettelman, A., Christensen, M. W., Diamond, M. S., Gryspeerdt, E., Manshausen, P., Stier, P., Watson-Parris, D., Yang, M., Yoshioka, M., and Yuan, T.: Has Reducing Ship Emissions Brought Forward Global Warming?, Geophysical Research Letters, 51, e2024GL109077, https://doi.org/10.1029/2024GL109077, 2024.

Ghan, S. J., Smith, S. J., Wang, M., Zhang, K., Pringle, K., Carslaw, K., Pierce, J., Bauer, S., and Adams, P.: A simple model of global aerosol indirect effects, Journal of Geophysical Research: Atmospheres, 118, 6688-6707, https://doi.org/10.1002/jgrd.50567, 2013.

Goessling, H. F., Rackow, T., and Jung, T.: Recent global temperature surge intensified by record-low planetary albedo, Science, 387, 68-73, 10.1126/science.adq7280, 2025.

Good, P., Gregory, J. M., and Lowe, J. A.: A step-response simple climate model to reconstruct and interpret AOGCM projections, Geophysical Research Letters, 38, https://doi.org/10.1029/2010GL045208, 2011.

Gregory, J. M., Andrews, T., and Good, P.: The inconstancy of the transient climate response parameter under increasing CO2, Philosophical Transactions of the Royal Society A: Mathematical, Physical and Engineering Sciences, 373, 20140417, 10.1098/rsta.2014.0417, 2015.

Gregory, J. M., Andrews, T., Ceppi, P., Mauritsen, T., and Webb, M. J.: How accurately can the climate sensitivity to CO2 be estimated from historical climate change?, Climate Dynamics, 54, 129-157, 10.1007/s00382-019-04991-y, 2020.

Gregory, J. M., Ingram, W. J., Palmer, M. A., Jones, G. S., Stott, P. A., Thorpe, R. B., Lowe, J. A., Johns, T. C., and Williams, K. D.: A new method for diagnosing radiative forcing and climate sensitivity, Geophys. Res. Lett., 31, 10.1029/2003GL018747, 2004.

Gulev, S. K., Thorne, P. W., Ahn, J., Dentener, F. J., Domingues, C. M., Gerland, S., Gong, D., Kaufman, D. S., Nnamchi, H. C., Quaas, J., Rivera, J. A., Sathyendranath, S., Smith, S. L., Trewin, B., von Schuckmann, K., and Vose, R. S.: Changing State of the Climate System, in: Climate Change 2021: The Physical Science Basis. Contribution of Working Group I to the Sixth Assessment Report of the Intergovernmental Panel on Climate Change, edited by: Masson-Delmotte, V., Zhai, P., Pirani, A., Connors, S. L., Péan, C., Berger, S., Caud, N., Chen, Y., Goldfarb, L., Gomis, M. I., Huang, M., Leitzell, K., Lonnoy, E., Matthews, J. B. R., Maycock, T. K., Waterfield, T., Yelekçi, O., Yu, R., and Zhou, B., Cambridge University Press, Cambridge, United Kingdom and New York, NY, USA, 287–422, 10.1017/9781009157896.004, 2021.

Gupta, A. K., Mittal, T., Fauria, K. E., Bennartz, R., and Kok, J. F.: The January 2022 Hunga eruption cooled the southern hemisphere in 2022 and 2023, Communications Earth & Environment, 6, 240, 10.1038/s43247-025-02181-9, 2025.

Hansen, J., Sato, M., Kharecha, P., and Von Schuckmann, K.: Earth's energy imbalance and implications, Atmospheric Chemistry and Physics, 11, 10.5194/acp-11-13421-2011, 2011.

Hartmann, D. L., Tank, a. M. G. K., and Rusticucci, M.: IPCC Fifth Assessment Report, Climatie Change 2013: The Physical Science Basis, 2013.

Hausfather, Z., Marvel, K., Schmidt, G. A., Nielsen-Gammon, J. W., and Zelinka, M.: Climate simulations: recognize the 'hot model' problem, Nature, 605, 26-29, 10.1038/d41586-022-01192-2, 2022.

Held, I. M., Winton, M., Takahashi, K., Delworth, T., Zeng, F., and Vallis, G. K.: Probing the Fast and Slow Components of Global Warming by Returning Abruptly to Preindustrial Forcing, Journal of Climate, 23, 2418-2427, https://doi.org/10.1175/2009JCLI3466.1, 2010.

Hodnebrog, Ø., Myhre, G., Kramer, R. J., Shine, K. P., Andrews, T., Faluvegi, G., Kasoar, M., Kirkevåg, A., Lamarque, J.-F., Mülmenstädt, J., Olivié, D., Samset, B. H., Shindell, D., Smith, C. J., Takemura, T., and Voulgarakis, A.: The effect of rapid adjustments to halocarbons and N2O on radiative forcing, npj Climate and Atmospheric Science, 3, 43, 10.1038/s41612-020-00150-x, 2020.

Hope, A. P., Canty, T. P., Salawitch, R. J., Tribett, W. R., and Bennett, B. F.: Forecasting global warming, in: Springer Climate, 10.1007/978-3-319-46939-3_2, 2017.

Hope, A. P., McBride, L. A., Canty, T. P., Bennett, B. F., Tribett, W. R., and Salawitch, R. J.: Examining the human influence on global climate using an empirical model, 10.1002/essoar.10504179.1, 2020.

IMO: IMO 2020: Consistent Implementation of MARPOL Annex VI, 2019.

IPCC: Climate Change 2001: The Scientific Basis. Contribution of Working Group I to the Third Assessment Report of the Intergovernmental Panel on Climate Change [Houghton, J.T., Y. Ding, D.J. Griggs, M. Noguer, P.J. van der Linden, X. Dai, K. Maskell, and C.A. Johnson (eds.)], 2001.

IPCC: Climate Change 2007: The Physical Science Basis. Contribution of Working Group I to the Fourth Assessment Report of the Intergovernmental Panel on Climate Change [Solomon, S., D. Qin, M. Manning, Z. Chen, M. Marquis, K.B. Averyt, M. Tignor and H.L. Miller (eds.)], 2007.

IPCC: Annex II: Climate System Scenario Tables [Prather, M., G. Flato, P. Friedlingstein, C. Jones, J.-F. Lamarque, H. Liao and P. Rasch (eds.)]. In: Climate Change 2013: The Physical Science Basis. Contribution of Working Group I to the Fifth Assessment Report of the Intergovernmental Panel on Climate Change [Stocker, T.F., D. Qin, G.-K. Plattner, M. Tignor, S.K. Allen, J. Boschung, A. Nauels, Y. Xia, V. Bex and P.M. Midgley (eds.)] doi: 10.1017/CBO9781107415324.030., 2013a.

IPCC: Climate Change 2013: The Physical Science Basis. Contribution of Working Group I to the Fifth Assessment Report of the Intergovernmental Panel on Climate Change [Stocker, T.F.,

D. Qin, G.-K. Plattner, M. Tignor, S.K. Allen, J. Boschung, A. Nauels, Y. Xia, V. Bex and P.M. Midgley (eds.)]. doi:10.1017/CBO9781107415324, 2013b.

IPCC: Annex III: Tables of historical and projected well-mixed greenhouse gas mixing ratios and effective radiative forcing of all climate forcers [Dentener F.J., B. Hall, C. Smith (eds.)], in: Climate Change 2021: The Physical Science Basis. Contribution of Working Group I to the Sixth Assessment Report of the Intergovernmental Panel on Climate Change, edited by: Masson-Delmotte, V., Zhai, P., Pirani, A., Connors, S. L., Péan, C., Berger, S., Caud, N., Chen, Y., Goldfarb, L., Gomis, M. I., Huang, M., Leitzell, K., Lonnoy, E., Matthews, J. B. R., Maycock, T. K., Waterfield, T., Yelekçi, O., Yu, R., and Zhou, B., Cambridge University Press, Cambridge, United Kingdom and New York, NY, USA, 2139–2152, 10.1017/9781009157896.017, 2021a.

IPCC: Climate Change 2021: The Physical Science Basis. Contribution of Working Group I to the Sixth Assessment Report of the Intergovernmental Panel on Climate Change, Cambridge University Press, Cambridge, United Kingdom and New York, NY, USA, 10.1017/9781009157896, 2021b.

IPCC: Annex VII: Glossary [Matthews, J.B.R., V. Möller, R. van Diemen, J.S. Fuglestvedt, V. Masson-Delmotte, C. Méndez, S. Semenov, A. Reisinger (eds.)], in: Climate Change 2021: The Physical Science Basis. Contribution of Working Group I to the Sixth Assessment Report of the Intergovernmental Panel on Climate Change, edited by: Masson-Delmotte, V., Zhai, P., Pirani, A., Connors, S. L., Péan, C., Berger, S., Caud, N., Chen, Y., Goldfarb, L., Gomis, M. I., Huang, M., Leitzell, K., Lonnoy, E., Matthews, J. B. R., Maycock, T. K., Waterfield, T., Yelekçi, O., Yu, R., and Zhou, B., Cambridge University Press, Cambridge, United Kingdom and New York, NY, USA, 2215–2256, 10.1017/9781009157896.022, 2021c.

Ishii, M., Shouji, A., Sugimoto, S., and Matsumoto, T.: Objective analyses of sea-surface temperature and marine meteorological variables for the 20th century using ICOADS and the Kobe Collection, International Journal of Climatology, 25, 10.1002/joc.1169, 2005.

Ishii, M., Fukuda, Y., Hirahara, S., Yasui, S., Suzuki, T., and Sato, K.: Accuracy of Global Upper Ocean Heat Content Estimation Expected from Present Observational Data Sets, SOLA, 13, 10.2151/sola.2017-030, 2017.

Jenkins, S., Smith, C., Allen, M., and Grainger, R.: Tonga eruption increases chance of temporary surface temperature anomaly above 1.5 °C, Nature Climate Change, 13, 127-129, 10.1038/s41558-022-01568-2, 2023.

Jones, C. D., Arora, V., Friedlingstein, P., Bopp, L., Brovkin, V., Dunne, J., Graven, H., Hoffman, F., Ilyina, T., John, J. G., Jung, M., Kawamiya, M., Koven, C., Pongratz, J., Raddatz, T., Randerson, J. T., and Zaehle, S.: C4MIP – The Coupled Climate–Carbon Cycle Model Intercomparison Project: experimental protocol for CMIP6, Geosci. Model Dev., 9, 2853-2880, 10.5194/gmd-9-2853-2016, 2016.

Jordan, G. and Henry, M.: IMO2020 Regulations Accelerate Global Warming by up to 3 Years in UKESM1, Earth's Future, 12, e2024EF005011, https://doi.org/10.1029/2024EF005011, 2024.

Kennedy, J. J., Rayner, N. A., Atkinson, C. P., and Killick, R. E.: An Ensemble Data Set of Sea Surface Temperature Change From 1850: The Met Office Hadley Centre HadSST.4.0.0.0 Data Set, Journal of Geophysical Research: Atmospheres, 124, 10.1029/2018JD029867, 2019.

Kennedy, J. J., Rayner, N. A., Smith, R. O., Parker, D. E., and Saunby, M.: Reassessing biases and other uncertainties in sea surface temperature observations measured in situ since 1850: 1. Measurement and sampling uncertainties, Journal of Geophysical Research Atmospheres, 116, 10.1029/2010JD015218, 2011.

Kirtman, B., Power, S. B., Adedoyin, J. A., Boer, G. J., Bojariu, R., Camilloni, I., Doblas-Reyes, F. J., Fiore, A. M., Kimoto, M., Meehl, G. A., Prather, M., Sarr, A., Schär, C., Sutton, R., van Oldenborgh, G. J., Vecchi, G., and Wang, H. J.: Near-term Climate Change: Projections and Predictability. In: Climate Change 2013: The Physical Science Basis. Contribution of Working Group I to the Fifth Assessment Report of the Intergovernmental Panel on Climate Change [Stocker, T.F., D. Qin, G.-K. Plattner, M. Tignor, S.K. Allen, J. Boschung, A. Nauels, Y. Xia, V. Bex and P.M. Midgley (eds.)]. doi:10.1017/CBO9781107415324.023, 2013.

Knutti, R., Rugenstein, M. A. A., and Hegerl, G. C.: Beyond equilibrium climate sensitivity, Nat. Geosci., 10, 727-736, 10.1038/ngeo3017, 2017.

Kriegler, E., Bauer, N., Popp, A., Humpenöder, F., Leimbach, M., Strefler, J., Baumstark, L., Bodirsky, B. L., Hilaire, J., Klein, D., Mouratiadou, I., Weindl, I., Bertram, C., Dietrich, J. P., Luderer, G., Pehl, M., Pietzcker, R., Piontek, F., Lotze-Campen, H., Biewald, A., Bonsch, M., Giannousakis, A., Kreidenweis, U., Müller, C., Rolinski, S., Schultes, A., Schwanitz, J., Stevanovic, M., Calvin, K., Emmerling, J., Fujimori, S., and Edenhofer, O.: Fossil-fueled development (SSP5): An energy and resource intensive scenario for the 21st century, Global Environmental Change, 42, 10.1016/j.gloenvcha.2016.05.015, 2017.

Kuhlbrodt, T., Swaminathan, R., Ceppi, P., and Wilder, T.: A Glimpse into the Future: The 2023 Ocean Temperature and Sea Ice Extremes in the Context of Longer-Term Climate Change, Bulletin of the American Meteorological Society, 105, E474-E485, https://doi.org/10.1175/BAMS-D-23-0209.1, 2024.

Lan, X., Tans, P., and Thoning, K. W.: Trends in globally-averaged CO2 determined from NOAA Global Monitoring Laboratory measurements. Version 2024-01, https://doi.org/10.15138/9N0H-ZH07, 2024a.

Lan, X., Thoning, K. W., and Dlugokencky, E. J.: Trends in globally-averaged CH4, N2O, and SF6 determined from NOAA Global Monitoring Laboratory measurements. Version 2024-01, https://doi.org/10.15138/P8XG-AA10, 2024b.

Lawrence, D. M., Hurtt, G. C., Arneth, A., Brovkin, V., Calvin, K. V., Jones, A. D., Jones, C. D., Lawrence, P. J., de Noblet-Ducoudré, N., Pongratz, J., Seneviratne, S. I., and Shevliakova, E.: The Land Use Model Intercomparison Project (LUMIP) contribution to CMIP6: rationale and experimental design, Geosci. Model Dev., 9, 2973-2998, 10.5194/gmd-9-2973-2016, 2016.

Leach, N. J., Jenkins, S., Nicholls, Z., Smith, C. J., Lynch, J., Cain, M., Walsh, T., Wu, B., Tsutsui, J., and Allen, M. R.: FaIRv2.0.0: a generalized impulse response model for climate

uncertainty and future scenario exploration, Geosci. Model Dev., 14, 3007-3036, 10.5194/gmd-14-3007-2021, 2021.

Lean, J. L. and Rind, D. H.: How natural and anthropogenic influences alter global and regional surface temperatures: 1889 to 2006, Geophysical Research Letters, 35, 10.1029/2008GL034864, 2008.

Lean, J. L. and Rind, D. H.: How will Earth's surface temperature change in future decades?, Geophysical Research Letters, 36, 10.1029/2009GL038932, 2009.

Lee, J. Y., Marotzke, J., Bala, G., Cao, L., Corti, S., Dunne, J. P., Engelbrecht, F., Fischer, E., Fyfe, J. C., Jones, C., Maycock, A., Mutemi, J., Ndiaye, O., Panickal, S., and Zhou, T.: Future Global Climate: Scenario-Based Projections and Near-Term Information, in: Climate Change 2021: The Physical Science Basis. Contribution of Working Group I to the Sixth Assessment Report of the Intergovernmental Panel on Climate Change, edited by: Masson-Delmotte, V., Zhai, P., Pirani, A., Connors, S. L., Péan, C., Berger, S., Caud, N., Chen, Y., Goldfarb, L., Gomis, M. I., Huang, M., Leitzell, K., Lonnoy, E., Matthews, J. B. R., Maycock, T. K., Waterfield, T., Yelekçi, O., Yu, R., and Zhou, B., Cambridge University Press, Cambridge, United Kingdom and New York, NY, USA, 553–672, 10.1017/9781009157896.006, 2021.

Levitus, S., Antonov, J. I., Boyer, T. P., Baranova, O. K., Garcia, H. E., Locarnini, R. A., Mishonov, A. V., Reagan, J. R., Seidov, D., Yarosh, E. S., and Zweng, M. M.: World ocean heat content and thermosteric sea level change (0-2000m), 1955-2010, Geophysical Research Letters, 39, 10.1029/2012GL051106, 2012.

Mantua, N., Hare, S., Zhang, Y., Wallace, J., and Francis, R.: A Pacific Interdecadal Climate Oscillation with Impacts on Salmon Production, Bulletin of the American Meteorological Society, 78, 1069-1079, 10.1175/1520-0477(1997)078%3C1069:APICOW%3E2.0.CO;2, 1997.

Mascioli, N., Canty, T., and Salawitch, R.: An empirical model of global climate - Part 2: Implications for future temperature, Atmospheric Chemistry & Physics Discussions, 12, 23913-23974, 10.5194/acpd-12-23913-2012, 2012.

Matthes, K., Funke, B., Andersson, M. E., Barnard, L., Beer, J., Charbonneau, P., Clilverd, M. A., Dudok De Wit, T., Haberreiter, M., Hendry, A., Jackman, C. H., Kretzschmar, M., Kruschke, T., Kunze, M., Langematz, U., Marsh, D. R., Maycock, A. C., Misios, S., Rodger, C. J., Scaife, A. A., Seppälä, A., Shangguan, M., Sinnhuber, M., Tourpali, K., Usoskin, I., Van De Kamp, M., Verronen, P. T., and Versick, S.: Solar forcing for CMIP6 (v3.2), Geoscientific Model Development, 10, 10.5194/gmd-10-2247-2017, 2017.

Mauritsen, T. and Pincus, R.: Committed warming inferred from observations, Nature Climate Change, 7, 652-655, 10.1038/nclimate3357, 2017.

McBride, L. A., Hope, A. P., Canty, T. P., Bennett, B. F., Tribett, W. R., and Salawitch, R. J.: Comparison of CMIP6 historical climate simulations and future projected warming to an empirical model of global climate, Earth System Dynamics, 12, 10.5194/esd-12-545-2021, 2021.

Meinshausen, M., Raper, S. C. B., and Wigley, T. M. L.: Emulating coupled atmosphere-ocean and carbon cycle models with a simpler model, MAGICC6 - Part 1: Model description and calibration, Atmospheric Chemistry and Physics, 11, 10.5194/acp-11-1417-2011, 2011a.

Meinshausen, M., Wigley, T. M. L., and Raper, S. C. B.: Emulating atmosphere-ocean and carbon cycle models with a simpler model, MAGICC6 – Part 2: Applications, Atmos. Chem. Phys., 11, 1457-1471, 10.5194/acp-11-1457-2011, 2011b.

Meinshausen, M., Smith, S. J., Calvin, K., Daniel, J. S., Kainuma, M. L. T., Lamarque, J., Matsumoto, K., Montzka, S. A., Raper, S. C. B., Riahi, K., Thomson, A., Velders, G. J. M., and van Vuuren, D. P. P.: The RCP greenhouse gas concentrations and their extensions from 1765 to 2300, Climatic Change, 109, 10.1007/s10584-011-0156-z, 2011c.

Meinshausen, M., Nicholls, Z. R. J., Lewis, J., Gidden, M. J., Vogel, E., Freund, M., Beyerle, U., Gessner, C., Nauels, A., Bauer, N., Canadell, J. G., Daniel, J. S., John, A., Krummel, P. B., Luderer, G., Meinshausen, N., Montzka, S. A., Rayner, P. J., Reimann, S., Smith, S. J., Van Den Berg, M., Velders, G. J. M., Vollmer, M. K., and Wang, R. H. J.: The shared socio-economic pathway (SSP) greenhouse gas concentrations and their extensions to 2500, Geoscientific Model Development, 13, 10.5194/gmd-13-3571-2020, 2020.

Meinshausen, M., Vogel, E., Nauels, A., Lorbacher, K., Meinshausen, N., Etheridge, D. M., Fraser, P. J., Montzka, S. A., Rayner, P. J., Trudinger, C. M., Krummel, P. B., Beyerle, U., Canadell, J. G., Daniel, J. S., Enting, I. G., Law, R. M., Lunder, C. R., O'Doherty, S., Prinn, R. G., Reimann, S., Rubino, M., Velders, G. J. M., Vollmer, M. K., Wang, R. H. J., and Weiss, R.: Historical greenhouse gas concentrations for climate modelling (CMIP6), Geoscientific Model Development, 10, 10.5194/gmd-10-2057-2017, 2017.

Meinshausen, M., Schleussner, C. F., Beyer, K., Bodeker, G., Boucher, O., Canadell, J. G., Daniel, J. S., Diongue-Niang, A., Driouech, F., Fischer, E., Forster, P., Grose, M., Hansen, G., Hausfather, Z., Ilyina, T., Kikstra, J. S., Kimutai, J., King, A. D., Lee, J. Y., Lennard, C., Lissner, T., Nauels, A., Peters, G. P., Pirani, A., Plattner, G. K., Pörtner, H., Rogelj, J., Rojas, M., Roy, J., Samset, B. H., Sanderson, B. M., Séférian, R., Seneviratne, S., Smith, C. J., Szopa, S., Thomas, A., Urge-Vorsatz, D., Velders, G. J. M., Yokohata, T., Ziehn, T., and Nicholls, Z.: A perspective on the next generation of Earth system model scenarios: towards representative emission pathways (REPs), Geosci. Model Dev., 17, 4533-4559, 10.5194/gmd-17-4533-2024, 2024.

Meyssignac, B., Boyer, T., Zhao, Z., Hakuba, M. Z., Landerer, F. W., Stammer, D., Köhl, A., Kato, S., L'Ecuyer, T., Ablain, M., Abraham, J. P., Blazquez, A., Cazenave, A., Church, J. A., Cowley, R., Cheng, L., Domingues, C. M., Giglio, D., Gouretski, V., Ishii, M., Johnson, G. C., Killick, R. E., Legler, D., Llovel, W., Lyman, J., Palmer, M. D., Piotrowicz, S., Purkey, S. G., Roemmich, D., Roca, R., Savita, A., von Schuckmann, K., Speich, S., Stephens, G., Wang, G., Wijffels, S. E., and Zilberman, N.: Measuring Global Ocean Heat Content to Estimate the Earth Energy Imbalance, Frontiers in Marine Science, 6, 432, 10.3389/fmars.2019.00432, 2019.

Millán, L., Santee, M. L., Lambert, A., Livesey, N. J., Werner, F., Schwartz, M. J., Pumphrey, H. C., Manney, G. L., Wang, Y., Su, H., Wu, L., Read, W. G., and Froidevaux, L.: The Hunga Tonga-Hunga Ha'apai Hydration of the Stratosphere, Geophysical Research Letters, 49, e2022GL099381, https://doi.org/10.1029/2022GL099381, 2022.

Morice, C. P., Kennedy, J. J., Rayner, N. A., Winn, J. P., Hogan, E., Killick, R. E., Dunn, R. J. H., Osborn, T. J., Jones, P. D., and Simpson, I. R.: An Updated Assessment of Near-Surface Temperature Change From 1850: The HadCRUT5 Data Set, Journal of Geophysical Research: Atmospheres, 126, 10.1029/2019JD032361, 2021.

Myhre, G. and Stordal, F.: Role of spatial and temporal variations in the computation of radiative forcing and GWP, Journal of Geophysical Research: Atmospheres, 102, 11181-11200, https://doi.org/10.1029/97JD00148, 1997.

Myhre, G., Highwood, E. J., Shine, K. P., and Stordal, F.: New estimates of radiative forcing due to well mixed greenhouse gases, Geophysical Research Letters, 25, 10.1029/98GL01908, 1998.

Myhre, G., Stordal, F., Gausemel, I., Nielsen, C. J., and Mahieu, E.: Line-by-line calculations of thermal infrared radiation representative for global condition: CFC-12 as an example, Journal of Quantitative Spectroscopy and Radiative Transfer, 97, 317-331, https://doi.org/10.1016/j.jqsrt.2005.04.015, 2006.

Myhre, G., Nilsen, J. S., Gulstad, L., Shine, K. P., Rognerud, B., and Isaksen, I. S. A.: Radiative forcing due to stratospheric water vapour from CH4 oxidation, Geophysical Research Letters, 34, https://doi.org/10.1029/2006GL027472, 2007.

Myhre, G., Shindell, D., Bréon, F.-M., Collins, W., Fuglestvedt, J., Huang, J., Koch, D., Lamarque, J.-F., Lee, D., Mendoza, B., Nakajima, T., Robock, A., Stephens, G., Takemura, T., and Zhang, H.: Anthropogenic and Natural Radiative Forcing Supplementary Material. In: Climate Change 2013: The Physical Science Basis. Contribution of Working Group I to the Fifth Assessment Report of the Intergovernmental Panel on Climate Change [Stocker, T.F., D. Qin, G.-K. Plattner, M. Tignor, S.K. Allen, J. Boschung, A. Nauels, Y. Xia, V. Bex and P.M. Midgley (eds.)]. 2013a.

Myhre, G., Shindell, D., Bréon, F. M., Collins, W. D., Fuglestvedt, J., Huang, J., Koch, D., Lamarque, J. F., Lee, D., Mendoza, B., Nakajima, T., Robock, a., Stephens, G., Takemura, T., and Zhan, H.: IPCC AR5 (2013) Chapter 8: Anthropogenic and Natural Radiative Forcing, in: Climate Change 2013: The Physical Science Basis. Contribution of Working Group I to the Fifth Assessment Report of the Intergovernmental Panel on Climate Change, 2013b.

Myhre, G., Samset, B. H., Stjern, C. W., Hodnebrog, Ø., Kramer, R., Smith, C., Andrews, T., Boucher, O., Faluvegi, G., Forster, P. M., Iversen, T., Kirkevåg, A., Olivié, D., Shindell, D., Stier, P., and Watson-Parris, D.: The warming effect of black carbon must be reassessed in light of observational constraints, Cell Reports Sustainability, 10.1016/j.crsus.2025.100428, 2025.

Myhre, G., Samset, B. H., Schulz, M., Balkanski, Y., Bauer, S., Berntsen, T. K., Bian, H., Bellouin, N., Chin, M., Diehl, T., Easter, R. C., Feichter, J., Ghan, S. J., Hauglustaine, D., Iversen, T., Kinne, S., Kirkevåg, A., Lamarque, J. F., Lin, G., Liu, X., Lund, M. T., Luo, G., Ma, X., van Noije, T., Penner, J. E., Rasch, P. J., Ruiz, A., Seland, Ø., Skeie, R. B., Stier, P., Takemura, T., Tsigaridis, K., Wang, P., Wang, Z., Xu, L., Yu, H., Yu, F., Yoon, J. H., Zhang, K., Zhang, H., and Zhou, C.: Radiative forcing of the direct aerosol effect from AeroCom Phase II simulations, Atmos. Chem. Phys., 13, 1853-1877, 10.5194/acp-13-1853-2013, 2013c.

Newman, M., Alexander, M. A., Ault, T. R., Cobb, K. M., Deser, C., Di Lorenzo, E., Mantua, N. J., Miller, A. J., Minobe, S., Nakamura, H., Schneider, N., Vimont, D. J., Phillips, A. S., Scott, J. D., and Smith, C. A.: The Pacific Decadal Oscillation, Revisited, Journal of Climate, 29, 4399-4427, https://doi.org/10.1175/JCLI-D-15-0508.1, 2016.

Nicely, J. M., Duncan, B. N., Hanisco, T. F., Wolfe, G. M., Salawitch, R. J., Deushi, M., Haslerud, A. S., Jöckel, P., Josse, B., Kinnison, D. E., Klekociuk, A., Manyin, M. E., Marécal, V., Morgenstern, O., Murray, L. T., Myhre, G., Oman, L. D., Pitari, G., Pozzer, A., Quaglia, I., Revell, L. E., Rozanov, E., Stenke, A., Stone, K., Strahan, S., Tilmes, S., Tost, H., Westervelt, D. M., and Zeng, G.: A machine learning examination of hydroxyl radical differences among model simulations for CCMI-1, Atmos. Chem. Phys., 20, 1341-1361, 10.5194/acp-20-1341-2020, 2020.

Nicholls, Z., Meinshausen, M., Lewis, J., Corradi, M. R., Dorheim, K., Gasser, T., Gieseke, R., Hope, A. P., Leach, N. J., McBride, L. A., Quilcaille, Y., Rogelj, J., Salawitch, R. J., Samset, B. H., Sandstad, M., Shiklomanov, A., Skeie, R. B., Smith, C. J., Smith, S. J., Su, X., Tsutsui, J., Vega-Westhoff, B., and Woodard, D. L.: Reduced Complexity Model Intercomparison Project Phase 2: Synthesizing Earth System Knowledge for Probabilistic Climate Projections, Earth's Future, 9, 10.1029/2020EF001900, 2021.

Nicholls, Z., Meinshausen, M., Lewis, J., Gieseke, R., Dommenget, D., Dorheim, K., Fan, C. S., Fuglestvedt, J. S., Gasser, T., Goluke, U., Goodwin, P., Hartin, C., P. Hope, A., Kriegler, E., J. Leach, N., Marchegiani, D., A. McBride, L., Quilcaille, Y., Rogelj, J., J. Salawitch, R., Samset, B. H., Sandstad, M., N. Shiklomanov, A., B. Skeie, R., J. Smith, C., Smith, S., Tanaka, K., Tsutsui, J., and Xie, Z.: Reduced Complexity Model Intercomparison Project Phase 1: Introduction and evaluation of global-mean temperature response, Geoscientific Model Development, 13, 10.5194/gmd-13-5175-2020, 2020.

O'Neill, B. C., Kriegler, E., Riahi, K., Ebi, K. L., Hallegatte, S., Carter, T. R., Mathur, R., and van Vuuren, D. P.: A new scenario framework for climate change research: The concept of shared socioeconomic pathways, Climatic Change, 122, 10.1007/s10584-013-0905-2, 2014.

O'Neill, B. C., Tebaldi, C., van Vuuren, D. P., Eyring, V., Friedlingstein, P., Hurtt, G., Knutti, R., Kriegler, E., Lamarque, J. F., Lowe, J., Meehl, G. A., Moss, R., Riahi, K., and Sanderson, B. M.: The Scenario Model Intercomparison Project (ScenarioMIP) for CMIP6, Geosci. Model Dev., 9, 3461-3482, 10.5194/gmd-9-3461-2016, 2016.

Otto, A., Otto, F. E. L., Boucher, O., Church, J., Hegerl, G., Forster, P. M., Gillett, N. P., Gregory, J., Johnson, G. C., Knutti, R., Lewis, N., Lohmann, U., Marotzke, J., Myhre, G., Shindell, D., Stevens, B., and Allen, M. R.: Energy budget constraints on climate response, 10.1038/ngeo1836, 2013.

Pirani, A., Fuglestvedt, J. S., Byers, E., O'Neill, B., Riahi, K., Lee, J.-Y., Marotzke, J., Rose, S. K., Schaeffer, R., and Tebaldi, C.: Scenarios in IPCC assessments: lessons from AR6 and opportunities for AR7, npj Climate Action, 3, 1, 10.1038/s44168-023-00082-1, 2024.

Poletti, A. N., Frierson, D. M. W., and Armour, K. C.: Why Do CO2 Quadrupling Simulations Warm More Than Twice as Much as CO2 Doubling Simulations in CMIP6?, Geophysical Research Letters, 51, e2023GL107320, https://doi.org/10.1029/2023GL107320, 2024.

Proistosescu, C. and Huybers, P. J.: Slow climate mode reconciles historical and model-based estimates of climate sensitivity, 10.1126/sciadv.1602821, 2017.

Qin, M., Dai, A., and Hua, W.: Quantifying Contributions of Internal Variability and External Forcing to Atlantic Multidecadal Variability Since 1870, Geophysical Research Letters, 47, e2020GL089504, https://doi.org/10.1029/2020GL089504, 2020.

Quaglia, I. and Visioni, D.: Modeling 2020 regulatory changes in international shipping emissions helps explain anomalous 2023 warming, Earth Syst. Dynam., 15, 1527-1541, 10.5194/esd-15-1527-2024, 2024.

Raghuraman, S. P., Soden, B., Clement, A., Vecchi, G., Menemenlis, S., and Yang, W.: The 2023 global warming spike was driven by the El Niño–Southern Oscillation, Atmos. Chem. Phys., 24, 11275-11283, 10.5194/acp-24-11275-2024, 2024.

Randel, W. J., Wang, X., Starr, J., Garcia, R. R., and Kinnison, D.: Long-Term Temperature Impacts of the Hunga Volcanic Eruption in the Stratosphere and Above, Geophysical Research Letters, 51, e2024GL111500, https://doi.org/10.1029/2024GL111500, 2024.

Riahi, K., van Vuuren, D. P., Kriegler, E., Edmonds, J., O'Neill, B. C., Fujimori, S., Bauer, N., Calvin, K., Dellink, R., Fricko, O., Lutz, W., Popp, A., Cuaresma, J. C., Kc, S., Leimbach, M., Jiang, L., Kram, T., Rao, S., Emmerling, J., Ebi, K., Hasegawa, T., Havlik, P., Humpenöder, F., Da Silva, L. A., Smith, S., Stehfest, E., Bosetti, V., Eom, J., Gernaat, D., Masui, T., Rogelj, J., Strefler, J., Drouet, L., Krey, V., Luderer, G., Harmsen, M., Takahashi, K., Baumstark, L., Doelman, J. C., Kainuma, M., Klimont, Z., Marangoni, G., Lotze-Campen, H., Obersteiner, M., Tabeau, A., and Tavoni, M.: The Shared Socioeconomic Pathways and their energy, land use, and greenhouse gas emissions implications: An overview, Global Environmental Change, 42, 10.1016/j.gloenvcha.2016.05.009, 2017.

Ribes, A., Qasmi, S., and Gillett, N. P.: Making climate projections conditional on historical observations, Science Advances, 7, eabc0671, 10.1126/sciadv.abc0671, 2021.

Rogelj, J., Popp, A., Calvin, K. V., Luderer, G., Emmerling, J., Gernaat, D., Fujimori, S., Strefler, J., Hasegawa, T., Marangoni, G., Krey, V., Kriegler, E., Riahi, K., Van Vuuren, D. P., Doelman, J., Drouet, L., Edmonds, J., Fricko, O., Harmsen, M., Havlík, P., Humpenöder, F., Stehfest, E., and Tavoni, M.: Scenarios towards limiting global mean temperature increase below 1.5 °c, Nature Climate Change, 8, 10.1038/s41558-018-0091-3, 2018.

Rugenstein, M., Dhame, S., Olonscheck, D., Wills, R. J., Watanabe, M., and Seager, R.: Connecting the SST Pattern Problem and the Hot Model Problem, Geophysical Research Letters, 50, e2023GL105488, https://doi.org/10.1029/2023GL105488, 2023.

Rugenstein, M., Bloch-Johnson, J., Gregory, J., Andrews, T., Mauritsen, T., Li, C., Frölicher, T. L., Paynter, D., Danabasoglu, G., Yang, S., Dufresne, J. L., Cao, L., Schmidt, G. A., Abe-Ouchi, A., Geoffroy, O., and Knutti, R.: Equilibrium Climate Sensitivity Estimated by Equilibrating Climate Models, Geophysical Research Letters, 47, 10.1029/2019GL083898, 2020.

Rugenstein, M., Bloch-Johnson, J., Abe-Ouchi, A., Andrews, T., Beyerle, U., Cao, L., Chadha, T., Danabasoglu, G., Dufresne, J.-L., Duan, L., Foujols, M.-A., Frölicher, T., Geoffroy, O., Gregory, J., Knutti, R., Li, C., Marzocchi, A., Mauritsen, T., Menary, M., Moyer, E.,

Nazarenko, L., Paynter, D., Saint-Martin, D., Schmidt, G. A., Yamamoto, A., and Yang, S.: LongRunMIP: Motivation and Design for a Large Collection of Millennial-Length AOGCM Simulations, Bulletin of the American Meteorological Society, 100, 2551-2570, https://doi.org/10.1175/BAMS-D-19-0068.1, 2019.

Rugenstein, M. A. A. and Armour, K. C.: Three Flavors of Radiative Feedbacks and Their Implications for Estimating Equilibrium Climate Sensitivity, Geophysical Research Letters, 48, e2021GL092983, https://doi.org/10.1029/2021GL092983, 2021.

Saji, N. H. and Yamagata, T.: Possible impacts of Indian Ocean Dipole mode events on global climate, Climate Research, 25, 151-169, 2003.

Salawitch, R. J., Canty, T. P., Hope, A. P., Tribett, W. R., and Bennett, B. F.: Paris Climate Agreement: Beacon of Hope, Springer Climate, 10.1009/978-3-319-469393, 2017.

Samset, B. H., Lund, M. T., Fuglestvedt, J. S., and Wilcox, L. J.: 2023 temperatures reflect steady global warming and internal sea surface temperature variability, Communications Earth & Environment, 5, 460, 10.1038/s43247-024-01637-8, 2024.

Samset, B. H., Zhou, C., Fuglestvedt, J. S., Lund, M. T., Marotzke, J., and Zelinka, M. D.: Steady global surface warming from 1973 to 2022 but increased warming rate after 1990, Communications Earth & Environment, 4, 400, 10.1038/s43247-023-01061-4, 2023.

Samset, B. H., Wilcox, L. J., Allen, R. J., Stjern, C. W., Lund, M. T., Ahmadi, S., Ekman, A., Elling, M. T., Fraser-Leach, L., Griffiths, P., Keeble, J., Koshiro, T., Kushner, P., Lewinschal, A., Makkonen, R., Merikanto, J., Nabat, P., Narazenko, L., O'Donnell, D., Oshima, N., Rumbold, S. T., Takemura, T., Tsigaridis, K., and Westervelt, D. M.: East Asian aerosol cleanup has likely contributed to the recent acceleration in global warming, Communications Earth & Environment, 6, 543, 10.1038/s43247-025-02527-3, 2025.

Schlesinger, M. E. and Ramankutty, N.: An oscillation in the global climate system of period 65-70 years, Nature, 367, 10.1038/367723a0, 1994.

Schmidt, G.: Climate models can't explain 2023's huge heat anomaly — we could be in uncharted territory, https://doi.org/10.1038/d41586-024-00816-z, 2024.

Schoeberl, M. R., Wang, Y., Taha, G., Zawada, D. J., Ueyama, R., and Dessler, A.: Evolution of the Climate Forcing During the Two Years After the Hunga Tonga-Hunga Ha'apai Eruption, Journal of Geophysical Research: Atmospheres, 129, e2024JD041296, https://doi.org/10.1029/2024JD041296, 2024.

Schoeberl, M. R., Wang, Y., Ueyama, R., Dessler, A., Taha, G., and Yu, W.: The Estimated Climate Impact of the Hunga Tonga-Hunga Ha'apai Eruption Plume, Geophysical Research Letters, 50, e2023GL104634, https://doi.org/10.1029/2023GL104634, 2023.

Sherwood, S. C., Bony, S., Boucher, O., Bretherton, C., Forster, P. M., Gregory, J. M., and Stevens, B.: Adjustments in the Forcing-Feedback Framework for Understanding Climate Change, Bulletin of the American Meteorological Society, 96, 217-228, https://doi.org/10.1175/BAMS-D-13-00167.1, 2015.

Skeie, R. B., Berntsen, T., Aldrin, M., Holden, M., and Myhre, G.: Climate sensitivity estimates—sensitivity to radiative forcing time series and observational data, Earth Syst. Dyn., 9, 879-894, 10.5194/esd-9-879-2018, 2018.

Skeie, R. B., Byrom, R., Hodnebrog, Ø., Jouan, C., and Myhre, G.: Multi-model effective radiative forcing of the 2020 sulfur cap for shipping, Atmos. Chem. Phys., 24, 13361-13370, 10.5194/acp-24-13361-2024, 2024a.

Skeie, R. B., Aldrin, M., Berntsen, T. K., Holden, M., Huseby, R. B., Myhre, G., and Storelvmo, T.: The aerosol pathway is crucial for observationally constraining climate sensitivity and anthropogenic forcing, Earth Syst. Dynam., 15, 1435-1458, 10.5194/esd-15-1435-2024, 2024b.

Smith, C., Nicholls, Z. R. J., Armour, K., Collins, W., Forster, P., Meinshausen, M., Palmer, M. D., and Watanabe, M.: The Earth's Energy Budget, Climate Feedbacks, and Climate Sensitivity Supplementary Material. In Climate Change 2021: The Physical Science Basis. Contribution of Working Group I to the Sixth Assessment Report of the Intergovernmental Panel on Climate Change [Masson-Delmotte, V., P. Zhai, A. Pirani, S.L. Connors, C. Péan, S. Berger, N. Caud, Y. Chen, L. Goldfarb, M.I. Gomis, M. Huang, K. Leitzell, E. Lonnoy, J.B.R. Matthews, T.K. Maycock, T. Waterfield, O. Yelekçi, R. Yu, and B. Zhou (eds.)]. Available from https://www.ipcc.ch/, 2021a.

Smith, C., Hall, B., Dentener, F., Ahn, J., Collins, W., Jones, C., Meinshausen, M., Dlugokencky, E., Keeling, R., Krummel, P., Mühle, J., Nicholls, Z., and Simpson, I.: IPCC Working Group 1 (WG1) Sixth Assessment Report (AR6) Annex III Extended Data (v1.0) [Data set]. Zenodo., https://doi.org/10.5281/zenodo.5705391, 2021b.

Smith, C. J., Forster, P. M., Allen, M., Leach, N., Millar, R. J., Passerello, G. A., and Regayre, L. A.: FAIR v1.3: a simple emissions-based impulse response and carbon cycle model, Geosci. Model Dev., 11, 2273-2297, 10.5194/gmd-11-2273-2018, 2018a.

Smith, C. J., Harris, G. R., Palmer, M. D., Bellouin, N., Collins, W., Myhre, G., Schulz, M., Golaz, J. C., Ringer, M., Storelvmo, T., and Forster, P. M.: Energy Budget Constraints on the Time History of Aerosol Forcing and Climate Sensitivity, Journal of Geophysical Research: Atmospheres, 126, 10.1029/2020JD033622, 2021c.

Smith, C. J., Kramer, R. J., Myhre, G., Forster, P. M., Soden, B. J., Andrews, T., Boucher, O., Faluvegi, G., Fläschner, D., Hodnebrog, Ø., Kasoar, M., Kharin, V., Kirkevåg, A., Lamarque, J. F., Mülmenstädt, J., Olivié, D., Richardson, T., Samset, B. H., Shindell, D., Stier, P., Takemura, T., Voulgarakis, A., and Watson-Parris, D.: Understanding Rapid Adjustments to Diverse Forcing Agents, Geophysical Research Letters, 45, 12,023-012,031, https://doi.org/10.1029/2018GL079826, 2018b.

Smith, S. J. and Bond, T. C.: Two hundred fifty years of aerosols and climate: The end of the age of aerosols, Atmospheric Chemistry and Physics, 14, 10.5194/acp-14-537-2014, 2014.

Smith, S. J., Van Aardenne, J., Klimont, Z., Andres, R. J., Volke, A., and Delgado Arias, S.: Anthropogenic sulfur dioxide emissions: 1850-2005, Atmospheric Chemistry and Physics, 11, 10.5194/acp-11-1101-2011, 2011.

Spencer, R. W. and Christy, J. R.: Effective climate sensitivity distributions from a 1D model of global ocean and land temperature trends, 1970–2021, Theoretical and Applied Climatology, 10.1007/s00704-023-04634-7, 2023.

Stevens, B.: Rethinking the Lower Bound on Aerosol Radiative Forcing, Journal of Climate, 28, 4794-4819, https://doi.org/10.1175/JCLI-D-14-00656.1, 2015.

Stevens, B., Sherwood, S. C., Bony, S., and Webb, M. J.: Prospects for narrowing bounds on Earth's equilibrium climate sensitivity, Earth's Future, 4, 512-522, https://doi.org/10.1002/2016EF000376, 2016.

Stjern, C. W., Samset, B. H., Myhre, G., Forster, P. M., Hodnebrog, Ø., Andrews, T., Boucher, O., Faluvegi, G., Iversen, T., Kasoar, M., Kharin, V., Kirkevåg, A., Lamarque, J.-F., Olivié, D., Richardson, T., Shawki, D., Shindell, D., Smith, C. J., Takemura, T., and Voulgarakis, A.: Rapid Adjustments Cause Weak Surface Temperature Response to Increased Black Carbon Concentrations, Journal of Geophysical Research: Atmospheres, 122, 11,462-411,481, https://doi.org/10.1002/2017JD027326, 2017.

Szopa, S., Naik, V., Adhikary, B., Artaxo, P., Berntsen, T., Collins, W. D., Fuzzi, S., Gallardo, L., Kiendler-Scharr, A., Klimont, Z., Liao, H., Unger, N., and Zanis, P.: Short-Lived Climate Forcers, in: Climate Change 2021: The Physical Science Basis. Contribution of Working Group I to the Sixth Assessment Report of the Intergovernmental Panel on Climate Change, edited by: Masson-Delmotte, V., Zhai, P., Pirani, A., Connors, S. L., Péan, C., Berger, S., Caud, N., Chen, Y., Goldfarb, L., Gomis, M. I., Huang, M., Leitzell, K., Lonnoy, E., Matthews, J. B. R., Maycock, T. K., Waterfield, T., Yelekçi, O., Yu, R., and Zhou, B., Cambridge University Press, Cambridge, United Kingdom and New York, NY, USA, 817–922, 10.1017/9781009157896.008, 2021.

Taylor, K. E., Stouffer, R. J., and Meehl, G. A.: An overview of CMIP5 and the experiment design, 10.1175/BAMS-D-11-00094.1, 2012.

Taylor, K. E., Crucifix, M., Braconnot, P., Hewitt, C. D., Doutriaux, C., Broccoli, A. J., Mitchell, J. F. B., and Webb, M. J.: Estimating shortwave radiative forcing and response in climate models, Journal of Climate, 20, 10.1175/JCLI4143.1, 2007.

Tebaldi, C., Debeire, K., Eyring, V., Fischer, E., Fyfe, J., Friedlingstein, P., Knutti, R., Lowe, J., O'Neill, B., Sanderson, B., van Vuuren, D., Riahi, K., Meinshausen, M., Nicholls, Z., Tokarska, K. B., Hurtt, G., Kriegler, E., Lamarque, J. F., Meehl, G., Moss, R., Bauer, S. E., Boucher, O., Brovkin, V., Byun, Y. H., Dix, M., Gualdi, S., Guo, H., John, J. G., Kharin, S., Kim, Y., Koshiro, T., Ma, L., Olivié, D., Panickal, S., Qiao, F., Rong, X., Rosenbloom, N., Schupfner, M., Séférian, R., Sellar, A., Semmler, T., Shi, X., Song, Z., Steger, C., Stouffer, R., Swart, N., Tachiiri, K., Tang, Q., Tatebe, H., Voldoire, A., Volodin, E., Wyser, K., Xin, X., Yang, S., Yu, Y., and Ziehn, T.: Climate model projections from the Scenario Model Intercomparison Project (ScenarioMIP) of CMIP6, Earth Syst. Dynam., 12, 253-293, 10.5194/esd-12-253-2021, 2021.

Thomason, L. W., Ernest, N., Millán, L., Rieger, L., Bourassa, A., Vernier, J. P., Manney, G., Luo, B., Arfeuille, F., and Peter, T.: A global space-based stratospheric aerosol climatology: 1979-2016, Earth System Science Data, 10, 10.5194/essd-10-469-2018, 2018.

Ting, M., Kushnir, Y., Seager, R., and Li, C.: Forced and Internal Twentieth-Century SST Trends in the North Atlantic, Journal of Climate, 22, 1469-1481, https://doi.org/10.1175/2008JCLI2561.1, 2009.

Tokarska, K. B., Hegerl, G. C., Schurer, A. P., Forster, P. M., and Marvel, K.: Observational constraints on the effective climate sensitivity from the historical period, Environmental Research Letters, 15, 10.1088/1748-9326/ab738f, 2020a.

Tokarska, K. B., Stolpe, M. B., Sippel, S., Fischer, E. M., Smith, C. J., Lehner, F., and Knutti, R.: Past warming trend constrains future warming in CMIP6 models, Science Advances, 6, 10.1126/sciadv.aaz9549, 2020b.

Tollefson, J.: Earth shattered heat records in 2023 and 2024: is global warming speeding up?, 2025.

Trenberth, K. E. and Shea, D. J.: Atlantic hurricanes and natural variability in 2005, Geophysical Research Letters, 33, https://doi.org/10.1029/2006GL026894, 2006.

Tsutsui, J. and Smith, C.: Revisiting two-layer energy balance models for climate assessment, Environmental Research Letters, 20, 014059, 10.1088/1748-9326/ad9ec5, 2025.

Twomey, S.: Pollution and the planetary albedo, Atmospheric Environment (1967), 8, 1251-1256, https://doi.org/10.1016/0004-6981(74)90004-3, 1974.

van Vuuren, D., O'Neill, B., Tebaldi, C., Chini, L., Friedlingstein, P., Hasegawa, T., Riahi, K., Sanderson, B., Govindasamy, B., Bauer, N., Eyring, V., Fall, C., Frieler, K., Gidden, M., Gohar, L., Jones, A., King, A., Knutti, R., Kriegler, E., Lawrence, P., Lennard, C., Lowe, J., Mathison, C., Mehmood, S., Prado, L., Zhang, Q., Rose, S., Ruane, A., Schleussner, C. F., Seferian, R., Sillmann, J., Smith, C., Sörensson, A., Panickal, S., Tachiiri, K., Vaughan, N., Vishwanathan, S., Yokohata, T., and Ziehn, T.: The Scenario Model Intercomparison Project for CMIP7 (ScenarioMIP-CMIP7), EGUsphere, 2025, 1-38, 10.5194/egusphere-2024-3765, 2025.

van Vuuren, D. P., Kriegler, E., O'Neill, B. C., Ebi, K. L., Riahi, K., Carter, T. R., Edmonds, J., Hallegatte, S., Kram, T., Mathur, R., and Winkler, H.: A new scenario framework for Climate Change Research: scenario matrix architecture, Climatic Change, 122, 373-386, 10.1007/s10584-013-0906-1, 2014.

van Vuuren, D. P., Stehfest, E., Gernaat, D. E. H. J., Doelman, J. C., van den Berg, M., Harmsen, M., de Boer, H. S., Bouwman, L. F., Daioglou, V., Edelenbosch, O. Y., Girod, B., Kram, T., Lassaletta, L., Lucas, P. L., van Meijl, H., Müller, C., van Ruijven, B. J., van der Sluis, S., and Tabeau, A.: Energy, land-use and greenhouse gas emissions trajectories under a green growth paradigm, Global Environmental Change, 42, 10.1016/j.gloenvcha.2016.05.008, 2017.

Vaughan, M. A., Young, S. A., Winker, D. M., Powell, K. A., Omar, A. H., Liu, Z., Hu, Y., and Hostetler, C. A.: Fully automated analysis of space-based lidar data: an overview of the CALIPSO retrieval algorithms and data products, Laser Radar Techniques for Atmospheric Sensing, 10.1117/12.572024,

Vial, J., Dufresne, J. L., and Bony, S.: On the interpretation of inter-model spread in CMIP5 climate sensitivity estimates, Climate Dynamics, 41, 10.1007/s00382-013-1725-9, 2013.

Voosen, P.: Use of 'too hot' climate models exaggerates impacts of global warming, Science, 376, 10.1126/science.abq8448, 2022.

Vömel, H., Evan, S., and Tully, M.: Water vapor injection into the stratosphere by Hunga Tonga-Hunga Ha'apai, Science, 377, 1444-1447, 10.1126/science.abq2299, 2022.

Watson-Parris, D., Wilcox, L. J., Stjern, C. W., Allen, R. J., Persad, G., Bollasina, M. A., Ekman, A. M. L., Iles, C. E., Joshi, M., Lund, M. T., McCoy, D., Westervelt, D., Williams, A., and

Samset, B. H.: Weak surface temperature effects of recent reductions in shipping SO2 emissions, with quantification confounded by internal variability, EGUsphere, 2024, 1-30, 10.5194/egusphere-2024-1946, 2024.

Weaver, C., Wu, D. L., Bhartia, P. K., Labow, G., Haffner, D. P., Borgia, L., McBride, L., and Salawitch, R.: Comparison of Proxy-Shortwave Cloud Albedo from SBUV Observations with CMIP6 Models, Journal of Climate, 37, 3093-3116, https://doi.org/10.1175/JCLI-D-23-0170.1, 2024.

Winton, M., Adcroft, A., Dunne, J. P., Held, I. M., Shevliakova, E., Zhao, M., Guo, H., Hurlin, W., Krasting, J., Knutson, T., Paynter, D., Silvers, L. G., and Zhang, R.: Climate Sensitivity of GFDL's CM4.0, Journal of Advances in Modeling Earth Systems, 12, e2019MS001838, https://doi.org/10.1029/2019MS001838, 2020.

WMO: State of the Global Climate 2024, 2025.

WMO, W. M. O.: Scientific Assessment of Ozone Depletion: 2018, Global Ozone Research and Monitoring Project – Report No. 58, 588 pp., Geneva, Switzerland, 2018.

Wolter, K. and Timlin, M. S.: Monitoring ENSO in COADS with a seasonally adjusted principal component index, 1993.

Wolter, K. and Timlin, M. S.: El Niño/Southern Oscillation behaviour since 1871 as diagnosed in an extended multivariate ENSO index (MEI.ext), International Journal of Climatology, 31, 10.1002/joc.2336, 2011.

Xie, M., Wang, J.-Z., Zhang, L., and Chen, Z.: Exceptional Equatorial Extension of Extreme Indian Ocean Dipole Cooling: Shaping Effect From Strong El Niño, Geophysical Research Letters, 52, e2024GL112464, https://doi.org/10.1029/2024GL112464, 2025.

Yoshioka, M., Grosvenor, D. P., Booth, B. B. B., Morice, C. P., and Carslaw, K. S.: Warming effects of reduced sulfur emissions from shipping, Atmos. Chem. Phys., 24, 13681-13692, 10.5194/acp-24-13681-2024, 2024.

Yuan, T., Song, H., Oreopoulos, L., Wood, R., Bian, H., Breen, K., Chin, M., Yu, H., Barahona, D., Meyer, K., and Platnick, S.: Abrupt reduction in shipping emission as an inadvertent geoengineering termination shock produces substantial radiative warming, Communications Earth & Environment, 5, 281, 10.1038/s43247-024-01442-3, 2024.

Zelinka, M. D., Andrews, T., Forster, P. M., and Taylor, K. E.: Quantifying components of aerosol-cloud-radiation interactions in climate models, Journal of Geophysical Research: Atmospheres, 119, 10.1002/2014JD021710, 2014.

Zelinka, M. D., Myers, T. A., McCoy, D. T., Po-Chedley, S., Caldwell, P. M., Ceppi, P., Klein, S. A., and Taylor, K. E.: Causes of Higher Climate Sensitivity in CMIP6 Models, Geophysical Research Letters, 47, 10.1029/2019GL085782, 2020.

Zhang, H., Wang, F., Li, J., Duan, Y., Zhu, C., and He, J.: Potential Impact of Tonga Volcano Eruption on Global Mean Surface Air Temperature, Journal of Meteorological Research, 36, 1-5, 10.1007/s13351-022-2013-6, 2022.

Zhang, H.-M., Lawrimore, J., Huang, B., Menne, M., Yin, X., Sánchez-Lugo, A., Gleason, B., Vose, R., Arndt, D., Rennie, J., and Williams, C.: Updated Temperature Data Give a Sharper View of Climate Trends, Eos, 100, 10.1029/2019eo128229, 2019a.

Zhang, R., Sutton, R., Danabasoglu, G., Kwon, Y.-O., Marsh, R., Yeager, S. G., Amrhein, D. E., and Little, C. M.: A Review of the Role of the Atlantic Meridional Overturning Circulation in Atlantic Multidecadal Variability and Associated Climate Impacts, Reviews of Geophysics, 57, 316-375, https://doi.org/10.1029/2019RG000644, 2019b.

Zhou, J. and Tung, K. K.: Deducing multidecadal anthropogenic global warming trends using multiple regression analysis, Journal of the Atmospheric Sciences, 70, 10.1175/JAS-D-12-0208.1, 2013.

Zhu, Y., Bardeen, C. G., Tilmes, S., Mills, M. J., Wang, X., Harvey, V. L., Taha, G., Kinnison, D., Portmann, R. W., Yu, P., Rosenlof, K. H., Avery, M., Kloss, C., Li, C., Glanville, A. S., Millán, L., Deshler, T., Krotkov, N., and Toon, O. B.: Perturbations in stratospheric aerosol evolution due to the water-rich plume of the 2022 Hunga-Tonga eruption, Communications Earth & Environment, 3, 248, 10.1038/s43247-022-00580-w, 2022.